National Technical University of Athens
School of Mechanical Engineering
Fluids Department
Parallel CFD & Optimization Unit

Prediction of the Exterior Wind Noise from Cars & Shape Optimization based on Continuous Adjoint

Diploma Thesis
by

Konstantinos Sarras

Supervisor: Kyriakos C. Giannakoglou
Professor NTUA

Industrial Supervisor: Antoine Delacroix
Manager TME

Athens, 2020

Acknowledgements

First and foremost, I would like to express my deepest gratitude to my professor K.C. Giannakoglou. I would like to thank him for being a great professor, as well as the most inspiring figure throughout all of my studies. I would also like to thank him for believing in me and for assigning me this very interesting project. I consider myself extremely fortunate to have been working under his supervision and I deeply acknowledge that none of this work would have been possible without his help, guidance and support.

Secondly, I would like to deeply thank my industrial supervisor at Toyota Motor Europe (TME), Mr. A. Delacroix. His continuous support and his enthusiasm towards engineering has inspired me and shaped me as an engineer. I would also like to wholeheartedly thank my colleague Panagiotis Koutsantonis, for his constant support and for his very meaningful and valuable guidance throughout this project, as well as the rest of the Vehicle Performance division of TME for their helpful ideas.

I would also like to thank all of the members of the research team of PCOpt/NTUA team and especially Dr. E.M. Papoutsis-Kiachagias, for always having time to discuss with me and whose help has been more than significant in this project.

Last but not least, I would like to thank my family, for always loving and supporting me, as well as my friends and K. for always being there for me, in good and bad.

National Technical University of Athens
School of Mechanical Engineering
Fluids Department
Parallel CFD & Optimization Unit

Prediction of the Exterior Wind Noise from Cars & Shape Optimization based on Continuous Adjoint

Diploma Thesis

Konstantinos Sarras

Supervisor: Kyriakos C. Giannakoglou, Professor NTUA

Athens, 2020

Abstract

The purpose of this diploma thesis is the prediction and minimization of aerodynamically induced noise, or wind noise, in automotive applications. Both of goals of this work are accomplished using CFD-based methods .

In order to computationally predict the wind noise levels of vehicles and to localize the noise sources, a CFD-based Noise Source Identification (NSI) model has been programmed in OpenFOAM©, developed and owned by Toyota Motor Corporation (TMC). The model aims at determining the flow patterns that contribute to the generation of acoustic pressure fluctuations; and consequently sound. The unsteady flow fields of velocity and vorticity acquired from a transient CFD simulation are a prerequisite for the evaluation of the model's equations. To this end, the model's workflow is demonstrated on a Toyota production car for localizing the noise sources around the vehicle's body.

Thereinafter, a shape optimization is applied to the production car for the reduction of noise levels perceived by the driver. The optimization was conducted in the OpenFOAM© environment, using the continuous adjoint method, developed by the Parallel CFD & Optimization Unit (PCOpt/NTUA). The driver's side view mirror (SVM), considered to be the main wind noise contributor, is parametrized and morphed accordingly in order to minimize the aforementioned objective function. A optimal SVM shape for noise reduction has been obtained.

Major part of this thesis was carried out in the premises of Toyota Motor Europe (TME) in Brussels, Belgium, during a 7 month long internship, with Mr. Antoine Delacroix as the industrial advisor.

Εθνικό Μετσόβιο Πολυτεχνείο
Σχολή Μηχανολόγων Μηχανικών
Τομέας Ρευστών
Μονάδα Παράλληλης Υπολογιστικής Ρευστοδυναμικής & Βελτιστοποίησης

Πρόλεξη του Αεροδυναμικά Επαγόμενου Εξωτερικού Θορύβου από Αυτοκίνητα & Βελτιστοποίηση Μορφής με Χρήση της Συνεχούς Συζυγούς Μεθόδου

Διπλωματική εργασία

Κωνσταντίνος Σάρρας

Επιβλέπων: Κυριάκος Χ. Γιαννάκογλου, Καθηγητής ΕΜΠ

Αθήνα, 2020

Σκοπός της διπλωματικής εργασίας είναι η πρόλεξη και ελαχιστοποίηση του αεροδυναμικά επαγόμενου θορύβου, σχετιζόμενου με εφαρμογές της αυτοκινητοβιομηχανίας. Και οι δύο αυτοί στόχοι υλοποιούνται χρησιμοποιώντας μεθόδους και μοντέλα Υπολογιστικής Ρευστοδυναμικής (ΥΡΔ).

Προκειμένου να προσδιοριστούν υπολογιστικά τα επίπεδα αεροδυναμικού θορύβου αυτοκινήτων οχημάτων και να εντοπιστούν οι θέσεις των πηγών αεροδυναμικού θορύβου, προγραμματίστηκε σε περιβάλλον OpenFOAM© μοντέλο Υπολογιστικής Αεροακουστικής (ΥΑΑ), το οποίο αναπτύχθηκε και ανήκει στην Toyota Motor Corporation (TMC) . Το μοντέλο στοχεύει στον προσδιορισμό των σημείων της ροής που συμβάλλουν στη δημιουργία ακουστικών διακυμάνσεων πίεσης και, κατά συνέπεια, στη δημιουργία θορύβου. Τα χρονικά μη-μόνιμα πεδία ταχύτητας και στροβιλότητας, όπως προκύπτουν από λογισμικό ΥΡΔ, απαιτούνται από τις εξισώσεις του μοντέλου. Η ροή εργασίας του αεροακουστικού μοντέλου εφαρμόστηκε στην περίπτωση ενός επιβατικού αυτοκινήτου μαζικής παραγωγής της εταιρίας Toyota , για τον εντοπισμό των πηγών αεροδυναμικού θορύβου γύρω από το σώμα του οχήματος.

Στη συνέχεια, εφαρμόστηκε βελτιστοποίηση μορφής στο εν λόγω αυτοκίνητο παραγωγής με σκοπό τη μείωση των επιπέδων θορύβου που αντιλαμβάνεται ο οδηγός του οχήματος. Η βελτιστοποίηση μορφής βασίστηκε σε λογισμικό της συνεχούς συζυγούς μεθόδου και διεξήχθη στο περιβάλλον του OpenFOAM© , με χρήση του συζυγούς κώδικα ροής που έχει αναπτυχθεί από την Μονάδα Παράλληλης Υπολογιστικής Ρευστοδυναμικής & Βελτιστοποίησης (ΜΠΥΡ&Β). Ο πλευρικός καθρέπτης του οχήματος θεωρήθηκε ως κύριος παράγοντας παραγωγής αεροδυναμικού θορύβου, παραμετροποιήθηκε και παραμορφώθηκε με σκοπό την ελαχιστοποίηση της συνάρτησης κόστους του

προβλήματος βελτιστοποίησης.

Το μεγαλύτερο μέρος της διπλωματικής εργασίας πραγματοποιήθηκε στις εγκαταστάσεις της Toyota Motor Europe (TME) στις Βρυξέλλες, κατά τη διάρκεια μίας επτάμηνης πρακτικής άσκησης, με τον κ. Antoine Delacroix ως επιβλέποντα από την πλευρά της βιομηχανίας.

Acronyms

CAA	Computational Aeroacoustics
CFD	Computational Fluid Dynamics
CPU	Central Processing Unit
EFS	Equivalent Flow Simulation
FAE	Field Adjoint Equations
GBM	Gradient-Based Method
NTUA	National Technical University of Athens
PCOpt	Parallel CFD & Optimization unit
PDE	Partial Differential Equation
RHS	Right Hand Side
TME	Toyota Motor Europe
TMC	Toyota Motor Corporation
w.r.t.	with respect to

ΕΘΣ	Εργαστήριο Θερμικών Στροβιλομηχανών
ΕΜΠ	Εθνικό Μετσόβιο Πολυτεχνείο
ΜΠΥΡ&Β	Μονάδα Παράλληλης Υπολογιστικής Ρευστοδυναμικής & Βελτιστοποίησης
ΥΑΑ	Υπολογιστική Αεροακουστική
ΥΡΔ	Υπολογιστική Ρευστοδυναμική

Contents

Chapter 1

Introduction

Automotive aeroacoustics play a significant role in modern vehicle performance, as they have a strong influence on customer perception, safety and comfort. High levels of interior cabin noise can negatively impact the perception of the driver and, most importantly, lead to fatigue and reduced concentration. While, at low cruising speeds, engine and tire-road noise dominate, at high speeds (generally above 100 kph), aerodynamically induced noise begins to contribute significantly more to overall noise.

In the past, cabin noise reduction was usually accomplished by high quality sealing and acoustic glazing. Nevertheless, these solutions lead to increased car weight and production costs. Today, achieving competitive wind noise performance also depends on detecting and minimising aeroacoustic noise sources generated by the vehicle's shape, by either means of experimental or computa tional methods. Since experimental approaches are excessively expensive, car manufacturers are investing considerable time and effort on computational aeroacoustics (CAA), for developing high-fidelity numerical methods that can predict interior and exterior noise levels with adequate accuracy.

Due to the nonlinearity of the governing equations, developing such CAA schemes for predicting the sound production on fluid flows is a difficult challenge. A direct but unbearably expensive approach to CAA is the Direct Numerical Simulation (DNS) approach, where the compressible flow governing equations resolve both the flow field, and the aerodynamically generated acoustic field. In contrast to the DNS approach, engineers preferably use hybrid CAA approaches, where the sound generation and sound propagation are computed in a decoupled manner. In such a regime, the sound generation alone is determined by flow field characteristics, and thus is resolved using standard Computational Fluid Dynamics (CFD) solvers, while acoustic solvers or analogies model the sound propagation. Such a hybrid approach is also followed in this diploma thesis for the wind noise evaluation of conventional car vehicles.

1.1 Basics of Vehicle Aeroacoustics

The perception of sound relies on the response to the stimulus of acoustic pressure to the human ear. Acoustic pressure p' is the local pressure deviation from the ambient pressure due to acoustic wave propagation, and may be defined as

$$p' = p(t) - p^0 \tag{1.1}$$

where the ambient presure p^0 is a temporal average

$$p^0 = \overline{p} = \lim_{T \to \infty} \frac{1}{T} \int_{-T/2}^{T/2} p(t + t')dt' \tag{1.2}$$

which is not perceived auditevely. The p' term is also called fluctuating sound pressure. An acoustic signal's strength can be appropriately measured by its *mean root square* or *rms* value p_{rms} of acoustic pressure, defined as

$$p_{rms} = \sqrt{\overline{(p')^2}} \tag{1.3}$$

Owing to the wide range of hearing sensitivity spanning a number of orders of magnitude, from approximately 2×10^{-5} Pa (approximate threshold of hearing) to up to 2×10^2 Pa (threshold of pain), the logarithmic sound pressure level L_p (SPL) is commonly used [1], defined as

$$L_p = 10log\left(\frac{p_{rms}}{p_{ref}}\right)^2 = 20log\left(\frac{p_{rms}}{p_{ref}}\right) \tag{1.4}$$

where $p_{ref} = 2 \cdot 10^{-5}$ Pa is the international reference pressure, corresponding to the threshold of hearing for a sinusoidal signal at roughly 2 kHz. The sound pressure level L_p is measured in decibels (dB).

Thereinafter, the sound intensity $\boldsymbol{I}$ can be derived in a spatial point $\boldsymbol{x}$ from sound pressure and sound velocty, as

$$\boldsymbol{I}(\boldsymbol{x}) = \overline{p'\boldsymbol{v'}} \tag{1.5}$$

and sound power P is then obtained by an integration of sound intensity over a closed surface S, i.e.

$$P = \oint_S \boldsymbol{I} \cdot \boldsymbol{n} dS \tag{1.6}$$

Distinction between sound and noise is a purely subjective matter, since noise is practically unwanted sound, depending on the listener and the circumstances. Noise generation varies widely upon each industrial application. In the case of motor vehicles, noise emission comprises drive train noise, tire-road noise and aerodynamic noise [2].

Aerodynamically induced noise can, in principle, be expressed by three noise generating mechanisms. Each of these mechanisms, in turn, can be approximated by idealised models. The first mechanism originates from unsteady volumetric flow, such as that emanating from a leak into the cabin of a vehicle, or from the exhaust of a piston engine [1]. This mechanism can be idealised by a monopole sound source, which is essentially a point in space of fluctuating pressure. The second mechanism arises from the interaction of unsteady pressure fluctuations upon a surface. An example of this is Von Kármán vortex shedding in the vicinity of a rigid body. This mechanism can be modeled by a dipole sound source, comprising of two adjacent monopole sources oscillating out of phase. The last noise generating mechanism is caused by unsteady internal stresses in the fluid flow. This mechanism can be modelled by a quadrupole source, i.e. by two adjacent dipole sources out of phase. These three different fundamental noise sources are illustrated in fig. 1.1.

(a) Monopole (b) Dipole (c) Quadrupole

Figure 1.1: *Representation of the fundamental noise sources. [3]*

Each of these sound sources scales differently with flow speed u or Mach number M, leading to the following relationships [1]

$$I_{monopole} \approx \frac{\rho}{c} u^4 = \rho u^3 M \tag{1.7}$$

$$I_{dipole} \approx \frac{\rho}{c^3} u^6 = \rho u^3 M^3 \tag{1.8}$$

$$I_{quadrupole} \approx \frac{\rho}{c^5} u^8 = \rho u^3 M^5 \tag{1.9}$$

where I is the sound intensity, ρ is the air density and c is the speed of sound.

The dependance of sound sources upon the flow's Mach number can be very useful in understanding the wind noise characteristics of a travelling vehicle. At the relatively low cruising speeds that a car travels, where $M < 0.1$, the monopole sound dominates, followed by dipole and quadrupole sound. Thereupon, dipole and quadrupole sources were sometimes neglected from the aeroacoustic study for simplicity. Nevertheless, as the most significant aerodynamic noise mechanisms in vehicles are either monopoles or dipoles, experimental observation tends to find that the intensity of aerodynamic noise increases with flow speed raised to between the fourth and sixth power [1]. Based on the above, in a more general sense, vehicle wind noise can be separated into three principles; broadband wind rush noise, which is a quadrupole noise caused by turbulent flow in the vicinity of the vehicle; tonal noise, which is a monopole caused by sharp edges or holes in the bodywork; resonance noise, which is a dipole noise caused by the fluid forces acting on the structure. Fig. 2.2 shows graphically those three wind noise classifications.

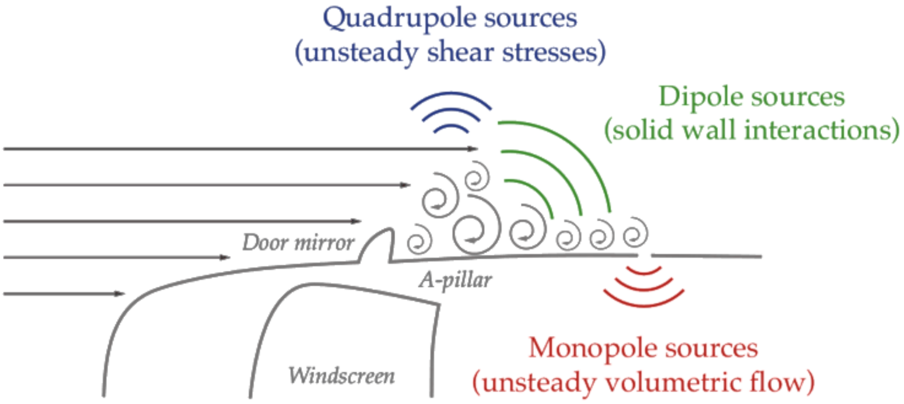

Figure 1.2: *Aeroacoustic noise sources around the area of the side view mirror.[1]*

Considering that gaps on the bodywork are absent and high quality sealing is applied to the windows of modern production cars, the tonal monopole noise becomes less of an issue and dipole sound comes to be the leading problem for car manufacturers.

As already mentioned, dipole sound originates from unsteady pressure fluctuations acting on the solid surfaces of the car. The pressure fluctuations on any surface of the vehicle mainly comprise two parts; convective (or hydrodynamic) pressure fluctuation and acoustic pressure fluctuation [1]. Both of hydrodynamic and acoustic pressure fluctuations induce vibrations on the vehicle's structure (mainly on the side glass) and contribute to the overall cabin noise in their own separate ways.

The energy of convective pressure fluctuation is mainly concentrated at the low frequency range and can excite the side glass to vibrate and hence radiate noise into the interior. Concurrently, the energy of acoustic pressure fluctuation is mainly concentrated an the high frequencies and can be transmitted into the vehicle interior with certain transmission loss through the glass. These two kinds of noise generation and transmission mechanisms are both studied by car manufacturers for reducing cabin noise and improving ride comfort.

---

[1] Main difference between the two is that acoustic fluctuations propagate with the speed of sound, whilst hydrodynamic fluctuations are convected by local velocity

1.2 Motivation & Objectives

The motivation of this diploma thesis stems from the challenge of, on the one hand predicting, and on the other hand minimizing the flow induced noise in automotive applications, i.e. the noise generated due to the aerodynamic shape of the car's geometry. Therefore, the purpose of this diploma thesis is twofold; the primary goal is the wind noise evaluation of conventional car vehicles, i.e. the programming of a hybrid CAA tool in order to predict the wind noise levels and characteristics of car vehicles with adequate accuracy. To this purpose, a vortex sound based model, developed by Toyota Motor Corporation (TMC), has been programmed in OpenFOAM© for the first time within the context of this thesis. The unsteady flow fields of velocity and vorticity acquired from a transient incompressible CFD simulation are a prerequisite for the evaluation of the model's equations. The model returns a key performance indicator (kpi) referred to as *Acoustic Pressure Density Source* (*APDS*), which is expressing the intensity of noise sources in the flow, regarding a frequency range of interest. Hence, it acts as a virtual Noise Source Identification (NSI) tool, identifying and localizing the primary sources of wind noise inside the fluid domain and around the car's geometry. A visualization of the *APDS* index field can help determine the main wind noise generating components on the vehicle's shape.

Secondary objective of this thesis is the reduction of these flow induced noise sources, using a gradient-based shape optimization. After determing the main noise generating component of the vehicle, a shape optimization is performed in order to obtain its optimal shape for noise reduction. Such a reduction could be well achieved by a minimization of the *APDS* levels, regarding a specific frequency range of interest. This could only be accomplished through an unsteady optimization framework. Nevertheless, the application of an unsteady optimization is prohibitively expensive in an industrial enviroment. Owing to this, a surrogate model expressing the generation of wind noise in a steady-state manner is used as the cost functional of the optimization process, based on [4]. The drawback of the latter steady-state approach is that it aims at reducing wind noise in a broadband sense, i.e. it cannot directively reduce noise in specific frequency ranges of high importance. The shape optimization performed is based on the continuous adjoint method and is conducted using the OpenFOAM© adjoint solver, developed by the Parallel CFD & Optimization Unit (PCOpt/NTUA).

Chapter 2

Aerodynamic Analysis

2.1 Flow Modelling

The set of differential equations that describe the motion of any viscous fluid flow are the Navier-Stokes equations, namely the conservation of mass eq. 2.1 and the conservation of momentum eq. 2.1. These are written in tensor notation as

$$\nabla \cdot \boldsymbol{u} = 0 \tag{2.1}$$

$$\frac{\partial \boldsymbol{u}}{\partial t} + (\boldsymbol{u} \cdot \nabla)\boldsymbol{u} = -\nabla p + \nabla \cdot \boldsymbol{\tau} + \mathbf{g} \tag{2.2}$$

where $\boldsymbol{u}$ is the velocity component, p is pressure, $\boldsymbol{\tau}$ is the stress tensor and $\mathbf{g}$ accounts for the external forces acting on the fluid.

The present thesis is concerned with the external turbulent flow that develops around a car geometry. Turbulent flows are chaotic in nature; they are characterised by random fluctuations of pressure and velocity, whilst also being highly irregular and diffusive. Moreover, a turbulent flow exhibits random flow structures that stretch in a wide spectrum of both length and time scales, the so-called eddies. In order to be able properly resolve all of the temporal and spatial scales of a turbulent flow, infinitesimally small discretization in both space and time must by used. Such an approach is called Direct Numerical Simulation (DNS). The cost of a DNS simulation is unbearably large, even for low Reynolds number flows.

On account of this, when simulating turbulent flows, the flow governing equations are usually filtered in both space and time, while the smallest spatial and temporal scales are no longer being resolved, but rather modelled.

2.1.1 Reynolds-Averaged Navier-Stokes Equations

The most widely used approach for simulating turbulent flows is the use of the Reynolds-Averaged Navier-Stokes (RANS) equations. The RANS equations consitute time-averaged equations of motion for fluid flow and can be used with approximations based on knowledge of the properties of flow turbulence to give approximate time-averaged solutions to the Navier–Stokes equations. The idea behind them is *Reynolds Decomposition*, suggested by Osborne Reynolds in 1895, whereby an instantaneous quantity is decomposed into its time-averaged and fluctuating quantities [5, 6]

$$u(\boldsymbol{x},t) = \bar{u}(\boldsymbol{x},t) + u^{'}(\boldsymbol{x},t) \tag{2.3}$$

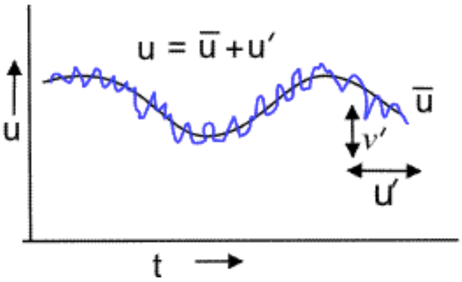

Figure 2.1: *Representation of the Reynolds decomposition in an unsteady flow.*

In the case of unsteady fluid flow, the time filtering applies only to the smallest temporal scales whilst the larger time scale flow structures are resolved, as shown graphically in fig. 2.1. The latter approach is the so-called Unsteady Reynolds Averaged Navier-Stokes (URANS). The system of the URANS equations for an incompressible and statistically steady fluid flow, can be written in Einstein notation and Cartesian coordinates as

$$\frac{\partial \bar{u}_j}{\partial x_j} = 0 \tag{2.4}$$

$$\frac{\partial \bar{u}_i}{\partial t} + \bar{u}_j \frac{\partial \bar{u}_i}{\partial x_j} + \frac{\partial \bar{p}}{\partial x_i} - \frac{\partial}{\partial x_j}\left[\nu\left(\frac{\partial \bar{u}_i}{\partial x_j} + \frac{\partial \bar{u}_j}{\partial x_i}\right)\right] - \frac{\partial}{\partial x_j}\left(-\overline{u_i^{'}u_j^{'}}\right) = 0\ , \qquad i = 1,2,3 \tag{2.5}$$

where 2.4 consitutes the conservation of mass, or continuity, equation and 2.5 constitutes the momentum equation, written in non-conservative form. The ’$^-$’ symbol stands for the mean value of a flow variable, whereas the ’ $'$’ symbol denotes the fluctuating part of a flow variable. The stress term $\tau_{ij}^{'}/\rho = -\overline{u_i^{'}u_j^{'}}$ appearing in 2.5, is the so-called Reynolds stress tensor and is usually modelled according to the Boussinesq hypothesis [6, 7].

2.1.2 Large-Eddy Simulation (LES)

Large-Eddy Simulations [8] are closely related to Direct Numerical Simulation (DNS), in a sense that the most turbulent length scales are being resolved. Specifically, the LES strategy entails that the large energy-containing flow structures of the turbulent wall bounded flow, are solved with adequate spatio-temporal resolution, whereas the smallest dissipative scales of the flow are represented by a subgrid-scale (SGS) model.

For this purpose, any flow field $u(\boldsymbol{x}, t)$ is filtered in space and time onto its resolved and residual part, as

$$u(\boldsymbol{x}, t) = \widetilde{u}(\boldsymbol{x}, t) + u(\boldsymbol{x}, t)^{'} \tag{2.6}$$

where for the resolved part, a filter convolution kernel G is applied [9]

$$\widetilde{u}(\boldsymbol{x}, t) = \int_{-\infty}^{\infty}\int_{-\infty}^{\infty} u(\boldsymbol{x}^{'}, t)G(\boldsymbol{x}^{'} - \boldsymbol{x}, t - \tau)d\tau d\boldsymbol{x}^{'} \tag{2.7}$$

The filter kernel G is associated with a cut-off length Δ, which is generally the mesh size. By applying a filter of size Δ, the Navier-Stokes equations can be written in conservative form as

$$\frac{\partial \widetilde{u_j}}{\partial x_j} = 0 \tag{2.8}$$

$$\frac{\partial \widetilde{u_i}}{\partial t} + \widetilde{u_j}\frac{\partial \widetilde{u_i}}{\partial x_j} = -\frac{1}{\rho}\frac{\partial \widetilde{p}}{\partial x_i} + \nu\frac{\partial^2 \widetilde{u_i}}{\partial x_j \partial x_j} - \frac{\partial \tau_{ij}^{sgs}}{\partial x_j} \tag{2.9}$$

where the stress tensor $\tau_{ij}^{sgs} = \widetilde{u_i u_j} - \widetilde{u_i}\widetilde{u_j}$ of **2.9** is referred to as the subgrid scale stresses term[1] (SGS), accounting for the effect of momentum transport caused by unresolved turbulent motions on the resolved scales. The SGS term is normally modeled by a standard eddy-viscosity Smagorinsky model [8], as

$$\tau_{ij}^{sgs} - \frac{1}{3}\tau_{kk}^{sgs}\delta_{ij} = -2\mathcal{C}_s\Delta^2|\widetilde{\mathcal{S}}|\widetilde{\mathcal{S}}_{ij} \tag{2.10}$$

where δ_{ij} is the Kronecker symbol and $\widetilde{\mathcal{S}_{ij}}$ the strain rate tensor of the resolved velocity field, defined as

$$\widetilde{\mathcal{S}_{ij}} = \frac{1}{2}(\frac{\partial \widetilde{u_i}}{\partial x_j} + \frac{\partial \widetilde{u_j}}{\partial x_i}) \quad \text{and} \quad |\widetilde{\mathcal{S}}| = \sqrt{2\widetilde{\mathcal{S}}_{ij}\widetilde{\mathcal{S}}_{ij}} \tag{2.11}$$

---

[1] Since the filter can be coarser than the employed grid, a more proper term would be subfilter, ranther than subgrid. Nevertheless, the latter labelling is used for historical reasons. [9]

Dimensional analysis shows that the eddy viscosity ν_t can then be determined as

$$\nu_t \propto \lambda \cdot q_{sgs} \tag{2.12}$$

where $\lambda = \mathcal{C}_s \Delta$ is the length scale of the unresolved motions and q_{sgs} their corresponding velocity scale. Assuming isotropic turbulence, the constant yields $\mathcal{C}_s = 0.18$. On the contrary, close to the walls where turbulence is anisotropic and the ν_t value has to be reduced, a damping function is usually used.

2.1.3 Detached Eddy Simulation (DES)

The DES formulation was created to address the challenges faced by LES simulations, when dealing with highly turbulent and massively separated flows, commonly found in aerospace and ground transportation applications. Specifically, the difficulties associated with the use of standard LES models, particularly in near-wall regions, has lead to the development of hybrid models, attempting to combine the best aspects of both RANS and LES formulations in a single solution strategy. Such a hybrid model is the Detached-Eddy Simulation (DES) [10] approach. The model in practice treats the near-wall regions in a RANS-like manner, while the rest of the flow is modeled in an LES-like manner. In light of this, the model is formulated by replacing the distance function term d, in the Spalart-Allmaras model of eq. 4.8, with a modified distance function

$$\widetilde{d} = min(d, \mathcal{C}_{DES}\Delta) \tag{2.13}$$

where $\mathcal{C}_{DES}$ is a constant and $\Delta = max(\Delta x, \Delta y, \Delta z)$ is the largest dimension of the grid cell in question.

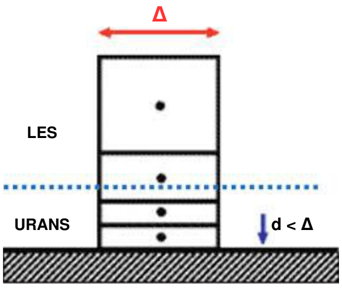

Figure 2.2: *Representation of the switch between URANS and LES close to the walls, based on the mesh resolution [11]*

The introduction of the modified distance $\widetilde{d}$ causes the model to behave as a URANS in the regions close to the walls where $d < \mathcal{C}_{DES}\Delta$, and switch to an LES Smagorinsky model away from the solid boundaries. The latter DES approach implies that a sufficiently fine grid size must be used only in the region close to the walls, contrary to the DNS approach, where fine grid is needed in all directions.

2.1.4 Delayed Detached Eddy Simulation (DDES)

The original DES formulation can exhibit an incorrect behavior in thick boundary layers and shallow separation regions. Specifically, when the stream-wise grid spacing becomes less than the boundary layer thickness, this may result to an early transition to LES mode close to the walls. In principle, this early transition may reduce the calculated skin friction and, in turn, cause and early separation. This numerical phenomenon is termed Grid Induced Separation (GIS).

For this purpose, a sheilding function f_d was defined to ensure that the solution will be a URANS solution, even if the grid spacing is smaller than the boundary layer thickness [12], so as

$$\widetilde{d} = d - f_d \cdot max(0, d - \mathcal{C}_{DES}\Delta) \tag{2.14}$$

with

$$f_d = 1 - tanh[(8r_d)^3] \tag{2.15}$$

where r_d is defined as

$$r_d = \frac{\nu + \nu_t}{k^2 d^2 \sqrt{(\frac{\partial v_i}{\partial x_j})^2}} \tag{2.16}$$

The latter is the origin of the so-called Delayed Detached-Eddy Simulation (DDES). The difference lies in the fact that, on contrary to the natural DES formulation where the length scale depends solely on the grid, in the DDES formulation it depends also on the eddy-viscosity ν_t. [13].

The latter DDES formulation was used in this thesis in order to resolve the turbulent flow that develops around the vehicle's geometry, using the standard PIMPLE solver and the DDES model of OpenFOAM$^{©}$ v.1906.

Chapter 3

Aeroacoustic Analysis

An aeroacoustic analysis aims on the prediction of noise generation owing to turbulent fluid motion or fluid structure interaction. Such an analysis is mostly accomplished by means of computational methods. In principle, hybrid CAA rely on converting unsteady turbulent flow and near field sound data, acquired from a CFD solver, into far field sound information. Analytical models, commonly referred to as *acoustic analogies*, allow this near field unsteady data conversion process to far field sound, some of which are named after Lighthill [**14**], Curle [**15**], Ffowcs-Williams and Hawkings [**16**].

Most of these analytical approaches reach final expressions containing a sound wave propagation operator $\mathcal{L}$, i.e. of the form [**17**]

$$\mathcal{L}(\boldsymbol{u}, \phi^{'}) = S_{\phi'} \tag{3.1}$$

where $\boldsymbol{u}$ denotes the mean velocity field, $\phi^{'}$ the perturbating acoustic variable (usually the fluctuating density $\rho^{'}$ or pressure $p^{'}$) and $S_{\phi'}$ the sources of $\phi^{'}$. Thereby, the source term $S_{\phi'}$ can be provided by an incompressible CFD solution while the wave operator is then responsible for transferring the information to the far field.

Depending on the application, aeroacoustics involve the modelling of either tonal or broadband noise. For tonal noise, (U)RANS (**2.1.1**) can be adequate [**17**]. Nevertheless, as already discussed on the introduction, broadband noise includes source terms depending on turbulent flow structures and unsteady internal fluid stresses. Therefore, determining the characteristics of broadband noise requires the detailed modelling of such unsteady source structures. This need largely invalidates URANS modelling, which can be grossly wrong in such situations, and renders flow models such as DDES (**2.1.4**) more appropriate.

3.1 Acoustic Analogies

Acoustic analogies are commonly used in numerical aeroacoustics to reduce the aeroacoustic sound sources to simple emmiter types. Acoustic analogies were initally introduced by Lighthill in 1952 [14]. In general, such analogies are derived by rearranging the compressible Navier-Stokes equations into various forms of the inhomogeneous wave equation, where the source terms express the acoustic sources. Approximations are later introduced to make the source terms independent of the acoustic variables. In this way, linearized equations are derived which describe the propagation of the acoustic waves in a homogeneous, quiescent medium.

3.1.1 Lighthill's Equation

The basic idea of Lighthill [14, 18] was to reformulate the general equations of fluid dynamics, in order to derive a wave equation. The derivation of the Lighthill equations starts from the momentum equation in conservative form, by neglecting the force term $\boldsymbol{f}$

$$\frac{\partial \rho \boldsymbol{u}}{\partial t} + \nabla \cdot \boldsymbol{\pi} = 0 \tag{3.2}$$

where $\boldsymbol{u}$ is the velocity component and $\pi_{ij} = \rho u_i u_j + (p - p_0)\delta_{ij} - \tau_{ij}$ is the momentum flux tensor. Considering an ideal linear acoustic medium, stress terms may be neglected and the flux tensor can be written as

$$\pi_{ij}^0 = (p - p_0)\delta_{ij} = c_0^2(\rho - \rho_0)\delta_{ij} \tag{3.3}$$

Therefore, the momentum eq. 3.2 reduces to

$$\frac{\partial \rho u_i}{\partial t} + \frac{\partial}{\partial x_i}(c_0^2(\rho - \rho_0)) = 0 \tag{3.4}$$

where, sequentially, the continuity equation allows us to also eliminate the momentum density ρu_i term from 3.4.
Subsequently, by applying a time derivative on 3.4, a spatial derivative on 3.2 and by subtracting the two resulting equations, we obtain

$$\left(\frac{1}{c_0^2}\frac{\partial^2}{\partial t^2} - \nabla \cdot \nabla\right)(c_0^2(\rho - \rho_0)) = 0 \tag{3.5}$$

Therefore, the homogeneous wave equation of $\rho' = \rho - \rho_0$ has been derived, characterised by a propagation speed of c_0 (speed of sound). This equation is referred to as the equation of linear acoustics and is valid at the farfield, away from noise sources.

Thereinafter, Lighthill asserted that the sound generated by turbulence in a "real fluid" is exactly equivalent to that produced in the ideal acoustic medium, forced by a stress distribution of the form

$$L_{ij} = \pi_{ij} - \pi_{ij}^0 = \rho v_i v_j + ((p - p_0) - c_0^2(\rho - \rho_0))\delta_{ij} - \tau_{ij} \tag{3.6}$$

where τ_{ij} accounts for viscous stresses and δ_{ij} is the Kronecker delta. The latter tensor L_{ij} is the so-called *Lighthill's stress tensor.*

Similarly, by rewriting the momentum eq. 3.2 for an ideal, stationary acoustic medium of mean density ρ_0 and speed of sound c_0, subjected to the externally applied stress of L_{ij} yields

$$\left(\frac{1}{c_0^2}\frac{\partial^2}{\partial t^2} - \nabla \cdot \nabla\right)(c_0^2(\rho - \rho_0)) = \frac{\partial^2 L_{ij}}{\partial x_i \partial x_j} \tag{3.7}$$

Eq. 3.7 is known as Lighthill's equation, describing the propagation of ρ' [1] caused by spatial disturbances of the stress tensor L_{ij} in the medium. The problem of calculating the flow generated sound reduces to solving this wave equation, where the source term $\partial^2 L_{ij}/\partial x_i x_j$ is provided e.g. by a CFD simulation. This source term can be interpreted as a quadrupole term, when free field conditions are assumed, i.e. no solid bodies are present [16]. A free field turbulent field exerts very weak sound sources, especially at low Mach numbers. However, in the presence of walls, the sound radiation can dramatically be enhanced, since compact bodies radiate a dipole sound field associated to the force which they exert on the flow.

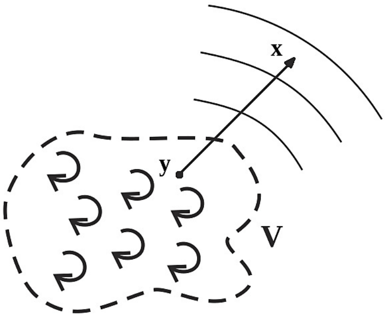

Figure 3.1: *Illustration of the Lighthill's integral equation. The real field is replaced by aquiescent medium with a distribution of volume noise sources, positioned at* $\boldsymbol{y}$*. The density* ρ' *is determined at* $\boldsymbol{x}$ *by an integration of the sources inside volume* V*.*

The solution of eq. 3.7 for a free field radiation condition with outgoing wave

---

[1] A sharp distinction must be made between the fluctuating density ρ' and the acoustic density ρ^{α}, since ρ' is just a superposition of flow and acoustic parts within flow regions.

behaviour can be obtained in intergal form as

$$(\rho - \rho_0)(\boldsymbol{x}, t) = \frac{1}{4\pi c_0^2} \frac{\partial^2}{\partial x_i \partial x_j} \int_V \frac{L_{ij}(\boldsymbol{y}, t - |\boldsymbol{x} - \boldsymbol{y}|/c_0)}{|\boldsymbol{x} - \boldsymbol{y}|} d\boldsymbol{y} \tag{3.8}$$

where $\boldsymbol{y}$ denotes the source coordinate, $\boldsymbol{x}$ the coordinate at which we compute the density fluctuation and V is the volume of the domain of integration. The latter is Lighthill's integral equation, illustrated in fig. 3.1. It should be noted that the tensor L_{ij} is evaluated at retarded time [2] $\tau = t - |\boldsymbol{x} - \boldsymbol{y}|/c_0$.

In conclusion, Lighthill's equation predicts noise radiation from free turbulence, while the whole set of compressible NS have to be solved in order to evaluate Lighthill's tensor. However, this means that we have to resolve both the flow structures and acoustic waves, which implies an enormous challenge for any numerical scheme. In order for the Lighthill's equation to be of practical use, further approximations that decouple the flow field from the acoustic field should be made; see [14, 19].

3.1.2 Curle's Equation

The main limitation of Lighthill's theory is that it is valid only on free turbulence induced radiation. Therefore, it cannot be applied to situations where solid bodies are present in the flow. As already mentioned, solid bodies have a significant impact on noise, since any compact body will radiate sound in the form of a dipole field. The Curle analogy is a formal solution of the Lighthill analogy, which takes hard surfaces into consideration.

Hence, the problem that Curle addressed in [15], was to determine the sound generated by turbulence in the vicinity of an arbitrary, fixed surface Γ_s, illustrated in fig. 3.2.

Thereby, the surface Γ_s is defined by the function $f(\boldsymbol{x})$, which has the following property

$$f(\boldsymbol{x}) = \begin{cases} 0 & \text{for } \boldsymbol{x} \text{ on } \Gamma_s \\ < 0 & \text{for } \boldsymbol{x} \text{ within the surface } \Gamma_s \\ > 0 & \text{for } \boldsymbol{x} \text{ in } \Omega \end{cases} \tag{3.9}$$

The derivation of Curle's equation starts with multiplying the momentum equation

---

[2] Retarded time τ referres to the time when the acoustic waves were generated and began to propagate from the source.

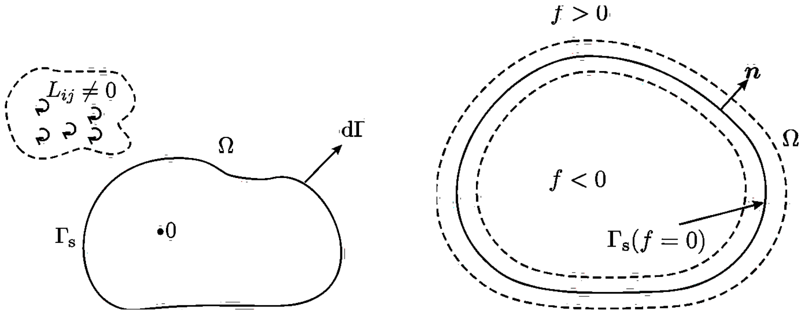

(a) *Turbulent source region next to solid body*

(b) *Solid body*

Figure 3.2: *Illustration of the Curle's equation setup. The solid body is placed inside a quiescent medium with a distribution of volume noise sources, where $L_{ij} \neq 0$. A function $f(\boldsymbol{x})$ is used to model the solid boundaries. Taken from [19].*

3.2 with a Heaviside function $H(f)$, or

$$H(f)\frac{\partial \rho v_i}{\partial t} + H(f)\frac{\partial}{\partial x_i}(c_0^2(\rho - \rho_0)) = -H(f)\frac{\partial L_{ij}}{\partial x_j} \tag{3.10}$$

After mathematical operations and rearrangements described in [15, 16], eq. 3.10 results to the following wave equation

$$\begin{aligned}\left(\frac{1}{c_0^2}\frac{\partial^2}{\partial t^2} - \nabla \cdot \nabla\right)&(c_0^2(\rho - \rho_0)H(f)) \\ &= \frac{\partial^2 L_{ij} H(f)}{\partial x_i \partial x_j} \\ &- \frac{\partial}{\partial xi}\left((\rho v_i v_j + (p - p_0)\delta_{ij} - \tau_{ij})\frac{\partial H(f)}{\partial x_j}\right) \\ &+ \frac{\partial}{\partial t}\left(\rho v_j \frac{\partial H(f)}{\partial x_j}\right)\end{aligned} \tag{3.11}$$

The latter inhomogeneous eq. 3.11 is called Curle's wave equation, and is valid throughout all space, including the region enclosed by Γ_s. In contrast to Lighthill's analogy which accounts only for free turbulence, this equation now takes also the presence of solid bodies in the flow into account. For this reason, eq. 3.11 comprises two additional source terms on the RHS, expressed in terms of spatial derivatives of the Heaviside function $H(f)$. Thereby, according to [19], the second term on the RHS corresponds to a dipole and the third term to a monopole.

Specifically, surface dipole represents the production of sound by the unsteady force that the body exerts on the exterior fluid, whereas the monopole is responsible for the sound generated by volume pulsations (if any) of the body [16].

Solving eq. 3.11 for $\rho'(\boldsymbol{x}, t)$ using Green's function yields

$$\begin{aligned}(\rho - \rho_0)(\boldsymbol{x}, t) = \frac{1}{4\pi c_0^2 H(f)} \cdot \Bigg[& \frac{\partial^2}{\partial x_i \partial x_j} \int_\Omega \frac{\langle L_{ij} \rangle}{|\boldsymbol{x} - \boldsymbol{y}|} d\boldsymbol{y} \\ & - \frac{\partial}{\partial x_i} \oint_{\Gamma_s} \frac{\langle \rho v_i v_j + (p - p_0)\delta_{ij} - \tau_{ij} \rangle}{|\boldsymbol{x} - \boldsymbol{y}|} dS_j(\boldsymbol{y}) \\ & + \frac{\partial}{\partial t} \oint_{\Gamma_s} \frac{\langle \rho v_j \rangle}{|\boldsymbol{x} - \boldsymbol{y}|} dS_j(\boldsymbol{y}) \Bigg]\end{aligned} \tag{3.12}$$

where the $\langle \quad \rangle$ symbol indicates that the terms have to be evaluated at retarded time $\tau = t - |\boldsymbol{x} - \boldsymbol{y}|/c_0$. The latter equation is known as Curle's integral equation.

It should be emphasized that no assumptions have been made nor in Curle's neither in Lighthill's analogy, but only a reformulation of NS equations was made, which was solved using Green's function.

3.1.3 Powell's Vortex Sound Theory

Vortex sound theory is based on the argument that aerodynamic noise is generated as a result of the movement of vortices, or of vorticity, in an unsteady fluid flow, suggested by Alan Powell in 1961 [20]. In consideration of this, the noise production parts of Lighthill's tensor L_{ij} are expressed in terms of local vorticity. The latter approach is very convenient on low Mach number flows, since the vorticity $\boldsymbol{\omega} = \nabla \times \boldsymbol{v}$ is a very convenient quantity to describe them.

Considering a homentropic irrotational flow, Powell's derivation starts from Euler's equations in Crocco's form

$$\frac{1}{\rho}\frac{D\rho}{Dt} = -\nabla \cdot \boldsymbol{v} \tag{3.13}$$

$$\frac{\partial \boldsymbol{v}}{\partial t} + \nabla B = -\boldsymbol{\omega} \times \boldsymbol{v} \tag{3.14}$$

with B being the total enthalpy defined as

$$B = \int \frac{dp}{\rho} + \frac{v^2}{2} = i + \frac{1}{2}v^2 \tag{3.15}$$

and i being the stagnation enthalpy.

By taking the divergence of 3.14 and the time derivative of 3.13 and subtracting the resulting equations, we obtain

$$\frac{\partial}{\partial t}\left(\frac{1}{\rho}\frac{D\rho}{Dt}\right) - \nabla^2 B = \nabla \cdot (\boldsymbol{\omega} \times \boldsymbol{v}) \tag{3.16}$$

Thereupon, we introduce the equations of state

$$dp = c^2 d\rho + \left(\frac{\partial p}{\partial s}\right)_\rho ds, \qquad di = \frac{dp}{\rho} \tag{3.17}$$

Since the entropy is constant ($ds = 0$) accross the flow, by taking into consideration eqs. 3.17, eq. 3.16 becomes

$$\frac{\partial}{\partial t}\left(\frac{1}{c^2}\frac{Di}{Dt}\right) - \nabla^2 B = \nabla \cdot (\boldsymbol{\omega} \times \boldsymbol{v}) \tag{3.18}$$

The independent acoustic variable of Powell's formulation is chosen to be the enthalpy B. For this purpose, a reference potential flow $\boldsymbol{U_0}$ with stagnation enthalpy B_0 is defined, and enthalpy is decomposed around B_0, i.e. $B = B_0 + B'$ [3].

In view of this, expressing eq. 3.18 in terms of B' yields

$$\frac{1}{c^2}\frac{D_0^2 B'}{Dt} - \nabla^2 B' = \nabla \cdot (\boldsymbol{\omega} \times \boldsymbol{v}) + \frac{1}{c^2}\frac{D_0^2 B'}{Dt} - \frac{\partial}{\partial t}\left(\frac{1}{c^2}\frac{Di}{Dt}\right) \tag{3.19}$$

where $D_0/Dt = \partial/\partial t + \boldsymbol{U_0} \cdot \nabla$.

At low Mach number flows, eq. 3.19 reduces to

$$\frac{1}{c_0^2}\frac{D_0^2 B'}{Dt^2} - \nabla^2 B' = \nabla \cdot (\boldsymbol{\omega} \times \boldsymbol{v}) \tag{3.20}$$

The latter inhomogeneous wave equation is referred to as the *Powell's vortex sound equation*. This equation clearly states that homentropic flow can generate sound only if moving vorticity is present. The use of a vortex sound formulation is particularly powerful when a simplified vortex model is available for the flow in question. Examples of such flows are discussed by Howe [21], Disselhorst & van Wijngaarden [22] and Peters & Hirschberg [23]. As far as this thesis is concerned, a model based on vortex sound was used to predict the noise from car geometries, presented next.

---

[3] Note that $i' = p'/\rho_0$ and $B' = i' + \boldsymbol{v_0} \cdot \boldsymbol{v'}$.

3.2 Vortex sound based NSI model

In order to resolve wind noise issues associated with automotive applications, it is important to determine the locations of the primary sources of sound generation around the vehicle. The application of a systematic methodology for noise source identification (NSI) would enable the localization of the sound sources and, in turn, would allow engineers to redesign the vehicle in order to reduce (or minimize) the noise generation. To this purpose, a CFD-based NSI model has been developed and owned by Toyota Motor Corporation (TMC), according to patent No. US 2019/0354647.

Specifically, V.L. Phan [24], in his patent, discloses a formula that makes a link between acoustic pressure fluctuations on the surface of the vehicle with variables of the flow. Thereby, V.L. Phan proposes a method that aims at determining which flow patterns contribute most to the acoustic pressure on a surface of interest. This link is realised through the means of an unsteady CFD solver and with the use of Powell's equation [20], i.e. by an evaluation of enthalpy in space.

Given a cruising vehicle subjected to uniform flow conditions, the setup for the NSI method, as developed by V.L. Phan, starts by defining a fluid volume Ω around the vehicle. This volume is practically where the NSI model's equations will be evaluated and should, therefore, enclose the regions of interest regarding wind noise, i.e. typically the A-pillar, the side view mirror and the side window, as illustrated in fig. 3.3. Secondly, a surface of interest S is defined, where the unsteady pressure fluctuations are computed; this surface is typically chosen to be the side window (side glass).

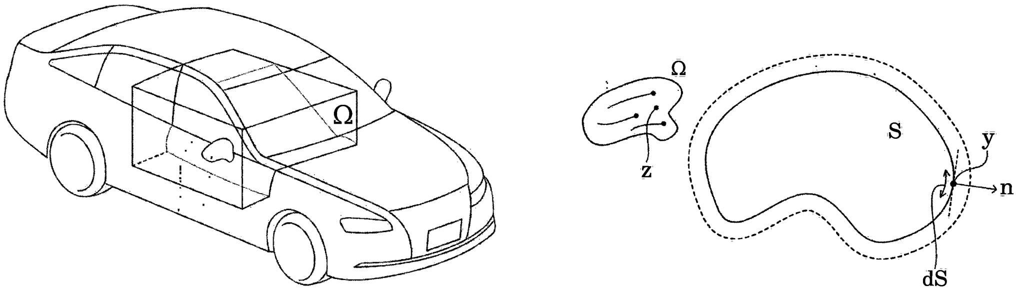

(a) *Volume Ω of evaluation-integration* **(b)** *Fluid volume Ω and surface S*

Figure 3.3: *Fluid volume of evaluation Ω containing the main noise generating components of the vehicle. Points on the fluid volume are denoted as $\boldsymbol{z}$ while surface points on the side glass as $\boldsymbol{y}$*

We let $\boldsymbol{y}$ denote any point of the surface S, $\boldsymbol{z}$ denote any point in the fluid volume Ω and $\boldsymbol{r} = \boldsymbol{y} - \boldsymbol{z}$ their distance vector. The aim is to compute how much does a point $\boldsymbol{z}$ of Ω contribute to unsteady pressure fluctuations on a point $\boldsymbol{y}$ on the side glass. This information can be useful for pinpointing the regions of the fluid volume Ω that are responsible for the unsteady pressure fluctuations on S, and therefore for wind noise. Concurrently, the aim is to determine the noise sources of Ω regarding a specific frequency range of interest. This demand of a frequency domain framework implies the need of a Fourier transform on the unsteady flow variables of interest.

In view of this, the transient flow fields of velocity $\tilde{\boldsymbol{u}}$ are sampled (stored in memory) inside volume Ω with a defined sampling timestep Δt. Thereinafter, the unsteady time series of fluctuating velocty $\tilde{u}(t)$ are transferred to the frequency domain via a Fourier transform, i.e.

$$u_f(f) = \int_{-\infty}^{\infty} \tilde{u}(t) e^{-2\pi i f t} dt \tag{3.21}$$

Evaluating eq. 3.21 for every spatial node $\boldsymbol{z}$ yields the spatial fields of *velocity in frequency domain* $\boldsymbol{u_f}$. In order to numerically obtain the $\boldsymbol{u_f}$ field, a Fast Fourier Transform (FFT) algorithm was implemented in OpenFOAM© v.1906, based on the LIBROW library [25]. The code, in turn, was upgraded to reduce the frequency domain resolution from broadband, to 1^{st} or $1/3^{rd}$ octave bands [4].

By employing Powell's formula of vortex sound (eq. 3.20), V.L. Phan derives a final relational expression for the Acoustic Pressure Density Source ($APDS$), expressed in the frequency domain, of the form

$$APDS(\boldsymbol{y}, \boldsymbol{z}, f_m) = g\left(\frac{{f_m}^2}{|\boldsymbol{r}|^4}, |\boldsymbol{u_f}|, |\overline{\boldsymbol{u}} \times \boldsymbol{r}|, |\overline{\boldsymbol{\varpi}} \times \boldsymbol{r}|\right) \tag{3.22}$$

where $|\boldsymbol{u_f}|$ is the amplitude of velocity in frequency domain, $\overline{\boldsymbol{u}}$ is the time averaged velocity, $\overline{\boldsymbol{\varpi}}$ is the time averaged vorticity, f_m is the frequency band and $\boldsymbol{r} = \boldsymbol{y} - \boldsymbol{z}$ is the distance between the evaluation points.

Eq. 3.22 constitutes an index that shows the degree of contribution of the flow field's point $\boldsymbol{z}$ to the surface acoustic pressure fluctuation of a point $\boldsymbol{y}$, regarding a frequency band of interest f_m. Note that $APDS$ is a function of three variables, where two of which are position vectors of grid nodes. Given the mesh sizes and resolutions commonly used in automotive CFD, storing such a field in RAM memory can be very expensive, or even prohibitive. There lies the need of reducing the frequency domain resolution from broadband to octave frequency bands. Such a reduction decreases drastically the number of frequencies to be stored, thus the memory requirements.

Integrating eq. 3.22 on the vehicle's window surface S, yields the $APDS(\boldsymbol{z}, f_m)$

---

[4] Hereinafter, the index f_m will denote a frequency band around the corresponding central frequency. The band's boundaries are $f_m = \sqrt{2} f_{min} = f_{max}/\sqrt{2}$ for 1^{st} octave bands and $f_{max} = 2^{1/6} f_m$ and $f_{min} = f_m/2^{1/6}$ for $1/3^{rd}$ bands respectively.

field for every spatial node $\boldsymbol{z}$ and every frequency band f_m, i.e.

$$APDS(\boldsymbol{z}, f_m) = \int_S APDS(\boldsymbol{y}, \boldsymbol{z}, f_m) dS \tag{3.23}$$

The volume field of eq. **3.23** may be referred as the *volume acoustic pressure density source field*. High values of the $APDS(\boldsymbol{z}, f_m)$ field pinpoint the regions of the flow field that contribute most to the generation of the acoustic pressure fluctuations of frequency f_m on the side glass.

Equivalently, by integrating eq. **3.22** inside the evaluation volume Ω, we obtain a surface field of $APDS$ for every surface node $\boldsymbol{y}$ and frequency band f_m, i.e.

$$APDS(\boldsymbol{y}, f_m) = \int_\Omega APDS(\boldsymbol{y}, \boldsymbol{z}) d\Omega \tag{3.24}$$

The surface field of eq. **3.24** may be referred to as the *surface acoustic pressure density field*, expressing the acoustic pressure fluctuations distribution on the side glass, owing to the turbulent flow structures of Ω. High values of the $APDS(\boldsymbol{y}, f_m)$ field pinpoint the areas on the side glass that experience high-energy containing pressure fluctuations of frequency f_m.

The described procedure of the NSI method can be arranged in the following workflow of seven consecutive steps :

1. Perform a transient CFD simulation for a total physical time of T seconds, to obtain the unsteady velocity $\tilde{\boldsymbol{u}}$ and vorticity $\tilde{\boldsymbol{\omega}}$ flow fields. Truncate the initial T^* seconds corresponding to the warm-up period of the simulation.
2. Store the unsteady velocity fields of $\tilde{\boldsymbol{u}}$ inside the evaluation volume Ω, with a user-defined sampling timestep Δt. The FFT time window T_f and sampling timestep Δt should aim for the desired frequency domain resolution.
3. Perform a Fast Fourier Transfrom (FFT) on the unsteady velocity flow fields $\tilde{\boldsymbol{u}}$ to obtain the velocity in frequency domain $\boldsymbol{u_f}$ fields. Reduce the frequency domain resolution by an integration to 1^{st} or $1/3^{rd}$ octave bands.
4. Apply a time averaging on velocity and vorticity for an averaging time window of T_w, to obtain the mean velocity $\overline{\boldsymbol{u}}$ and vorticity $\overline{\boldsymbol{\omega}}$ fields.
5. Compute the $APDS(\boldsymbol{y}, \boldsymbol{z}, f_m)$ index by an evaluation of eq. **3.22**.
6. Integrate the $APDS(\boldsymbol{y}, \boldsymbol{z}, f_m)$ field on the vehicle's side window surface S to obtain a $APDS(\boldsymbol{z}, f_m)$ volume field for each frequency band f_m, according to eq. **3.23**.
7. Integrate the $APDS(\boldsymbol{y}, \boldsymbol{z}, f_m)$ field inside the evaluation volume Ω to obtain a $APDS(\boldsymbol{y}, f_m)$ surface field on the side glass for each frequency band f_m, according to eq. **3.24**.

The aforementioned windows of physical time used in the workflow of the NSI model are illustrated in fig. 3.4.

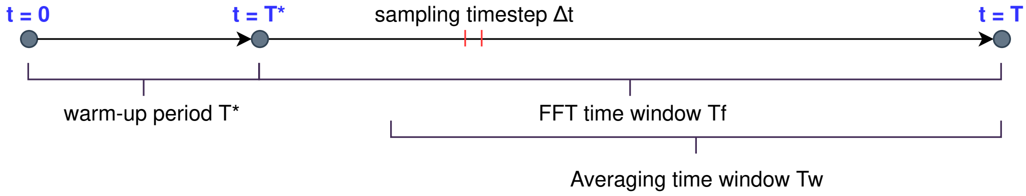

Figure 3.4: *Representation of the time windows used for the computation of APDS. The FFT time window and the averaging time window do not necessarily coincide.*

Given that the time series of fluctuating velocity are ergodic [5], the time window for performing the FFT should typically be chosen so as to include all of the temporal scales of the resolved velocity field; specifically, when cutting off large time scales, while they may not be of interest since they correspond to low frequencies, these attenuated frequency components become aliased to the larger frequencies, resulting to a deformed result.

Concurrently, since the initial conditions of the simulation do not agree with the real states of the system, this leads to a initialization bias in the simulation output, referred to as the *warm-up period.* Given that the time series of the unsteady variables reach at some moment statistical stationarity, the warm-up period of the simulation can be defined with adequate accuracy. In this thesis, the MSER-5 algorithm [26] was employed for detecting the warm-up period.

MSER-5 is an algorithm that acts upon batched (batch size of 5) data $X(j)$ to find the optimal truncation point d^* in the data series where the standard error (test statistic) in the data is at a minimum when the data before that point is deleted [27]

$$d^*(j) = \underset{0\le d(j)\le n}{\arg\min} \left[\frac{1}{(n(j)-d(j))^2} \sum_{i=d+1}^{n} \left(X_i(j) - \overline{X_{n,d}}(j) \right)^2 \right] \tag{3.25}$$

where eq. 3.25 is applied to a series of $b = [n/5]$ batch averages of the data.

The latter NSI model was programmed for the first time in OpenFOAM© v.1906, within the context of this thesis. To this purpose, the original PIMPLE solver of OpenFOAM© was augmented to compute the vorticity field and to sample the unsteady velocity fields inside a predefined evaluation volume, using a user-defined sampling frequency. To this end, both the augmented PIMPLE solver and the NSI model, as well as the FFT utility code, were parallelized in order to use distributed memory through the MPI message passing interface.

---

[5] A process is ergodic if its statistical properties can be deduced from a single, sufficiently long, random sample of the process.

3.3 Application to a Production Car

In this section, the aforementioned vortex sound based NSI model is applied to a production car for localizing the noise sources in the flow. The aim is to determine the flow structures developed around the upper body of the vehicle that contribute to wind noise. As described in 3.2, the first step towards evaluating the *APDS* index is to select a fluid volume around the car. To this purpose, a volume of evaluation Ω is defined, enclosing the components of high importance, i.e. the A-pillar, the side view mirror and the driver's side window. Concurrently, the driver's side windows are considered to be the main mechanism of transmiting sound waves from the exterior to the interior, due to their vibrational response to unsteady pressure excitation. Therefore, the surface S of the model is chosen to be the driver's side window. The particular production car comprises two sets of side windows next to the driver, both of which compose the surface S.

The production car's geometry, as well as the volume of evaluation Ω are illustrated in fig. 3.5. The volume Ω is entirely a fluid volume, hence it excludes any surface point that lies within its boundaries.

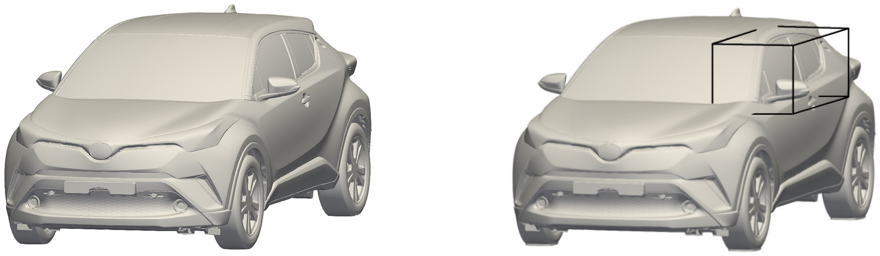

(a) *Vehicle's geometry* **(b)** *Volume of evaluation* Ω

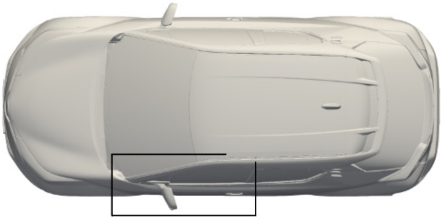

(c) *Top view of volume* Ω

Figure 3.5: *The production car's geometry. A fluid volume* Ω *is defined, enclosing the A-pillar, side view mirror and side window. The volume* Ω *is entirely a fluid volume, therefore it excludes any surface within its boundaries.*

The required unsteady flow data are obtained by using the standard PIMPLE solver of OpenFOAM©, while a DDES (2.1.4) approach is used for resolving the turbulent flow structures, together with the Spalart-Allmaras turbulence model (4.1.2).

CFD Mesh

In order to conduct the unsteady flow simulations around the car geometry, a computational domain is firstly defined. Owing to the apparent symmetry of the problem, a half-car models is used instead of the full-car model. This approach is expected to introduce numerical errors in the vicinity of the symmetry plane, but the benefits in terms of computational cost outweigh, since the size of the domain is practically downsized to half.

The computational domain is a rectangular box around the half-car, comprising an inlet, and outlet, the sides and the top as well as the road (shown in fig. **3.6**). The inlet lies $15m$ upstream from the vehicle, while the outlet lies $25m$ downstream, in order to secure uniform inlet and outlet flow conditions. Similarly, the height and width of the computational domain are approximately $11.6m$ and $11m$ respectively, such as the flow on the top and the sides is practically unaffected by the presence of the vehicle's geometry.

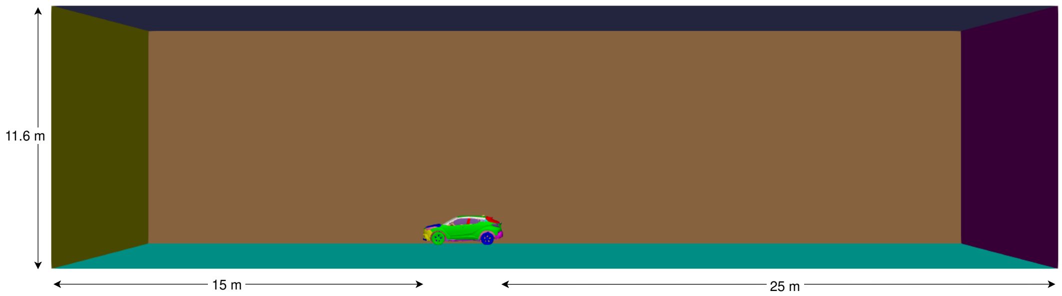

Figure 3.6: *Rectangular computational domain around the vehicle's geometry. The inlet lies* $15m$ *upstream from the vehicle, while the outlet lies* $25m$ *downstream, in order to secure uniform inlet and outlet flow conditions.*

The domain of **3.6** is in turn discretized to form a mesh consisting of cell elements [6]. In order for the DDES model to function properly, the mesh resolution has been kept adequately fine, especially in the areas of high importance. As a result, the employed mesh comprises of $2.8 \cdot 10^6$ surface elements for representing the half-car's surface and $4 \cdot 10^7$ polyhedral volume elements for representing the fluid domain.

Moreover, local refinements near the vehicle's surface and in the areas of relatively high velocity gradients were used, while a coarser mesh was kept at the far field fluid domain. Notably near the wall boundaries, a wall function approach was used in order for the viscous boundary layer to be properly resolved, by featuring layers of prismatic elements, referred hereinafter as *viscous layers*. As described in **2.1.4**, the DDES model is expected to switch to a URANS in the region of the viscous layers.

---

[6] The computational mesh was generated and provided by TME

Furthermore, the surface mesh has been locally refined on the vehicle's upper body components considered of high importance regarding wind noise, i.e. on the side view mirror, the A-pillar and the side windows (shown in fig. 3.7). Clearly, 51444 faces represent the A-pillar, 25383 faces the side view mirror and 16398 faces the side windows.

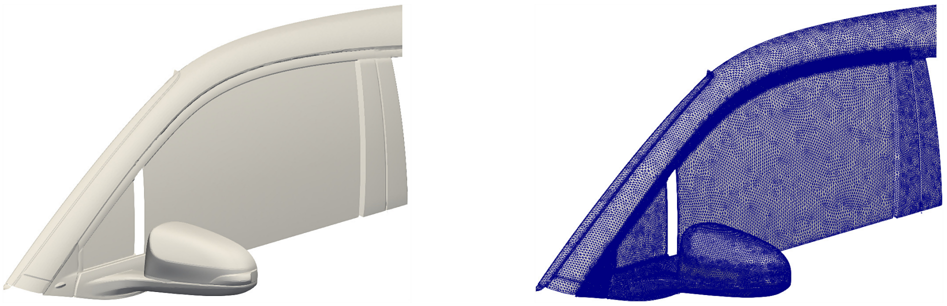

(a) *A-pillar, side view mirror and side window geometries*

(b) *Surface mesh resolutions on the A-pillar, mirror and window*

Figure 3.7: *Surface mesh resolution on the components of interest regarding wind noise, i.e. the A-pillar, the side view mirror and the side window.*

The evaluation volume Ω was defined, consisting of a total of 695137 polyhedral elements. The mesh resolution of Ω is illustrated in fig. 3.8 with the use of a cross-sectional plane. A local refinement near the vehicle's surfaces, were high velocity gradients occur, can be observed. Thereinafter, in order to avoid any singularities in the computation of eq. 3.22, since the $APDS$ index is highly dependent on the cells-to-faces distance $\boldsymbol{r}$ ($APDS \propto 1/|\boldsymbol{r}|^4$), the viscous layers that lie in close proximity to the surface S were excluded from the volume Ω.

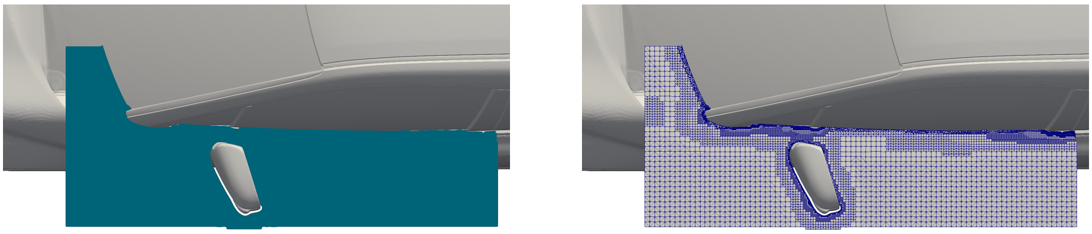

(a) *Parallel to the road cross-sectional plane of evaluation volume* Ω

(b) *Volume mesh resolution on the cross-section plane of volume* Ω

Figure 3.8: *Volume mesh resolution on a cross-section of the evaluation volume* Ω*. The evaluation volume* Ω *consists of a total of* 695137 *hexahedral elements, excluding the prismatic elements of the viscous layers.*

3.3.1 Unsteady Flow Simulation

The unsteady flow fields required by the NSI model are obtained by means of a DDES simulation, using the standard PIMPLE solver of OpenFOAM©. A uniform inflow velocity of $u_\infty = 38.9\ (m/s)$, corresponding to a cruising speed of $140kph$, was imposed on the inlet while a zero Dirichlet condition was imposed on the car's surface, including the wheels which were modeled as stationary.

A workflow of the following 6 steps was followed:

1. Initialize with a well converged steady-state RANS solution, so as to reduce the initialization bias of the unsteady simulation.
2. Run a DDES flow simulation for a total physical time of $T = 0.5s$, with a timestep of $\Delta t = 10^{-5}s$. Sample the unsteady velocity fields inside the volume Ω with a sampling frequency of $\Delta f = 50kHz$ (sampling timestep of $\Delta t = 5 \cdot 10^{-5}s$).
3. Monitor the time series of fluctuating velocity $\widetilde{u}(t)$ in predifined points of the fluid domain, using probes.
4. Perform a MSER-5 analysis, based on eq. 3.25, on the time series of fluctuating velocity $\widetilde{u}(t)$, in order to determine the warm-up period T^* of the simulation.
5. Average the fluctuating velocity $\widetilde{u}$ and vorticity $\widetilde{\omega}$ fields by using an averaging time window of $T_w = 0.2s$ $(0.3s \rightarrow 0.5s)$.
6. Perform a Fast Fourier Transform (FFT) on the unsteady velocity fields of volume Ω, using a FFT time window of $T_f = 0.3s$ $(0.2s \rightarrow 0.5s)$. Reduce the frequency domain resolution to $1/3^{rd}$ octave bands.

The aerodynamic force coefficients were computed during the DDES simulation. The time history of the unsteady lift and drag coefficients, C_L and C_D respectively, normalized around their mean value, are presented in fig. 3.9

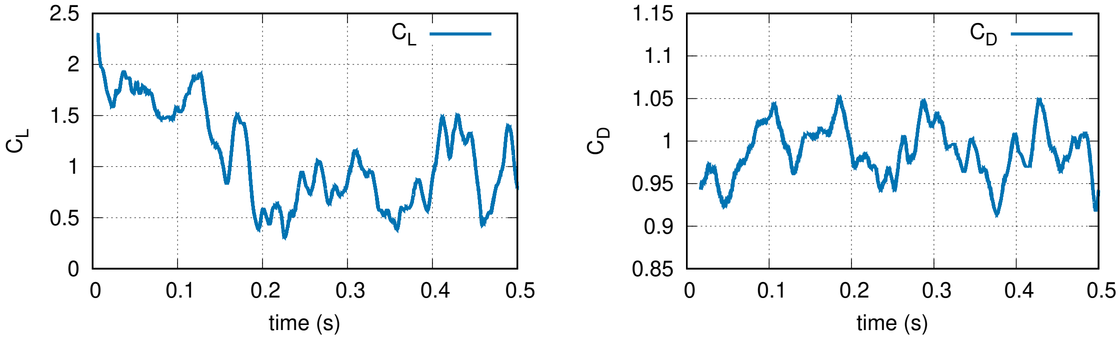

(a) *Time history of lift coefficient C_L* **(b)** *Time history of drag coefficient C_D*

Figure 3.9: *Time history of the unsteady Lift coefficient C_L and Drag coefficient C_D*

During the simulation, several probes have been located inside the volume Ω, to monitor the time series of the unsteady velocity $\widetilde{u}(t)$. Fig. 3.10 illustrates the time series of $\widetilde{u}(t)$ at 4 such locations upstream and downstream of the side view mirror.

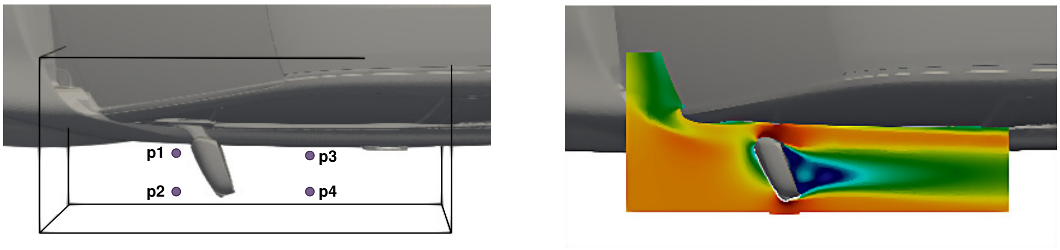

(a) *Probe locations in volume* Ω **(b)** *Instanteneous velocity* $\widetilde{u}$

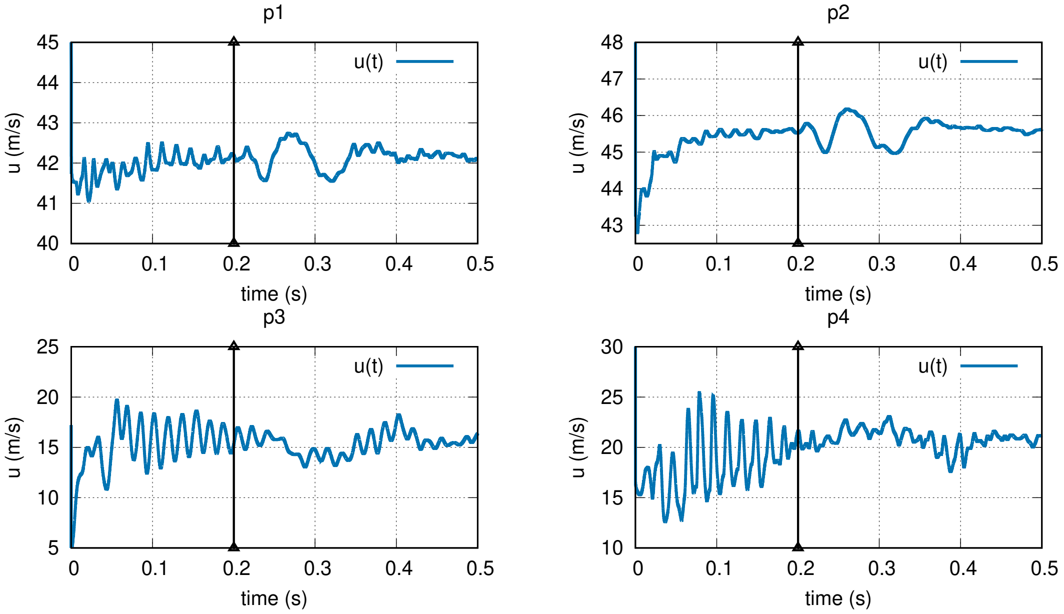

Figure 3.10: *Unsteady velocity magnitude time series* $\widetilde{u}(t)$, *obtained by the DDES solution, plotted for four probe locations p1-p4 on a cutting plane of the evaluation volume* Ω. *The initial* $0.2s$ *were truncated since they correspond to the simulation's warm-up period, determined by the MSER-5 algorithm.*

It is observed that a warm-up period is clearly present in the time series; i.e. the velocity magnitude initially exhibits an upwards trend and takes up time to reach statistical stationarity [7]. The MSER-5 algorithm of eq. 3.25 was applied to 10 velocity time series to properly determine the length of the warm-up period T^*. The T^* value returned from MSER-5 differ from probe to probe, while the largest T^* value was $T^* = 0.2s$, considered to be the warm-up period of the simulation.

---

[7] A process is statistically stationary if its statistical properties do not change when shifted in time. In this specific case, the mean value and standard deviation of velocity magnitude variate in time, until they converge to specific values.

It is noted that the latter approach does not necessarily determine the warm-up period with absolute accuracy; foremost, total simulated physical time of $T = 0.5s$ may not be a sufficiently long sample of the process and may not capture the broader unsteadiness of the physical problem; secondarily, the 10 probe positions were chosen subjectively and may not speak for every fluid point of Ω.

The unsteady velocity flow fields $\tilde{\boldsymbol{u}}$ of volume Ω were transferred to frequency domain via a Fast Fourier Transform (FFT). The frequency domain velocity magnitude fields $|\boldsymbol{u_f}|$ are presented in fig. 3.11, plotted on a cross-section of Ω. Each frequency index f_m denotes a $1/3^{rd}$ octave band around the corresponding frequency.

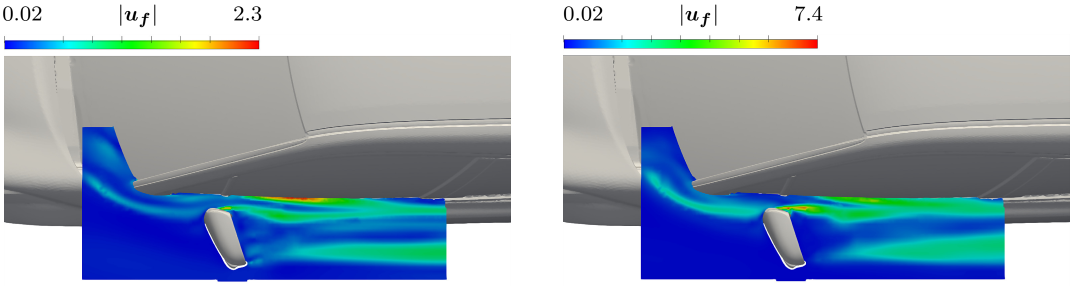

(a) $f_m = 25\ Hz$ **(b)** $f_m = 125\ Hz$

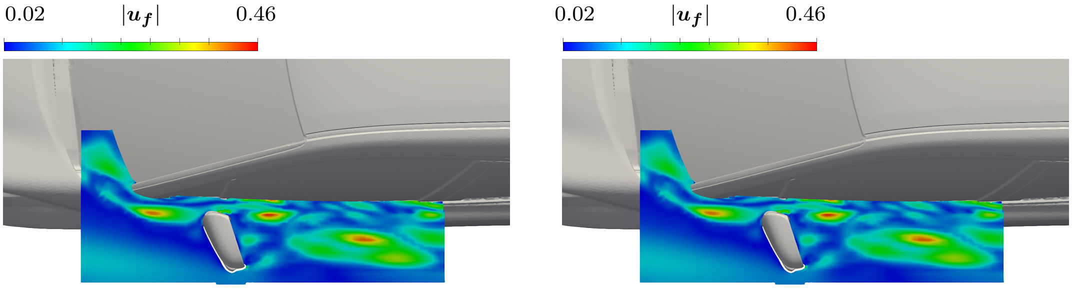

(c) $f_m = 1000\ Hz$ **(d)** $f_m = 2000\ Hz$

Figure 3.11: *Magnitude of velocity in frequency domain* $|\boldsymbol{u_f}|$*, obtained by an FFT on the unsteady velocity* $\tilde{u}$*, plotted on a cross-sectional plane of volume* Ω*. The frequency domain resolution has been reduced to* $1/3^{rd}$ *octave frequency bands.*

In low frequency ranges (e.g. $125\ Hz$), the $|\boldsymbol{u_f}|$ fields exhibit greater magnitudes than on high frequencies (e.g. $2000\ Hz$), showing that the larger eddy structures of the wake downstream of the side view mirror contain more energy than the smallest dissipative scales. Concurrently, at low frequencies, the $|\boldsymbol{u_f}|$ fields display a coherent, streamlined behaviour, while at higher frequencies show less coherent, dispersed structures.

Lastly, the mean velocity $\overline{u}$ and mean vorticity $\overline{\varpi}$ fields were obtained by an time averaging of the corresponding unsteady flow fields, over a time window of $T = 0.3s$, illustrated in fig. 3.12.

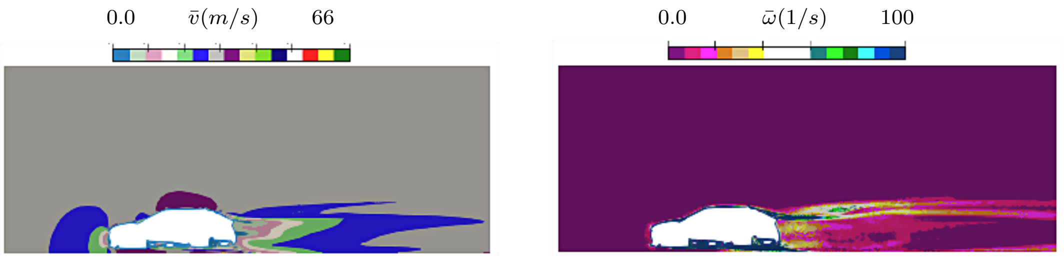

(a) *Averaged velocity magnitude field* $\overline{v}$ **(b)** *Averaged vorticity magnitude field* $\overline{\varpi}$

Figure 3.12: *Mean velocity magnitude* $\overline{u}$ *and vorticity magnitude* $\overline{\varpi}$ *fields, averaged over a time window of* $T = 0.3s$

3.3.2 Computation of the APDS volume field

With the use of the latter flow fields acquired by the DDES solution, eq. 3.22 is evaluated. The resulting $APDS$ index creates a two-way link between the acoustic pressure fluctuations on the side glass and their sources on the fluid volume. An integration of $APDS(y, z, f_m)$ on the vehicle's side glass surface S (eq. 3.23) results to the acoustic pressure density source field $APDS(z)$; one for each frequency band f_m.

Only the frequency band of $f_m = 2kHz$ is deemed of high importance, since the driver's ear is highly sensitive to this frequency range, whereas it does not respond to low frequency noise. Fig. 3.13 illustrates the acoustic pressure density source field for the frequency band of $f_m = 2kHz$.

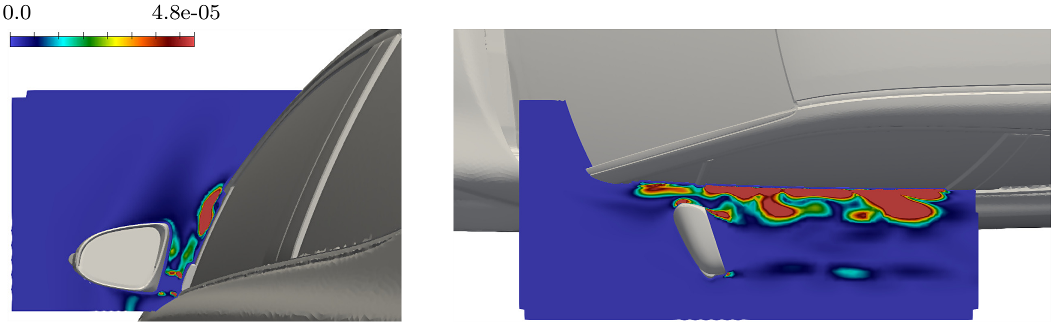

Figure 3.13: *The acoustic pressure density source* $APDS(z)$ *for the frequency band of* $f_m = 2\ kHz$*, plotted on vertical and horizontal cross-sections of the evaluation volume* Ω*. It can be observed that high values of the* $APDS(z)$ *field are tlocated on the wake of the SVM, as well as close to the A-pillar.*

It is observed in fig. 3.13 that high values of the $APDS$ index are located downstream of the side view mirror, as well as near the A-pillar, i.e. close to noise generating components. Meanwhile, since $APDS$ depends on the proximity ($\propto 1\ /|\boldsymbol{r}|^4$), the highest $APDS$ levels are found close to the driver's side window.

For properly determining the spatial patterns of the $APDS$ field, iso-surfaces are used, i.e. surfaces in space representing points of constant $APDS$ value. By visualizing the noise sources distribution field with iso-surfaces (fig. 3.14), we can illustrate the flow patterns of Ω that contribute the most to wind noise.

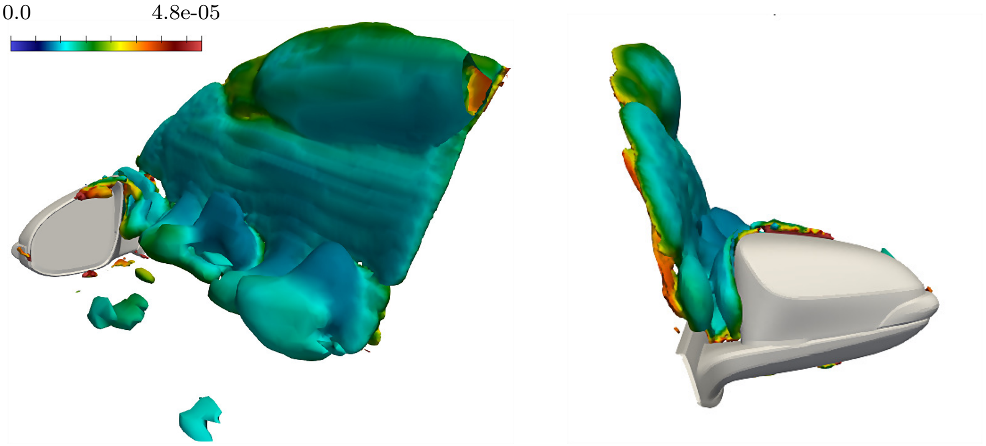

Figure 3.14: *The noise source distribution field* $APDS(z)$ *for the* $f_m = 2\ kHz$ *frequency band, visualized with the use of iso-surfaces inside volume* Ω. *The flow patterns that contribute to pressure fluctuations of* $2\ kHz$ *are the A-pillar's and SVM's wake.*

It is shown in fig. 3.14 that the flow patterns originating from the side view mirror and the A-pillar are mainly responsible for the acoustic pressure fluctuations (of frequency $f_m = 2kHz$) exerted on the side glass. However, the $APDS$ field exhibits clearly more prominant structures downstream of the mirror, than downstream of the A-pillar. Therefore, one can argue that the side view mirror is the dominant noise generating component.

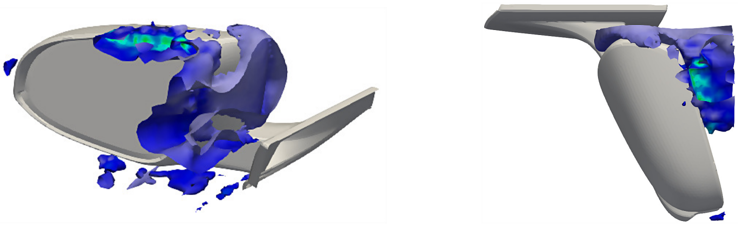

Figure 3.15: *Illustration of the* $APDS(z)$ *field for* $f_m = 2\ kHz$ *around the vehicle's side view mirror (SVM) with the use of iso-surfaces. The inner edge of the mirror appears to contribute the most to the* $2\ kHz$ *pressure fluctuations.*

Considering that the SVM is the main wind noise contributor, we can pinpoint specific areas on its geometry with the greatest potential for noise reduction. Fig. 3.15 suggests that the inner edge of the SVM contributes the most to the generation of acoustic pressure fluctuations, therefore it should be the first geometry feature to be modified.

3.3.3 Computation of the APDS surface field

Lastly, an integration of the $APDS(y,z)$ field inside the evaluation volume Ω results to the surface acoustic pressure density source fields of fig. 3.16 , expressing the acoustic pressure fluctuations distribution on the side glass for each frequency band f_m.

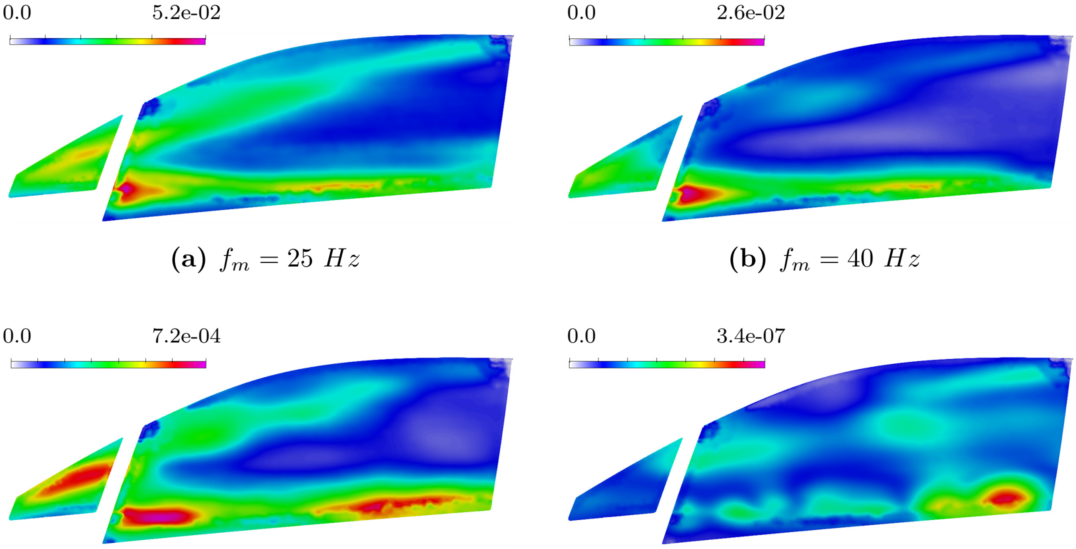

(a) $f_m = 25\ Hz$ **(b)** $f_m = 40\ Hz$

(c) $f_m = 125\ Hz$ **(d)** $f_m = 2000\ Hz$

Figure 3.16: *The surface acoustic pressure density source field $APDS(y)$ over the driver's side windows for specific frequency bands f_m.*

At low frequency bands (e.g. 125 Hz), the pressure fluctuations index field follows a coherent pattern, resembling the vorticity of the mirror's wake, while at higher frequency bands (e.g. 2000 Hz) exhibits significantly smaller magnitudes and a more incoherent behaviour.

Chapter 4

Wind Noise Optimization

In this chapter, an adjoint-based optimization for the reduction of noise in automotive applications is presented and applied, based on [4]. The aim of the optimization worfklow is the reduction of wind noise perceived by the driver's ear, when cruising at high speeds. The big wind noise contributor is considered to be the vehicle's SVM; From a fluid point of view, the side view mirror is a bluff body exposed to a high speed flow. The flow structures in the wake of an SVM are highly transient and subject the vehicle's surfaces (e.g. doors, windows) to significant unsteady pressure fluctuation. This unsteady pressure variations ultimately propagate inside and around the vehicle as sound [28]. For this purpose, a cost functional expressing the creation of noise in terms of turbulence intensity is used. The evaluation of the cost functional is done in a steady-state manner, by means of a RANS equations solver. The cost functional is minimized using an uncostrained gradient-based optimization algorithm, where the framework's control parameters, or design variables, shape the vehicle's SVM. The evaluation of the cost functional's gradient w.r.t. the design variables is performed using the continuous adjoint method, which implies the simulation of an auxiliary set of PDEs, at a cost equivalent to the standard RANS.

4.1 Formulation of the Primal Problem

The primal problem consists of the mathematical formulation and numerical solution of the state equations that govern the physics of the aerodynamic problem under consideration. This optimization problem is concerned with turbulent flows developed around car geometries. The mean flow is resolved through a RANS simulation, while the turbulent flow patterns are being modeled. Moreover, a high-Re mesh has been utilized, together with the use of wall functions.

4.1.1 Governing Equations

Regarding the aerodynamic optimization problem that concerns this thesis, the turbulent flow that develops around the car’s geometry is governed by the steady-state incompressible Navier-Stokes equations. On account of this, the time-averaged RANS (2.1.1) equations are used to model the turbulent flow.

The system of the RANS equations for an incompressible and steady-state fluid flow, can be rewritten in Einstein notation and Cartesian coordinates as

$$R^p = \frac{\partial \bar{v}_j}{\partial x_j} = 0 \tag{4.1}$$

$$R_i^v = \bar{v}_j \frac{\partial \bar{v}_i}{\partial x_j} + \frac{\partial \bar{p}}{\partial x_i} - \frac{\partial}{\partial x_j}\left[\nu\left(\frac{\partial \bar{v}_i}{\partial x_j} + \frac{\partial \bar{v}_j}{\partial x_i}\right)\right] - \frac{\partial}{\partial x_j}\left(-\overline{v_i' v_j'}\right) = 0 \ , \qquad i = 1,2,3 \tag{4.2}$$

where 4.1 consitutes the conservation of mass, or continuity, equation and 4.2 constitutes the momentum equation, written in non-conservative form. The ’$^{-}$’ symbol stands for the mean value of a flow variable, whereas the ’ $'$’ symbol denotes the fluctuating part of a flow variable.

The extra stress term $\tau_{ij}'/\rho = -\overline{v_i' v_j'}$ appearing in 4.2, is the so-called Reynolds stress tensor. According to the Boussinesq hypothesis, proposed by Boussinesq in 1877 [6, 7], this extra stress term may be expressed in terms of mean flow variables as

$$-\overline{v_i' v_j'} = \nu_t \left(\frac{\partial \bar{v}_i}{\partial x_j} + \frac{\partial \bar{v}_j}{\partial x_i}\right) - \frac{2}{3} k \delta_i^j \tag{4.3}$$

where δ_i^j is the Kronecker delta, k is the turbulent kinetic energy (TKE), defined as

$$k = \frac{1}{2}\overline{v_i' v_i'} \tag{4.4}$$

Boussinesq introduces the new viscosity-like variable ν_t, referred to as turbulent,or eddy, viscosity. The turbulent viscosity, in simple terms, is a property of the flow, representing the net effective mixing between fluids.

By taking 4.3 into consideration, the momentum conservation eq. 4.2 yields

$$R_i^v = v_j \frac{\partial v_i}{\partial x_j} - \frac{\partial}{\partial x_j}\left[(\nu + \nu_t)\left(\frac{\partial v_i}{\partial x_j} + \frac{\partial v_j}{\partial x_i}\right)\right] + \frac{\partial p}{\partial x_i} = 0 \ , \qquad i = 1,2,3 \tag{4.5}$$

where the ’$^{-}$’ symbol is omitted for simplicity since all flow variable correspond to the mean flow. This convection will be followed for the rest of this thesis.

4.1.2 The Spalart-Allmaras Model

The Spalart-Allmaras model is a one-equation model that solves a modelled transport equation for the kinematic eddy turbulent viscocity [29]. This model was initially designed specifically for aerospace applications involving wall-bounded flows and has shown good results for boundary layers subjected to adverse pressure gradients. In its original form, it is more effective in low-Reynolds number flows, requiring the viscosity-affected region of the boundary layer to be properly resolved ($y^+ \sim 1$) meshes [1], except when wall functions are used.

The model is proposing a transport equation for a viscosity-like variable $\widetilde{\nu}$, commonly referred to as the Spalart-Allmaras variable. Specifically, the following transport PDE is proposed

$$R^{\widetilde{\nu}} = v_j \frac{\partial \widetilde{\nu}}{\partial x_j} - \frac{\partial}{\partial x_j}\left[\left(\nu + \frac{\widetilde{\nu}}{\sigma}\right)\frac{\partial \widetilde{\nu}}{\partial x_j}\right] - \frac{c_{b2}}{\sigma}\left(\frac{\partial \widetilde{\nu}}{\partial x_j}\right)^2 - \widetilde{\nu}\, P\left(\widetilde{\nu}\right) + \widetilde{\nu}\, D\left(\widetilde{\nu}\right) = 0 \tag{4.6}$$

from which, the eddy viscocity ν_t can then be explicitly expressed as

$$\nu_t = \widetilde{\nu} f_{v_1} \tag{4.7}$$

The production P and destruction D terms of eq. 4.6 are defined as

$$P(\widetilde{\nu}) = c_{b1}\widetilde{Y} \ , \qquad D(\widetilde{\nu}) = c_{w1} f_w(\widetilde{Y})\frac{\widetilde{\nu}}{d^2} \tag{4.8}$$

where $\widetilde{Y}$ is computed through

$$\widetilde{Y} = Y f_{v_3} + \frac{\widetilde{\nu}}{d^2 \kappa^2} f_{v_2} \tag{4.9}$$

while the vorticity magnitude Y is defined as

$$Y = \sqrt{2\boldsymbol{\mathcal{S}} : \boldsymbol{\mathcal{S}}} \ , \qquad \boldsymbol{\mathcal{S}} = \frac{1}{2}\left(\nabla \boldsymbol{u} - (\nabla \boldsymbol{u})^T\right) \tag{4.10}$$

The term $\boldsymbol{\mathcal{S}}$ in eq. 4.10 is the rotation rate tensor, where d denotes the distance of the points in the flow domain from the nearest wall boundary surface. Regarding

---

[1] y^+ stands for the non dimensional distance from the wall, defined as $y^+ = v_\tau y/\nu$, with $v_\tau = \sqrt{\tau_w}$ being the friction velocity, y the absolute distance from the wall and ν the kinematic viscocity. Here, the y^+ value denotes the distance of the first cell centre from the nearest wall, used to determine the mesh resolution near the wall boundaries of the computational domain.

the numerical evaluation of eq. 4.6, since OpenFOAM© uses a cell-centered finite volume discretization scheme, the term d denotes the distance of cell-centres from the closest boundary face-centres [30].

Finally, the functions f_v of the model are defined as

$$
\begin{aligned}
f_{v_1} &= \frac{\chi^3}{\chi^3 + c_{v_1}^3} \;, \quad f_{v_2} = \frac{1}{\left(1 + \frac{\chi}{c_{v_2}}\right)^3} \\
f_{v_3} &= \frac{(1 + \chi f_{v1})}{c_{v2}} \left[3\left(1 + \frac{\chi}{c_{v2}}\right) + \left(\frac{\chi}{c_{v2}}\right)^2 \right] \left(1 + \frac{\chi}{c_{v2}}\right)^{-3} \\
\chi &= \frac{\widetilde{\nu}}{\nu} \;, \quad f_w = g \left(\frac{1 + c_{w_3}^6}{g^6 + c_{w_3}^6} \right)^{1/6} \\
g &= r + c_{w_2}(r^6 - r) \;, \quad r = \frac{\widetilde{\nu}}{\widetilde{Y} \kappa^2 d^2} .
\end{aligned}
\tag{4.11}
$$

The constants of the model can be found in [29], whilst the Levi–Civita symbol e_{ijk} of eq. 4.10 is defined as

$$
e_{ijk} = \begin{cases} +1 & (i,j,k) \in (1,2,3),\ (2,3,1),\ (3,1,2) \\ -1 & (i,j,k) \in (1,3,2),\ (3,2,1),\ (2,1,3) \\ 0 & i = j,\ j = k,\ k = i \end{cases}
\tag{4.12}
$$

4.1.3 Wall Functions

Turbulence models, such as $k - \epsilon$, are only valid for predicting isotropic and fully developed turbulent flows. This is not the case for wall bounded flows, where the fluid close to the wall is greatly influenced by viscosity effects. This layer of fluid, residing on the bounding surface, is called the boundary layer. In order to properly predict the flow properties of the boundary layer, two approaches can be followed.

One approach is to directly integrate turbulence to the wall. Turbulence models, such as the Spalart Allmaras model and $k - \epsilon$, are capable of allowing the viscosity-affected region to be resolved all the way down to the wall, including the viscous sublayer (shown in fig. 4.1). This approach is the so-called *Low-Reynolds number of Turbulence* modelling [6]. Concurrently, the viscous sublayer contains a large amount of information, due to steep velocity profiles and statistically incoherent flow structures. Owing to this, when utilising a Low Reynolds number model, very fine grids must be used, where the first cell-centre must be placed in the viscous sublayer (preferably $y^+ = 1$), so as to be able to properly resolve the flow characteristics. Nonetheless, this requirement leads to the need for substantial computational resources, typically not available in an industrial enviroment.

On the contrary, another way to deal with the near-wall region is the use of the so-called wall functions. Wall functions are empirical equations, used to predict the physics of the flow in the near-wall region. Practically, they are used to bridge the inner region between the wall and the fully developed turbulent one. The latter approach is the so-called *High-Reynolds number of Turbulence* modelling. When using a High Reynolds model, the first cell-centre needs to be placed in the log-law inertial sublayer (shown in fig. 4.1), in order to secure accurate results. Since the viscous sublayer no longer needs to be fully resolved, much coarser grids can be used, rendering wall functions a great choice for industrial applications.

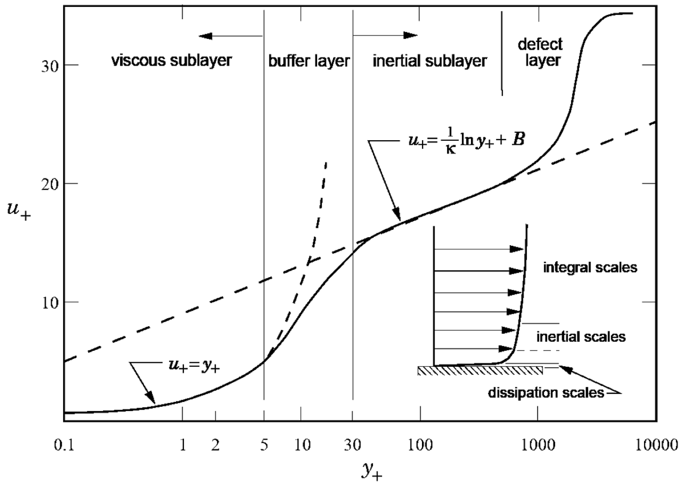

Figure 4.1: *Velocity profiles across the different regions of the boundary layer.*

Regarding this diploma thesis, the wall functions are being employed to estimate the values of ν_t at the closest-to-the-wall cells of the computational domain. Considering this optimization problem, this is very important since the next to the wall ν_t values define the objective function, described in section 4.2.3.

Specifically, as programmed in OpenFOAM©, wall functions are based on a single formula for modelling both the inner sublayer and the logarithmic part of the boundary layer, the so-called Spalding's Law [31]

$$f_{WF} = y_P^+ - v_P^+ - e^{-kB}\left[e^{\kappa v_P^+} - 1 - \kappa v_P^+ - \frac{(\kappa v_P^+)^2}{2} - \frac{(\kappa v_P^+)^3}{6}\right] = 0 \qquad (4.13)$$

where κ is the von Kármán constant equal to 0.41, $B \approx 5.5$ and the non-dimensional distance and velocity at the first cell-center P of the wall are given by [2]

$$y_P^+ = \frac{\Delta^P v_\tau}{\nu}, \qquad v_P^+ = \frac{|v_i|^P}{v_\tau} \tag{4.14}$$

The ν_t values at the first cell-centers off the wall are obtained by computing the viscous flux at the boundary faces f

$$\tau_{ij}|^f n_j = (\nu + \nu_t^f)\frac{v_i^P}{|P_f|} \tag{4.15}$$

Solving the flow equations using wall functions practically means that eq. **4.13** is solved for v_τ at each face f using the Newton-Raphson method and, in turn, ν_t^f is obtained by adjusting **4.15** accordingly [4].

4.1.4 Primal Equations

Based on the aforementioned analysis, the set of differential equations that describe the physics of the steady-state external aerodynamic problem under consideration read

$$R^p = -\frac{\partial v_j}{\partial x_j} = 0 \tag{4.16a}$$

$$R_i^v = v_j \frac{\partial v_i}{\partial x_j} - \frac{\partial}{\partial x_j}\left[(\nu + \nu_t)\left(\frac{\partial v_i}{\partial x_j} + \frac{\partial v_j}{\partial x_i}\right)\right] + \frac{\partial p}{\partial x_i} = 0 \ , \qquad i = 1,2,3 \tag{4.16b}$$

$$R^{\widetilde{\nu}} = v_j \frac{\partial \widetilde{\nu}}{\partial x_j} - \frac{\partial}{\partial x_j}\left[\left(\nu + \frac{\widetilde{\nu}}{\sigma}\right)\frac{\partial \widetilde{\nu}}{\partial x_j}\right] - \frac{c_{b2}}{\sigma}\left(\frac{\partial \widetilde{\nu}}{\partial x_j}\right)^2 - \widetilde{\nu}\, P\left(\widetilde{\nu}\right) + \widetilde{\nu}\, D\left(\widetilde{\nu}\right) = 0 \tag{4.16c}$$

The above-mentioned mean flow equations along with the turbulence model equation **4.16** and their boundary conditions are referred to as the primal (or state) equations of the optimization problem. The vector of primal variables, $\mathbf{U}$, contains the flow variables v_i , p and the turbulence model variable $\widetilde{\nu}$.

The boundary conditions used for the closure of the primal problem are (a) Dirichlet conditions for the velocity vector $\boldsymbol{v}$ and the turbulence model variable $\widetilde{\nu}$, along with a zero Neumann condition for p at the inlet and wall boundaries of the computational domain and (b) a, usually zero, Dirichlet condition for p along with zero Neumann conditions for $\boldsymbol{v}$ and the turbulence model variable at the outlet boundaries [19].

---

[2] where the fricition velocity v_τ is computed over the wall faces f as $v_\tau^2 = -\tau_{ij}|^f n_j t_i^I$, where n_j and t_i^I refer to the components of the unit vectors which are where normal to the wall and parallel to the velocity, at the first cell P [4]

4.2 Formulation of the Adjoint Problem

As already mentioned, an optimization problem aims at the minimization of a cost functional F, given a design space defined by a vector of design variables $\mathbf{b}$. In such an optimization regime, the adjoint problem consists of the derivation of the field adjoint differential equations which can in turn lead to the evaluation of $\delta F/\delta\mathbf{b}$, i.e. the gradient of the cost functional F w.r.t. the design variables $\mathbf{b}$.
In general, F may depend on the state variables $\mathbf{U}$ or on $\mathbf{b} = (b_1, b_2, ..., b_n)$. The cost function F may directly depend on $\mathbf{b}$; for example, in shape optimization problems, F usually includes the normal unit vector to the surface on which F is defined, which depends directly on $\mathbf{b}$. Concurrently, F also depends on $\mathbf{U}$ which, in turn, depends on $\mathbf{b}$ itself; meaning that by varying the design vector $\mathbf{b}$, $\mathbf{U}$ varies also in order to satisfy the primal equations. Therefore, $F = F(\mathbf{b}, \mathbf{U}(\mathbf{b}))$ holds.
Gradient based methods (GBMs) make use of the derivative of F w.r.t. the design variables, or $\delta F/\delta b_n$, in order to minimize F. Typical GBMs algorithms are steepest descent, conjugate gradient [32], quasi-Newton methods like BFGS [33] and SR1 [34] and Newton's method [35]. The key factor for determining the computational cost of the optimization algorithm is the way $\delta F/\delta b_n$ is computed. For example, in a direct differentiation (DD) approach, the derivatives of the state variables $\mathbf{U}$ w.r.t. the design variables b_n are computed at first and, through them, the $\delta F/\delta b_n$ values are derived. As a result, a DD evaluation costs as many as N equivalent state solutions, i.e. as if the state equations were solved for a total of N times.
In an aerodynamic shape optimization, where the state or flow equations may originate from the Navier-Stokes equations, the solution of N equivalent flow simulations (EFS) increases excessively the computational cost. The great advantage of the adjoint method is that it computes $\delta F/\delta b_n$ at a cost that practically does not depend on N. Owing to this, when designing an adjoint based optimization framework, we can choose an indifferently large design space, whenever needed, e.g. in large industrial optimization problems.
An introduction to the continuous adjoint method follows, based on [19, 36]. The adjoint solver, used in this thesis, has been developed in OpenFOAM© by the PCOpt/NTUA team.

4.2.1 Introduction to the Adjoint Variables

The formulation of the continuous adjoint method is based on the definition of the augmented objective function L, defined as

$$L = F + \int_{\Omega} \Psi_i R_i d\Omega \tag{4.17}$$

where F is the objective function or functional, $R_i = 0$ are the residuals of the state equations, Ψ_i are the adjoint variables and Ω the computational domain.

Considering that the residuals of the primal equations are set to zero, $L \equiv F$. The augmented objective function L may also be viewed as the Lagrangian of F and the adjoint variables Ψ_i as Lagrange multipliers.

Differentiation of eq. 4.17 w.r.t. b_n yields

$$\frac{\delta L}{\delta b_n} = \frac{\delta F}{\delta b_n} + \frac{\delta}{\delta b_n} \int_{\Omega} \Psi_i R_i d\Omega \tag{4.18}$$

To further expand the $\delta/\delta b_n$ derivative of the integral term $\int_{\Omega} \Psi_i R_i d\Omega$ in eq. 4.18, two alternative approaches may be followed. Originally, the continuous adjoint equations were derived by further developing this derivative term as follows

$$\frac{\delta}{\delta b_n} \int_{\Omega} \Psi_i R_i d\Omega = \int_{\Omega} \Psi_i \frac{\delta R_i}{\delta b_n} d\Omega + \int_{\Omega} \Psi_i R_i \frac{\delta (d\Omega)}{\delta b_n} \tag{4.19}$$

Considering that $\frac{\delta(d\Omega)}{\delta b_n} = \frac{\partial}{\partial x_k}\left(\frac{\delta x_k}{\delta b_n}\right) d\Omega$, (proof can be found in [19]), eq. 4.18 reads

$$\frac{\delta L}{\delta b_n} = \frac{\delta F}{\delta b_n} + \int_{\Omega} \Psi_i \frac{\delta R_i}{\delta b_n} d\Omega + \int_{\Omega} \Psi_i R_i \frac{\partial}{\partial x_k}\left(\frac{\delta x_k}{\delta b_n}\right) d\Omega \tag{4.20}$$

After expanding eq. 4.20 and by using the following relation between the total and spatial derivatives of any quantity Φ

$$\frac{\delta}{\delta b_n}\left(\frac{\partial \Phi}{\partial x_j}\right) = \frac{\partial}{\partial x_j}\left(\frac{\delta \Phi}{\delta b_n}\right) - \frac{\partial \Phi}{\partial x_k}\frac{\partial}{\partial x_j}\left(\frac{\delta x_k}{\delta b_n}\right) \tag{4.21}$$

(proof also be found in [19]) and the Green-Gauss theorem, the final *FI* sensitivity derivatives expression containing the field variations of x_k is received. The latter is the so-called *FI* adjoint formulation.

To avoid the evaluation of integrals containing the term $\delta x_k/\delta b_n$, the Leibniz theorem for integral variations can be employed as

$$\frac{\delta L}{\delta b_n} = \frac{\delta F}{\delta b_n} + \int_{\Omega} \Psi_i \frac{\partial R_i}{\partial b_n} d\Omega + \underbrace{\int_{S} \Psi_i R_i n_k \frac{\delta x_k}{\delta b_n} dS}_{LBterm} \tag{4.22}$$

in a domain with variable boundaries ($S = S(\mathbf{b}) = \partial\Omega$). Eq. 4.22 is the origin of the so-called *SI* adjoint formulation.

The *LBterm* that appears in this equation denotes the surface integral term introduced by the use of the Leibniz theorem. Originally, the *LBterm* was usually ignored, under the assumption that the state equations R_i are satisfied along the boundaries S. Regarding CFD problems, in fine grids the value of the *LBterm* may become negligible and ignoring it does not harm the computed derivative accuracy. Nevertheless, depending on the case, as well as the mesh coarseness, this term may become very important and can affect the gradient accuracy.

An alternative expression, surrogate to the *LBterm* reads [36]

$$\int_S \Psi_i R_i n_k \frac{\delta x_k}{\delta b_n} dS = -\int_\Omega \frac{\partial}{\partial x_j}\left\{ -u_i v_j \frac{\partial v_i}{\partial x_k} - u_j \frac{\partial p}{\partial x_k} - \tau^a_{ij}\frac{\partial v_i}{\partial x_k} u_i \frac{\partial \tau_{ij}}{\partial x_k} + q\frac{\partial v_j}{\partial x_k}\right\} \frac{\delta x_k}{\delta b_n}\delta\Omega \tag{4.23}$$

where $\tau_{ij} = \nu\left(\frac{\partial v_i}{\partial x_j}\frac{\partial v_j}{\partial x_i}\right)$ is the stress tensor and $\tau^a_{ij} = \nu\left(\frac{\partial u_i}{\partial x_j}\frac{\partial u_j}{\partial x_i}\right)$ is the adjoint stress tensor. Eq. 4.23 will be referred to as *Vterm*.

However, the *Vterm* expression includes a grid displacement term $\delta x_k/\delta b_n$, typically difficult to evaluate. To compute $\delta x_k/\delta b_n$ through finite differences, each design variable has to be displaced by $\pm\epsilon$, where ϵ is an infinitesimally small quantity. The computational cost of the FD approach is that of solving $2N$ grid displacement equations, i.e. equal to the *FI* approach.

To alleviate the need of computing $\delta x_k/\delta b_n$ in the domain Ω, the adjoint formulation is enhanced by solving the adjoint to a hypothetical grid displacement PDE. In view of this, a Laplace equation is utilized as a grid displacement PDE (gdPDE), defined as

$$R^m_i = \frac{\partial^2 m_i}{\partial x_j^2} = 0 \tag{4.24}$$

where m_i are the Cartesian displacements of the grid nodes. Along the boundary, m_i represents the displacement of the boundary points. The displacement component m_i is both a function of x_k, since the gdPDE is satisfied on the given grid and b_n, since the design variables directly affect the boundary conditions of eq. 4.24.

The latter is the origin of the so-called Enchanced *SI* (*E-SI*) adjoint formulation, in which, the gdPDE is considered to be an additional state equation, or, an extra constraint in the optimization.

The continuous adjoint formulation for the aerodynamic shape optimization problem that concerns this thesis, is based in the aforementioned *E-SI* formulation and is presented in the next section.

4.2.2 The E-SI Continuous Adjoint Formulation

The introductory generalised adjoint methodology will be used for the given aerodynamic shape optimization problem, that concerns this thesis. The starting point for the derivation of the adjoint equations is the definition of the Lagrangian or augmented objective function L. In the general E-SI approach used in this thesis, the augmented objective function is defined by expanding F with the volume integral of the state equations, multiplied by the corresponding adjoint variables, as

$$L = F + \int_\Omega u_i R_i^v d\Omega + \int_\Omega q R^p d\Omega + \int_\Omega \widetilde{\nu_a} R^{\widetilde{\nu}} d\Omega + \int_\Omega m_i^a R_i^m d\Omega \tag{4.25}$$

where u_i is the adjoint velocity component, q is the adjoint pressure, $\widetilde{\nu_a}$ is adjoint to $\widetilde{\nu}$ [3] and Ω is the computational domain. The last field integral term in eq. 4.25 corresponds to the laplacian grid displacement PDE. This term would be absent in the FI or SI adjoint formulations. A complete review on the different adjoint formulations can be found in [37].

Differentiating eq. 4.25 w.r.t the design variables b_n and applying Liebniz and Green-Gauss theorem on the volume integrals with variable boundaries ($S = S(\mathbf{b}) = \partial\Omega$) one gets

$$\frac{\delta L}{\delta b_n} = \frac{\delta F}{\delta b_n} + \frac{\delta}{\delta b_n}\int_\Omega \left(u_i R_i^v + q R^p + \widetilde{\nu_a} R^{\widetilde{\nu}} + m_i^a R_i^m\right) d\Omega \tag{4.26}$$

$$\begin{aligned} &= \frac{\delta F}{\delta b_n} + \int_\Omega u_i \frac{\partial R_i^v}{\partial b_n} d\Omega + \int_\Omega q \frac{\partial R^p}{\partial b_n} d\Omega + \int_\Omega \widetilde{\nu_a} \frac{\partial R^{\widetilde{\nu}}}{\partial b_n} d\Omega \\ &+ \int_S m_i^a n_j \frac{\partial}{\partial x_j}\left(\frac{\delta x_i}{\delta b_n}\right) dS - \int_{S_W} \frac{\partial m_i^a}{\partial x_j} n_j \frac{\delta x_i}{\delta b_n} dS + \int_\Omega \frac{\partial^2 m_i^a}{\partial x_j^2} \frac{\delta x_i}{\delta b_n} \delta\Omega \\ &+ \int_S \left(u_i R_i^v + q R^p + \widetilde{\nu_a} R^{\widetilde{\nu}} + m_i^a R_i^m\right) n_k \frac{\delta x_k}{\delta b_n} dS \end{aligned} \tag{4.27}$$

where the boundary S of the computational domain Ω can be expressed in terms of the boundaries S_I, S_O, S_W and S_{W_P} standing for inlet, outlet, fixed and controlled (thus, parameterized) wall boundaries of Ω, respectively, as $S = S_I \cup S_O \cup S_W \cup S_{W_P}$. Furthermore, x_k denotes the coordinates of the boundary's surface points while n_k is the normal to that surface unit vector component.

Since the only boundary that can be deformed is the parameterized boundary S_{W_P} and all the other boundaries are fixed, the term $\delta x_k / \delta b_n$ in eq. 4.26 only applies

---

[3] The adjoint turbulence model equations and variables are neglected in the commonly used "frozen turbulence" assumption.

for that controlled boundary S_{W_P}, which yields

$$\begin{aligned}\frac{\delta L}{\delta b_n} = &\frac{\delta F}{\delta b_n} + \int_{\Omega} u_i \frac{\partial R_i^v}{\partial b_n} d\Omega + \int_{\Omega} q \frac{\partial R^p}{\partial b_n} d\Omega + \int_{\Omega} \widetilde{\nu_a} \frac{\partial R^{\widetilde{\nu}}}{\partial b_n} d\Omega \\ &+ \int_{S_{W_P}} m_i^a n_j \frac{\partial}{\partial x_j} \left(\frac{\delta x_i}{\delta b_n} \right) dS - \int_{S_{W_P}} \frac{\partial m_i^a}{\partial x_j} n_j \frac{\delta x_i}{\delta b_n} dS + \int_{\Omega} \frac{\partial^2 m_i^a}{\partial x_j^2} \frac{\delta x_i}{\delta b_n} \delta\Omega \\ &+ \int_{S_{W_P}} \left(u_i R_i^v + q R^p + \widetilde{\nu_a} R^{\widetilde{\nu}} + m_i^a R_i^m \right) n_k \frac{\delta x_k}{\delta b_n} dS \end{aligned} \tag{4.28}$$

Since the residuals of the state equations must equal to zero over the entire domain Ω, the expression $L = F$ holds and thus $\delta L/\delta b_n = \delta F/\delta b_n$.

Note that a sharp distinction must be made here between the symbols $\delta()/\delta b_n$ and $\partial()/\partial b_n$ in eq. 5.7. Specifically, $\delta\Phi/\delta b_n$ denotes the total (or material) derivative of an arbitrary quantity Φ and speaks for the total change in Φ by varying b_n, whilst $\partial\Phi/\partial b_n$ denotes the partial derivative of Φ and speaks for the variation in Φ due to changes in the flow variables excluding the contributions from the space deformation. From a discrete point of view, the partial derivative represents the variation in Φ if the internal grid nodes of Ω remained unchanged [19].

The total and partial derivatives are linked through the following relationship

$$\frac{\delta \Phi}{\delta b_n} = \frac{\partial \Phi}{\partial b_n} + \frac{\partial \Phi}{\partial x_k} \frac{\delta x_k}{\delta b_n} \tag{4.29}$$

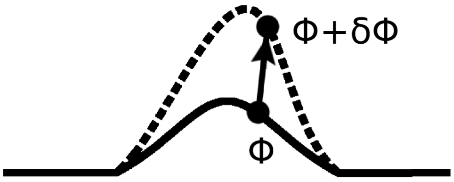

Figure 4.2: *The deformation of the starting geometry of the aerodynamic shape (solid line) to the new one (dashed line) causes the total variation in the quantity* Φ*, given by* $\delta\Phi = \partial\Phi + \partial\Phi\frac{\delta x_k}{\delta b_n}$*. The total variation in* Φ *accounts both for the changes in the flow variables due to the change of the geometry through* $\partial\Phi$ *and on the displacement of the corresponding node through* $\partial\Phi\frac{\delta x_k}{\delta b_n}$ *[19].*

If the total derivative of Φ was to be computed on a surface (e.g. a car's surface), eq. 4.29 whould take a slightly different form. In this case, for any small surface deformation, only the normal part of that deformation velocity $\delta x_k/\delta b_n$ can be taken into account, thus

$$\frac{\delta_s \Phi}{\delta b_n} = \frac{\partial \Phi}{\partial b_n} + \frac{\partial \Phi}{\partial x_k} n_k \frac{\delta x_m}{\delta b_n} n_m \tag{4.30}$$

In eq. 4.30, the symbol $\delta_s()/\delta b_n$ is used to distinguish the surface constrained material derivative from the unconstrained material derivative of eq. 4.29 [19].

In the following mathematical operations to be made, it should be noted that repeated partial derivative operators can be interchangeable, i.e.

$$\frac{\partial}{\partial b_n}\left(\frac{\partial \Phi}{\partial x_j}\right) = \frac{\partial}{\partial x_j}\left(\frac{\partial \Phi}{\partial b_n}\right) \tag{4.31}$$

while the same does not necessarily apply for the total derivatives, i.e.

$$\frac{\delta}{\delta b_n}\left(\frac{\partial \Phi}{\partial x_j}\right) \neq \frac{\partial}{\partial x_j}\left(\frac{\delta \Phi}{\delta b_n}\right) \tag{4.32}$$

4.2.3 Differentiation of the Objective Function

In order to proceed with the formulation of the adjoint differential equations, we must further develop the term of the total derivative of the objective function $\delta F/\delta b_n$, wich appears in eq. 5.7. In the case of a general objective function that comprises both surface and volume integrals, this may be expressed as

$$F = \int_S F_{S_i} n_i dS + \int_\Omega F_\Omega d\Omega \tag{4.33}$$

where F_{S_i} and F_Ω are integrands on the boundary or the volume of the computational domain respectively, while n_i is the normal to the surface unit vector.
By differentiating eq. 4.33 w.r.t. the design variables b_n one gets

$$\frac{\delta F}{\delta b_n} = \frac{\delta}{\delta b_n}\int_S F_{S_i} n_i dS + \frac{\delta}{\delta b_n}\int_\Omega F_\Omega d\Omega \tag{4.34}$$

In what follows, the steps for the derivation of the final expressions of the surface and volume intergals are better presented in detail in [19].

Surface Integral of eq. 4.34

The derivative of the surface integral in eq. 4.34 takes the following final form

$$\begin{aligned}\frac{\delta}{\delta b_n}\int_S F_{S_i} n_i dS = &\int_S \frac{\partial F_{S_i}}{\partial v_k} n_i \frac{\partial v_k}{\partial b_n} dS + \int_S \frac{\partial F_{S_i}}{\partial p} n_i \frac{\partial p}{\partial b_n} dS + \int_S \frac{\partial F_{S_i}}{\partial \tau_{kj}} n_i \frac{\partial \tau_{kj}}{\partial b_n} dS \\ &+ \int_S \frac{\partial F_{S_i}}{\partial \widetilde{\nu}} n_i \frac{\partial \widetilde{\nu}}{\partial b_n} dS + \int_S n_i \frac{\partial F_{S_i}}{\partial x_m} \frac{\delta x_k}{\delta b_n} n_k dS \\ &+ \int_S F_{S_i} \frac{\delta n_i}{\delta b_n} dS + \int_S F_{S_i} n_i \frac{\delta (dS)}{\delta b_n} \end{aligned} \tag{4.35}$$

By using differential geometry we could further express the derivatives of the geometrical quantities that appear in eq. 4.35 as

$$\frac{\delta n_i}{\delta b_n} = -\frac{\partial_t}{\partial x_i}\left(\frac{\delta x_k}{\delta b_n} n_k\right) \tag{4.36}$$

$$\frac{\delta (dS)}{\delta b_n} = -k \frac{\delta x_k}{\delta b_n} n_k dS \tag{4.37}$$

where $\partial_t()/\partial x_i$ denotes the tangential derivative and k the mean curvature of the surface. Computing the mean curvature k though is not a trivial task, especially on unstructured meshes. Furthermore, even though the tangential derivative of any quantity Φ that can be defined on a surface S and its ambient space can be expressed as

$$\frac{\partial_t \Phi}{\partial x_i} = \frac{\partial \Phi}{\partial x_i} - \frac{\partial \Phi}{\partial x_m} n_m n_i \tag{4.38}$$

this cannot be done for the mesh deformation velocity $(\delta x_k/\delta b_n)n_k$, since it can only be defined on the wall surface S_{W_P}, but not its ambient space [19]. For these reasons, in a discrete sense, eq. 4.35 stays as it is and the terms $\delta n_i/\delta b_n$ and $\delta(dS)/\delta b_n$ can alternatively be evaluated by finite differences.

Volume Integral of eq. 4.34

After applying Leibniz theorem for the differentiation of the integral terms with moving boundaries ($S = S(\mathbf{b}) = \partial\Omega$) we obtain

$$\frac{\delta}{\delta b_n}\int_\Omega F_\Omega d\Omega = \int_\Omega \frac{\partial F_\Omega}{\partial b_n} d\Omega + \int_S F_\Omega n_k \frac{\delta x_k}{\delta b_n} dS \tag{4.39}$$

Eq. 4.39 can further be expanded by taking into consideration the dependency of F on the state variables $\mathbf{U}$. Generally, F may be expressed in terms of flow variables v_i, p or turbulence model variables (e.g. k, ω, $\widetilde{\nu}$) , but also in terms of differential expressions of these quantities (e.g. the stress tensor τ_{ij}). Therefore, considering that $F = F(\mathbf{b}, \mathbf{U}(\mathbf{b}))$ with $\mathbf{U}(\mathbf{b}) = (v_i, p, \widetilde{\nu})$, eq. 4.39 takes the form

$$\begin{aligned}\frac{\delta}{\delta b_n}\int_\Omega F_\Omega d\Omega = &\int_\Omega \acute{F}^v_{\Omega,i}\frac{\partial v_i}{\partial b_n}d\Omega + \int_\Omega \acute{F}^p_\Omega \frac{\partial p}{\partial b_n}d\Omega + \int_\Omega \acute{F}^{\widetilde{\nu}}_\Omega \frac{\partial \widetilde{\nu}}{\partial b_n}d\Omega + \int_S \acute{F}^v_{S,i}\frac{\partial v_i}{\partial b_n}dS \\ &+ \int_S \acute{F}^p_S \frac{\partial p}{\partial b_n}dS \int_S \acute{F}^{\widetilde{\nu}}_S \frac{\partial \widetilde{\nu}}{\partial b_n}dS \int_S F_\Omega n_k \frac{\delta x_k}{\delta b_n}dS\end{aligned} \tag{4.40}$$

where $\acute{F}^\Phi_\Omega$ includes the partial derivative $\partial F_\Omega/\partial\Phi$ plus any term that might result from the use of Gauss divergence theorem for integrals of the form $\int_\omega \frac{\partial}{\partial b_n}\left(\frac{\partial \Phi}{\partial x_j}\right)d\Omega$.

By substituting these final surface and volume integral expressions in eq. 4.34, the final expression of $\delta F/\delta b_n$ results to

$$\begin{aligned}\frac{\delta F}{\delta b_n} = &\int_\Omega \acute{F}^v_{\Omega,i}\frac{\partial v_i}{\partial b_n}d\Omega + \int_\Omega \acute{F}^p_\Omega \frac{\partial p}{\partial b_n}d\Omega + \int_\Omega \acute{F}^{\widetilde{\nu}}_\Omega \frac{\partial \widetilde{\nu}}{\partial b_n}d\Omega + \int_S \left(\acute{F}^v_{S,i} + \frac{\partial F_{S_k}}{\partial v_i}n_k\right)\frac{\partial v_i}{\partial b_n}dS \\ &+ \int_S \left(\acute{F}^p_S + \frac{\partial F_{S_i}}{\partial p}n_i\right)\frac{\partial p}{\partial b_n}dS + \int_S \left(\acute{F}^{\widetilde{\nu}}_S + \frac{\partial F_{S_i}}{\partial \widetilde{\nu}}n_i\right)\frac{\partial \widetilde{\nu}}{\partial b_n}dS \\ &+ \int_S \frac{\partial F_{S_k}}{\partial \tau_{ij}}n_k\frac{\partial \tau_{ij}}{\partial b_n}dS + \int_{S_{W_p}} F_\Omega n_k \frac{\delta x_k}{\delta b_n}dS + \int_{S_{W_p}} n_i \frac{\partial F_{S_{W_p,i}}}{\partial x_m}n_m\frac{\delta x_k}{\delta b_n}n_k dS \\ &+ \int_{S_{W_p}} F_{S_{W_p,i}}\frac{\delta n_i}{\delta b_n}dS + \int_{S_{W_p}} F_{S_{W_p,i}}n_i\frac{\delta(dS)}{\delta b_n}\end{aligned} \tag{4.41}$$

Eq. 4.41 contains the partial derivatives of the flow variables $\mathbf{U}$ w.r.t. the design variables b_n which would typically require the solution of N systems of equations, similar to the Navier-Stokes ones with a cost approximately of N EFS. To reduce this great computational cost, one should formulate and numerically solve the adjoint field equations.

The aforementioned analysis of differentiating a general objective function will be applied to the wind noise objective function that concerns this diploma thesis.

Surrogate Noise Objective Function

Whilst noise is an inherentely unsteady phenomenon, the application of an unsteady optimization workflow is practically too expensive, if not impossible, in an industrial enviroment. For this reason, a surrogate model expressing the generation of wind noise in an incompressible and steady-state manner is used as the objective function of the optimization process.

According to Proudman's model [38], the acoustic power generated by isotropic turbulence can by derived from Lighthill's theory of aerodynamic noise. Proudman's formula, in turn, can be correlated to the turbulent kinetic energy and dissipation or the levels of turbulent viscosity.

Based on industrial experience, an objective function which is linked to the noise perceived by the driver of a car and which depends exclusively on the turbulence viscosity is given by [4]

$$F_\nu = \int_{\Omega'} \nu_t^2 d\Omega \tag{4.42}$$

where ν_t is the turbulent viscocity and Ω' is a volume residing next to the driver's window with a user-defined thickness.

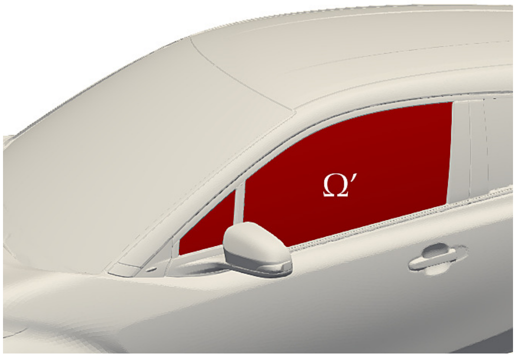

Figure 4.3: *Finite volume Ω' used for the definition of the surrogate noise objective function 4.42. The volume is residing next to the driver's window and has a user-defined finite thickness.*

By utilizing the objective function of eq. 4.42, one wishes to reduce noise by exclusively using a steady-state flow solver (to obtain the ν_t field), without coupling it with an acoustic one. Furthermore, since ν_t is only obtained by solving a turbulence model, it is necessary to differentiate the turbulence model in the adjoint formulation, in order to secure accurate sensitivity derivatives, while otherwise these would have a zero value irrespectively of the body's shape.

Differentiating eq. 4.42 w.r.t. the design variables b_n and applying Leibniz's theorem results to

$$\begin{aligned}\frac{\delta F_\nu}{\delta b_n} &= \frac{\delta}{\delta b_n}\int_{\Omega'} \nu_t^2 d\Omega = \int_{\Omega'} \frac{\partial \nu_t^2}{\partial b_n} d\Omega + \int_{S'} \nu_t^2 n_k \frac{\delta x_k}{\delta b_n} dS \\ &= \int_{\Omega'} \underbrace{2\nu_t \frac{\partial \nu_t}{\partial \widetilde{\nu}}}_{\acute{F}_{\Omega}^{\widetilde{\nu}}} \frac{\partial \widetilde{\nu}}{\partial b_n} d\Omega + \int_{S'} \nu_t^2 n_k \frac{\delta x_k}{\delta b_n} dS\end{aligned} \tag{4.43}$$

where $S^{'}$ is the surface corresponding to the residing volume $\Omega^{'}$. Eq. **4.43** implies that an extra source term $\acute{F}_{\Omega}^{\widetilde{\nu}}$ must be added to the adjoint turbulence model equation, in the cells contained within $\Omega^{'}$.

4.2.4 Derivation of the Field Adjoint Equations

By looking back at eq. **4.26**, in order to reach a final expression for $\delta L/\delta b_n$ we must further develop the terms $\partial R^p/\partial b_n$, $\partial R_i^v/\partial b_n$ and $\partial R^{\widetilde{\nu}}/\partial b_n$, i.e. the partial derivatives of the state equations w.r.t. the design variables.

Therefore, by differentiating the Navier-Stokes continuity **4.16a** and momentum **4.16b** equations we get

$$\frac{\partial R^p}{\partial b_n} = -\frac{\partial}{\partial x_j}\left(\frac{\partial v_j}{\partial b_n}\right) \tag{4.44}$$

and

$$\begin{aligned}\frac{\partial R_i^v}{\partial b_n} = {} & \frac{\partial v_j}{\partial b_n}\frac{\partial v_i}{\partial x_j} + v_j\frac{\partial}{\partial x_j}\left(\frac{\partial v_i}{\partial b_n}\right) + \frac{\partial}{\partial x_i}\left(\frac{\partial p}{\partial b_n}\right) \\ & - \frac{\partial}{\partial x_j}\left[(\nu+\nu_t)\frac{\partial}{\partial b_n}\left(\frac{\partial v_i}{\partial x_j}+\frac{\partial v_j}{\partial x_i}\right)\right] - \frac{\partial}{\partial x_j}\left[\frac{\partial \nu_t}{\partial b_n}\left(\frac{\partial v_i}{\partial x_j}+\frac{\partial v_j}{\partial x_i}\right)\right]\end{aligned} \tag{4.45}$$

where the differential operator $\partial()/\partial b_n$ was conveniently interchanged with the operator $\partial()/\partial x_j$, according to eq. **4.31**.

In order to analyze the term $\partial \nu_t/\partial b_n$ appearing in eq. **4.45**, we need to express ν_t in terms of the state variables through the turbulence model. For the Spalart-Allmaras model used in this thesis, we have

$$\frac{\partial \nu_t}{\partial b_n} = \frac{\partial \nu_t}{\partial \widetilde{\nu}}\frac{\partial \widetilde{\nu}}{\partial b_n} \quad \text{, with} \quad \frac{\partial \nu_t}{\partial \widetilde{\nu}} = f_{v_1} + \widetilde{\nu}\frac{\partial f_{v_1}}{\partial \widetilde{\nu}} = f_{v_1} + \frac{3c_{v_1}^3\chi^2}{\left(\chi^3+c_{v_1}^3\right)^2} \tag{4.46}$$

Subsequently, by differentiating the Spalart-Allmaras turbulence model of eq. **4.16c**, one gets

$$\begin{aligned}\frac{\delta R^{\widetilde{\nu}}}{\delta b_n} = {} & \frac{\partial \widetilde{\nu}}{\partial x_j}\frac{\partial v_j}{\partial b_n} + v_j\frac{\partial}{\partial x_j}\left(\frac{\partial \widetilde{\nu}}{\partial b_n}\right) - \frac{\partial}{\partial x_j}\left[\left(\nu+\frac{\widetilde{\nu}}{\sigma}\right)\frac{\partial}{\partial x_j}\frac{\partial \widetilde{\nu}}{\partial b_n}\right] \\ & - \frac{1}{\sigma}\frac{\partial}{\partial x_j}\left(\frac{\partial \widetilde{\nu}}{\partial b_n}\frac{\partial \widetilde{\nu}}{\partial x_j}\right) - 2\frac{c_{b2}}{\sigma}\frac{\partial \widetilde{\nu}}{\partial x_j}\frac{\partial}{\partial x_j}\left(\frac{\partial \widetilde{\nu}}{\partial b_n}\right) \\ & + \widetilde{\nu}\left(-\frac{\partial P}{\partial b_n}+\frac{\partial D}{\partial b_n}\right) + (-P+D)\frac{\partial \widetilde{\nu}}{\partial x_j}\end{aligned} \tag{4.47}$$

Differentiating the production P and destruction D terms of the model w.r.t. design variables b_n yields

$$-\frac{\partial P}{\partial b_n}+\frac{\partial D}{\partial b_n}=\mathcal{C}_{\widetilde{\nu}}\frac{\partial\widetilde{\nu}}{\partial b_n}+\mathcal{C}_\Delta\frac{\partial\Delta}{\partial b_n}+\mathcal{C}_Y\frac{1}{Y}e_{mjk}\frac{\partial v_k}{\partial x_j}e_{mli}\frac{\partial}{\partial b_n}\left(\frac{\partial v_i}{\partial x_l}\right) \tag{4.48}$$

The Δ term appearing in eq. 4.47 corresponds to the distance from the wall boundaries [4], introduced by the Spalart-Allmaras turbulence model. Its derivative $\partial\Delta/\partial b_n$ requires further treatement, covered in section 4.2.6. The $\mathcal{C}_{\widetilde{\nu}}$, $\mathcal{C}_\Delta$ and $\mathcal{C}_Y$ are the derived coefficients equivalent to

$$\mathcal{C}_Y=\left(-c_{b_1}-c_{w_1}\mathcal{C}\frac{r}{\widetilde{Y}}\right)f_{v_3} \tag{4.49}$$

$$\mathcal{C}_\Delta=-\frac{2}{\Delta^3}\left[c_{w_1}r\,\mathcal{C}\left(\Delta^2-\frac{\widetilde{\nu}f_{v_2}}{\kappa^2\widetilde{Y}}\right)+c_{w_1}f_w\widetilde{\nu}-c_{b_1}\frac{f_{v_2}}{\kappa^2}\widetilde{\nu}\right] \tag{4.50}$$

$$\mathcal{C}_{\widetilde{\nu}}=\left(-c_{b_1}-c_{w_1}\mathcal{C}\frac{r}{\widetilde{Y}}\right)\left(\frac{\partial f_{v_3}}{\partial\widetilde{\nu}}Y+\frac{f_{v_2}}{\kappa^2\Delta^2}+\frac{\partial f_{v_2}}{\partial\widetilde{\nu}}\frac{\widetilde{\nu}}{\kappa^2\Delta^2}\right)+c_{w_1}\mathcal{C}\frac{r}{\widetilde{\nu}}+c_{w_1}\frac{f_w}{\Delta^2} \tag{4.51}$$

$$C=\frac{c_{w_1}\widetilde{\nu}^2}{\Delta^2}\left[1+c_{w_2}(6r^5-1)\right]\frac{c_{w_3}^6}{g^6+c_{w_3}^6}\left(\frac{1+c_{w_3}^6}{g^6+c_{w_3}^6}\right)^{1/6} \tag{4.52}$$

$$\frac{\partial f_{v_2}}{\partial\widetilde{\nu}}=-\frac{3}{\nu c_{v_2}}\left(1+\frac{\chi}{c_{v_2}}\right)^{-4} \tag{4.53}$$

$$\begin{aligned}\frac{\partial f_{v_3}}{\partial\widetilde{\nu}}=&\frac{1}{c_{v_2}}\left(\frac{f_{v_1}}{\nu}+\chi\frac{\partial f_{v_1}}{\partial\nu}\right)\left[3\left(1+\frac{\chi}{c_{v_2}}\right)+\left(\frac{\chi}{c_{v_2}}\right)^2\right]\left(1+\frac{\chi}{c_{v_2}}\right)^{-3}\\&+\frac{1}{\nu c_{v_2}^2}(1+\chi f_{v_1})\left(3+2\frac{\chi}{c_{v_2}}\right)c_{v_2}^2\left(1+\frac{\chi}{c_{v_2}}\right)^{-3}\\&-3\frac{(1+\chi f_{v_1})}{\nu c_{v_2}^2}\left[3\left(1+\frac{\chi}{c_{v_2}}\right)+\left(\frac{\chi}{c_{v_2}}\right)^2\right]\left(1+\frac{\chi}{c_{v_2}}\right)^{-4}\end{aligned} \tag{4.54}$$

The differentiation of the turbulence model's equation allows us to take into consideration any variation in the flow's turbulence, due to the deformations of the geometry's shape. Therefore, it is emphasized that obtaining adjoint-based sensitivities for the specific objective function would not have been possible without a full differentiation of the turbulence model, since otherwise, the acquired sensitivities would have zero values irrespectively of the geometry's shape. A more complete and in-detail presentation of the adjoint formulation to the Spalart-Allmaras model can be found in [19, 39].

---

[4] The same term in eq. 4.8 was labeled as d, to differ from the mesh size length Δ.

Subsequently, by substituting eqs. **4.44**, **4.45** and **4.47** into the expression of eq. **5.7**, we obtain the final expression of the material derivative of the augmented objective function w.r.t. the design variables

$$\begin{aligned}
\frac{\delta L}{\delta b_n} = & \int_S \mathcal{BC}_i^u \frac{\partial v_i}{\partial b_n} dS + \int_S \mathcal{BC}^p \frac{\partial p}{\partial b_n} dS + \int_S \mathcal{BC}^{\widetilde{\nu_a}} \frac{\partial \widetilde{\nu}}{\partial b_n} dS + \int_S \mathcal{BC}^{m_a} \frac{\partial}{\partial x_j} \left(\frac{\delta x_i}{\delta b_n} \right) dS \\
& + \int_S (-u_i n_j + \frac{\partial F_{S_k}}{\partial \tau_{ij}} n_k) \frac{\partial \tau_{ij}}{\partial b_n} dS - \int_S \widetilde{\nu_a} \left(\nu + \frac{\widetilde{\nu}}{\sigma} \right) \frac{\partial}{\partial b_n} \left(\frac{\partial \widetilde{\nu}}{\partial x_j} \right) n_j dS \\
& + \int_\Omega R_i^u \frac{\partial v_i}{\partial b_n} d\Omega + \int_\Omega R^q \frac{\partial p}{\partial b_n} d\Omega + \int_\Omega R^{\widetilde{\nu_a}} \frac{\partial \widetilde{\nu}}{\partial b_n} d\Omega + \int_\Omega R_k^{m^a} \frac{\delta x_k}{\delta b_n} d\Omega \\
& + \int_{S_{W_p}} n_i \frac{\partial F_{S_{W_p,i}}}{\partial x_m} n_m \frac{\delta x_k}{\delta b_n} n_k dS + \int_{S_{W_p}} F_{S_{W_p,i}} \frac{\delta n_i}{\delta b_n} dS + \int_{S_{W_p}} F_{S_{W_p,i}} n_i \frac{\delta (dS)}{\delta b_n} \\
& - \int_{S_{W_P}} \frac{\partial m_i^a}{\partial x_j} n_j \frac{\delta x_i}{\delta b_n} dS + \int_\Omega \widetilde{\nu} \widetilde{\nu_a} \mathcal{C}_\Delta \frac{\partial \Delta}{\partial b_n} d\Omega + \int_S m_i^a R_i^m n_k \frac{\delta x_k}{\delta b_n} dS
\end{aligned} \tag{4.55}$$

where

$$\begin{aligned}
\mathcal{BC}_i^u = & u_i v_j n_j + (\nu + \nu_t) \left(\frac{\partial u_i}{\partial x_j} + \frac{\partial u_j}{\partial x_i} \right) n_j - q n_i + \widetilde{\nu_a} \widetilde{\nu} \frac{\mathcal{C}_Y}{Y} e_{mjk} \frac{\partial v_k}{\partial x_j} e_{mli} n_l \\
& + \frac{\partial F_{S_k}}{\partial v_i} n_k + \acute{F}_{S,i}^v
\end{aligned} \tag{4.56}$$

$$\mathcal{BC}^p = u_j n_j + \frac{\partial F_{S_i}}{\partial p} n_i + \acute{F}_S^p \tag{4.57}$$

$$\mathcal{BC}^{\widetilde{\nu_a}} = \widetilde{\nu_a} v_j n_j + \left(\nu + \frac{\widetilde{\nu}}{\sigma} \right) \frac{\partial \widetilde{\nu_a}}{\partial x_j} n_j - \frac{\widetilde{\nu_a}}{\sigma} (1 + 2 c_{b_2}) \frac{\partial \widetilde{\nu}}{\partial x_j} n_j + \frac{\partial F_{S_k}}{\partial \widetilde{\nu}} n_k + \acute{F}_S^{\widetilde{\nu}} \tag{4.58}$$

$$\mathcal{BC}^{m_a} = m_i^a n_j \tag{4.59}$$

As already mentioned, the aim of the adjoint method is to bypass the expensive computation of expressions of the form $\partial \mathbf{U} / \partial b_n$, i.e. the derivatives of state variables $\mathbf{U}$ w.r.t. the design variables b_n .

This can be accomplished by setting the multipliers of $\partial v_i / \partial b_n$, $\partial p / \partial b_n$, $\partial \widetilde{\nu} / \partial b_n$ and $\delta x_k / \delta b_n$, in the volume integrals of eq. **4.55** to zero, or

$$R^q = - \frac{\partial u_j}{\partial x_j} + \acute{F}_\Omega^p = 0 \tag{4.60}$$

$$\begin{aligned}
R_i^u = & u_j \frac{\partial v_j}{\partial x_i} - \frac{\partial (v_j u_i)}{\partial x_j} - \frac{\partial}{\partial x_j} \left[(\nu + \nu_t) \left(\frac{\partial u_i}{\partial x_j} + \frac{\partial u_j}{\partial x_i} \right) \right] + \frac{\partial q}{\partial x_i} + \acute{F}_{\Omega,i}^v \\
& + \widetilde{\nu_a} \frac{\partial \widetilde{\nu}}{\partial x_i} - \frac{\partial}{\partial x_l} \left(\widetilde{\nu_a} \widetilde{\nu} \frac{\mathcal{C}_Y}{Y} e_{mjk} \frac{\partial v_k}{\partial x_j} e_{mli} \right) = 0 \ , \ i = 1, 2, 3
\end{aligned} \tag{4.61}$$

$$\begin{aligned} R^{\widetilde{\nu_a}} = & -\frac{\partial(v_j\widetilde{\nu_a})}{\partial x_j} - \frac{\partial}{\partial x_j}\left[\left(\nu+\frac{\widetilde{\nu}}{\sigma}\right)\frac{\partial\widetilde{\nu_a}}{\partial x_j}\right] + \frac{1}{\sigma}\frac{\partial\widetilde{\nu_a}}{\partial x_j}\frac{\partial\widetilde{\nu}}{\partial x_j} + 2\frac{c_{b2}}{\sigma}\frac{\partial}{\partial x_j}\left(\widetilde{\nu_a}\frac{\partial\widetilde{\nu}}{\partial x_j}\right) \\ & +\widetilde{\nu_a}\widetilde{\nu}\mathcal{C}_{\widetilde{\nu}} + \frac{\partial\nu_t}{\partial\widetilde{\nu}}\frac{\partial u_i}{\partial x_j}\left(\frac{\partial v_i}{\partial x_j}+\frac{\partial v_j}{\partial x_i}\right) + (-P+D)\,\widetilde{\nu_a} + \acute{F}_{\Omega}^{\widetilde{\nu}} = 0 \end{aligned} \tag{4.62}$$

$$R_k^{m^a} = \frac{\partial^2 m_k^a}{\partial x_j^2} + \frac{\partial}{\partial x_j}\left\{u_i v_j\frac{\partial v_i}{\partial x_k} + u_j\frac{\partial p}{\partial x_k} + \tau_{ij}^a\frac{\partial u_i}{\partial x_k} - u_i\frac{\partial\tau_{ij}}{\partial x_k} - q\frac{\partial v_j}{\partial x_k}\right\} = 0 \tag{4.63}$$

The aforementioned system of PDEs consitutes the Field Adjoint Equations (FAE). Specifically, the first two equations constitute the adjoint Navier-Stokes equations, eq. **4.62** the adjoint Spalart-Allmaras model [5] and eq. **4.63** the adjoint grid displacement equation. The FAE relate quite a lot the primal equations; e.g. the adjoint continuity equation **4.60** remains the same, whilst the adjoint momentum equation **4.61** comprises similar convection, diffusion and adjoint pressure gradient terms. Nevertheless, eq. **4.61** contains an extra non-conservative "adjoint transpose convection" term, which combined with the nature of the adjoint boundary conditions, renders convergence a difficult challenge.

4.2.5 Adjoint Boundary Conditions

The system of the field adjoint PDEs is a closed system with its own corresponding adjoint boundary conditions (ABC). The ABCs are obtained similarly, by setting the multipliers of the surface integrals which contain $\partial\mathbf{U}/\partial b_n$ terms to zero. We may name these surface integral terms of eq. **4.55** as

$$I_1 = \int_S \mathcal{BC}_i^u \frac{\partial v_i}{\partial b_n} dS \tag{4.64}$$

$$I_2 = \int_S \mathcal{BC}^p \frac{\partial p}{\partial b_n} dS \tag{4.65}$$

$$I_3 = \int_S \mathcal{BC}^{\widetilde{\nu_a}} \frac{\partial\widetilde{\nu}}{\partial b_n} dS \tag{4.66}$$

$$I_4 = \int_S \mathcal{BC}^{m_a} \frac{\partial}{\partial x_j}\left(\frac{\delta x_i}{\delta b_n}\right) dS \tag{4.67}$$

$$I_5 = \int_S (-u_i n_j + \frac{\partial F_{S_k}}{\partial\tau_{ij}} n_k)\frac{\partial\tau_{ij}}{\partial b_n} dS \tag{4.68}$$

$$I_6 = \int_S \widetilde{\nu_a}\left(\nu+\frac{\widetilde{\nu}}{\sigma}\right)\frac{\partial}{\partial b_n}\left(\frac{\partial\widetilde{\nu}}{\partial x_j}\right) n_j dS \tag{4.69}$$

$$I_7 = \int_S m_i^a R_i^m n_k \frac{\delta x_k}{\delta b_n} dS \tag{4.70}$$

---

[5] The extra source term $\acute{F}_{\Omega}^{\widetilde{\nu}}$ only applies for the cells contained within the volume Ω'

Developing these terms depends on the type of the boundary surface S. Nevertheless, the boundary condition of the adjoint grid discplacement PDEs is the same regardless of the boundary's type, namely $m_k^a = 0$, so that the term I_4 can vanish. Additionally, the term I_7 containing the term m_k^a also gets vanished along all boundaries S.

What follows is a distinction between the adjoint boundary conditions, regarding the different types of boundaries. A more complete presentation of the adjoint boundary conditions can be found in [19].

Inlet Boundaries S_I

At the inlet boundaries S_I, a Dirichlet boundary condition is imposed for the velocity component u_i (and thus $\delta u_i/\delta b_n$), while a zero Neumann condition is used for the pressure p. Since S_I is fixed, $\delta x_k/\delta b_n = 0$. After taking into consideration eq. 4.30, $\partial v_i/\partial b_n = 0$ and $\partial \widetilde{\nu}/\partial b_n = 0$ is also valid. This means that $I_1 = I_3 = 0$.

Integrals I_2 and I_5 are eliminated by demanding

$$u_{\langle n \rangle} = -\frac{\partial F_{S_I,j}}{\partial p} n_j \tag{4.71a}$$

$$u_{\langle t \rangle}^{I} = \frac{\partial F_{S_I,k}}{\partial \tau_{ij}} n_k t_i^I n_j + \frac{\partial F_{S_I,k}}{\partial \tau_{ij}} n_k t_j^I n_i \tag{4.71b}$$

$$u_{\langle t \rangle}^{II} = \frac{\partial F_{S_I,k}}{\partial \tau_{ij}} n_k t_i^{II} n_j + \frac{\partial F_{S_I,k}}{\partial \tau_{ij}} n_k t_j^{II} n_i \tag{4.71c}$$

where t_i^I, t_i^{II} are the components of the tangent to the surface unit vectors. The first tangent vector t_i^I is an arbitrary vector parallel to S_I whereas t_i^{II} is orthogonal to n_i and t_i^I and is given by $t_i^{II} = e_{ijk} n_j t_k^I$. The velocity component $\boldsymbol{u}$ is analyzed into its components $u_{\langle t \rangle}^{I}$ and $u_{\langle t \rangle}^{II}$ along the directions t_i^I and t_i^{II} respectively.

The integral term I_6 is elliminated by imposing a zero Dirichlet condition on $\widetilde{\nu_a}$, whereas, since no boundary condition arises for q by the aforementioned ellimination of these integral terms, a zero Neumann boundary condition is chosen for the adjoint pressure q.

Outlet Boundaries S_O

On the outlet boundaries S_O, a Dirichlet boundary condition is imposed on the pressure and zero Neumann conditions are imposed on the velocity components. Similar to the inlet boundary, the outlet boundary is fixed, or $\delta x_k/\delta b_n = 0$ and by taking into consideration eq. 4.30, $\partial p/\partial b_n = 0$ also holds. Consequently, integral I_2 along S_O vanishes automatically. Due to the distance of the outlet boundary from the controlled area, an almost a uniform velocity profile can be assumed along S_O. The latter implies that $\delta\tau_{ij}/\delta b_n = 0$ along S_0 and therefore integral I_5 can also be neglected.

In order to eliminate I_1, its integrand should be set to zero, or

$$\begin{aligned}\mathcal{BC}_i^u = {} & u_i v_j n_j + (\nu + \nu_t)\left(\frac{\partial u_i}{\partial x_j} + \frac{\partial u_j}{\partial x_i}\right) n_j - q n_i + \widetilde{\nu_a}\widetilde{\nu}\frac{\mathcal{C}_Y}{Y} e_{mjk}\frac{\partial v_k}{\partial x_j} e_{mli} n_l \\ & + \frac{\partial F_{S_k}}{\partial v_i} n_k + \acute{F}^v_{S,i} = 0, \qquad i = 1,2,3 \end{aligned} \tag{4.72}$$

Eq. **4.72** comprises three PDEs which, in turn, include four unknown quantities (the three adjoint velocity components and the adjoint pressure). Therefore, one of them should be extrapolated from the interior of the domain. This is chosen to be the normal component of the adjoint velocity, $u_{\langle n \rangle}$.

By multiplying eq. **4.72** with n_i, we obtain an expression for the adjoint pressure

$$\begin{aligned} q = {} & u_{\langle n \rangle} v_{\langle n \rangle} + 2(\nu + \nu_t)\frac{\partial u_{\langle n \rangle}}{\partial n} + \frac{\partial F_{S_{O,k}}}{\partial v_i} n_i n_k + \acute{F}^v_{S_{O,i}} n_i \\ & + \widetilde{\nu_a}\widetilde{\nu}\frac{\mathcal{C}_Y}{Y} e_{mjk}\frac{\partial v_k}{\partial x_j} e_{mli} n_l n_i = 0 \end{aligned} \tag{4.73}$$

The adjoint tangential velocity component can be obtained by multiplying eq. **4.72** with the tangent to the surface vectors t_i^l , $l=1,2$.

$$\begin{aligned} & v_{\langle t \rangle} u^l_{\langle t \rangle} + (\nu + \nu_t)\left(\frac{\partial u^l_{\langle t \rangle}}{\partial n} + \frac{\partial u_{\langle n \rangle}}{\partial t^l}\right) + \frac{\partial F_{S_{O,k}}}{\partial v_i} n_k t_i^l + \acute{F}^v_{S_{O,i}} t_i^l \\ & - \widetilde{\nu_a}\widetilde{\nu}\frac{\mathcal{C}_Y}{Y} e_{mjk}\frac{\partial v_k}{\partial x_j} e_{mzi} n_z t_i^l = 0 \ , \ l=1,2 \end{aligned} \tag{4.74}$$

Finally, a Robin-type boundary condition is imposed on $\widetilde{\nu_a}$ in order to eliminate integral I_3, as

$$BC^{\widetilde{\nu_a}} = \widetilde{\nu_a} v_j n_j + \left(\nu + \frac{\widetilde{\nu}}{\sigma}\right)\frac{\partial \widetilde{\nu_a}}{\partial x_j} n_j + \frac{\partial F_{S_{O,k}}}{\partial \widetilde{\nu}} n_k + \acute{F}^{\widetilde{\nu}}_{S_O} = 0 \tag{4.75}$$

where the term $\widetilde{\nu_a}/\sigma\,(1 + 2c_{b_2})\,\frac{\partial \widetilde{\nu}}{\partial x_j} n_j$ found in eq. **4.58** where $BC^{\widetilde{\nu_a}}$ was initially defined, has been elliminated from **4.75** due to the zero Neumann boundary condition imposed on $\widetilde{\nu}$ for the outlet boundaries S_O.

Unparameterized/Fixed Wall Boundaries S_W

Alongside S_W, the imposed boundary conditions for the state variables are the same as those used at the inlet, i.e. Dirichlet boundary conditions for the velocity component and a zero Neumann boundary condition for the pressure. By taking into consideration that $\delta x_k/\delta b_n = 0$ for the S_W boundaries, the following conditions for the adjoint velocity are derived

$$u_{\langle n\rangle} = -\frac{\partial F_{S_W,j}}{\partial p} n_j \tag{4.76a}$$

$$u^I_{\langle t\rangle} = \frac{\partial F_{S_W,k}}{\partial \tau_{ij}} n_k t^I_i n_j + \frac{\partial F_{S_W,k}}{\partial \tau_{ij}} n_k t^I_j n_i \tag{4.76b}$$

$$u^{II}_{\langle t\rangle} = \frac{\partial F_{S_W,k}}{\partial \tau_{ij}} n_k t^{II}_i n_j + \frac{\partial F_{S_W,k}}{\partial \tau_{ij}} n_k t^{II}_j n_i \tag{4.76c}$$

along with a zero Neumann condition for the adjoint pressure q. Furthermore, we know that $\widetilde{\nu}$ is equal to zero on the wall boundaries, hence integral I_3 vanishes automatically. However, this is not the case for the gradient of $\widetilde{\nu}$. The integral I_6 is elliminated by imposing a zero Dirichlet boundary condition on $\widetilde{\nu_a}$.

For the wall boundaries, it is often useful to define t^I_i to be parallel to the primal velocity vector direction at the first cell centre adjacent to the wall P, i.e. $t^I_i = u^P_i / \left\|\mathbf{v^P}\right\|$ [19], as shown in fig. 4.4.

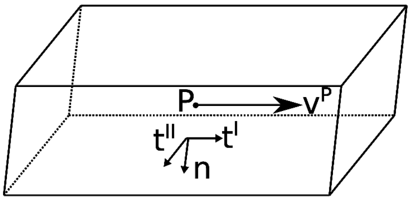

Figure 4.4: *Representation of a finite volume adjacent to the wall, where* $\boldsymbol{n}$ *is the outwards normal unit vector,* $\boldsymbol{t^I}$ *is parallel to the velocity vector at the first cell centre* P *and* $t^{II}_i = e_{ijk} n_j t^I_k$. *[19].*

Parameterized/Controlled Wall Boundaries S_{W_P}

The controlled wall boundaries S_{W_P}, are the boundaries of the domain that may change during the optimization and thus $\delta x_k/\delta b_n \neq 0$. By taking into consideration eq. 4.29, we conclude that the material and partial derivatives of flow quantities are no longer identical along S_{W_P}. As a result, the total variation of the normal and tangent to the surface vectors are not zero, leading to the appearance of some extra terms during the formulation of the adjoint boundary conditions [19, 4].

4.2.6 Adjoint Wall Distance Equations

At this point, the adjoint to the wall distance equations will be derived. Foremost, it is necessary to account for the contribution of wall functions to the adjoint formulation. The wall functions are being used for the treatement of ν_t near the wall boundaries, where the objective function of eq. **4.42** is evaluated.

In view of this, after satisfying the field adjoint equations and their boundary conditions, the sensitivity derivatives eq. **4.55** yields

$$
\begin{aligned}
\frac{\delta L}{\delta b_n} = & T_{SD}^{WF} - \int_{S_{W_p}} \mathcal{SD}_1 \frac{\partial \tau_{ij}}{\partial x_m} n_j t_i^I n_m n_k \frac{\delta x_k}{\delta b_n} dS - \int_{S_{W_p}} \mathcal{SD}_1 \tau_{ij} \frac{\delta (n_j t_i^I)}{\delta b_n} \frac{\delta x_k}{\delta b_n} dS \\
& + \int_{S_{W_p}} \mathcal{SD}_{2,i} v_{\langle t \rangle}^I \frac{\delta t_i^I}{\delta b_n} dS - \int_{S_{W_p}} \mathcal{SD}_{2,i} \frac{\partial v_i}{\partial x_m} n_m n_k \frac{\delta x_k}{\delta b_n} dS \\
& - \int_{S_{W_p}} \left[\left(\nu + \frac{\widetilde{\nu}}{\sigma} \right) \frac{\partial \widetilde{\nu_a}}{\partial x_j} n_j + \frac{\partial F_{S_z}}{\partial \widetilde{\nu}} n_z + \acute{F}_S^{\widetilde{\nu}} \right] \frac{\partial \widetilde{\nu}}{\partial x_m} n_m n_k \frac{\delta x_k}{\delta b_n} dS \\
& - \int_{S_{W_p}} (-u_{\langle n \rangle} + \phi_{\langle n \rangle \langle n \rangle}) \left(\tau_{ij} \frac{\delta (n_i n_j)}{\delta b_n} + \frac{\partial \tau_{ij}}{\partial x_m} n_m \frac{\delta x_k}{\delta b_n} n_k n_i n_j \right) dS \\
& - \int_{S_{W_p}} \phi_{\langle t^I \rangle \langle t^I \rangle} \left(\tau_{ij} \frac{\delta (t_i^I t_j^I)}{\delta b_n} + \frac{\partial \tau_{ij}}{\partial x_m} n_m \frac{\delta x_k}{\delta b_n} n_k t_i^I t_j^I \right) dS \\
& - \int_{S_{W_p}} (\phi_{\langle t^{II} \rangle \langle t^I \rangle} + \phi_{\langle t^I \rangle \langle t^{II} \rangle}) \left(\tau_{ij} \frac{\delta (t_i^{II} t_j^I)}{\delta b_n} + \frac{\partial \tau_{ij}}{\partial x_m} n_m \frac{\delta x_k}{\delta b_n} n_k t_i^{II} t_j^I \right) dS \\
& - \int_{S_{W_p}} \phi_{\langle t^{II} \rangle \langle t^{II} \rangle} \left(\tau_{ij} \frac{\delta (t_i^{II} t_j^{II})}{\delta b_n} + \frac{\partial \tau_{ij}}{\partial x_m} n_m \frac{\delta x_k}{\delta b_n} n_k t_i^{II} t_j^{II} \right) dS \\
& + \int_{S_{W_p}} n_i \frac{\partial F_{S_{W_p,i}}}{\partial x_m} n_m \frac{\delta x_k}{\delta b_n} n_k dS + \int_{S_{W_p}} F_{S_{W_p,i}} \frac{\delta n_i}{\delta b_n} dS + \int_{S_{W_p}} F_{S_{W_p,i}} n_i \frac{\delta (dS)}{\delta b_n} \\
& - \int_{S_{W_P}} \frac{\partial m_i^a}{\partial x_j} n_j \frac{\delta x_i}{\delta b_n} dS + \int_{S_{W_p}} \mathcal{A}_{\Delta}^{WF} \frac{\partial \Delta^P}{\partial b_n} dS + \int_{S_W} \mathcal{A}_{\Delta}^{WF} \frac{\partial \Delta^P}{\partial b_n} dS \\
& + \left(\int_{\Omega} \widetilde{\nu} \widetilde{\nu_a} \mathcal{C}_{\Delta} \frac{\partial \Delta}{\partial b_n} d\Omega \right)_{I_\Omega}
\end{aligned}
\tag{4.77}
$$

with

$$
\mathcal{SD}_1 = -u_{\langle t \rangle}^I + \phi_{\langle t^I \rangle \langle n \rangle} + \phi_{\langle n \rangle \langle t^I \rangle} \tag{4.78}
$$

$$
\mathcal{SD}_{2,i} = (\nu + \nu_t) \left(\frac{\partial u_i}{\partial x_j} + \frac{\partial u_j}{\partial x_i} \right) n_j - q n_i + \frac{\partial F_{S_{W_p,k}}}{\partial v_i} n_k + \acute{F}_{S_{W_p,i}}^{v} \tag{4.79}
$$

$$
\phi_{ij} = \frac{\partial F_{S_{W_p,k}}}{\partial \tau_{ij}} n_k \tag{4.80}
$$

The terms T_{SD}^{WF}, $\int_{S_{W_P}} \mathcal{A}_{\Delta}^{WF} \frac{\partial \Delta^P}{\partial b_n} dS$ and $\int_{S_W} \mathcal{A}_{\Delta}^{WF} \frac{\partial \Delta^P}{\partial b_n} dS$ summarize the contribution of the wall functions differentiation to the sensitivity derivatives, based on [40].

By looking at eq. 4.77, almost all of the involved terms are surface integrals over the wall boundaries S_W and S_{W_P}. These terms can be numerically computed with no exceptional computational cost, therefore they can remain unchanged. On the contrary, the last term I_Ω is a field integral across the entire domain Ω, rendering it much more difficult to compute. Furthermore, the integrand of I_Ω contains the variation of the distance field Δ w.r.t. the design variables b_n, which is not straightforward to evaluate. One approach would be to compute $\partial \Delta / \partial b_n$ by using finite differences, i.e. by perturbating the design variables by an infinitesimally small quantity ϵ. By applying central differences, the total derivative of the distance field Δ could be assesed as

$$\frac{\delta \Delta}{\delta b_n} = \frac{\Delta(b_n + \epsilon) - \Delta(b_n - \epsilon)}{2\epsilon} \tag{4.81}$$

In turn, by taking into consideration eq. 4.29, we could compute the requested partial derivative of Δ through

$$\frac{\partial \Delta}{\partial b_n} = \frac{\delta \Delta}{\delta b_n} - \frac{\partial \Delta}{\partial x_k} \frac{\delta x_k}{\delta b_n}$$

Evaluating eq. 4.81 requires the numerical calculation of the distance field Δ for a total of two times; one for each set of the perturbated design variables. Concurrently, the distance field Δ could be calculated by measuring and storing the distances of each volume cell centre with each face centre of the boundary surface. This procedure can exert a great computational cost, especially in big mesh sizes, commonly found in industrial applications.

An alternative approach to this would be to use the eikonal equation, in order to calculate the distance field Δ. Such an equation could be the Hamilton-Jacobi equation, which gives a very good approximation to the Euclidean distance [19, 16], given by

$$\frac{\partial \Delta}{\partial x_j} \frac{\partial \Delta}{\partial x_j} = 1 \tag{4.82}$$

Eq. 4.82 constitutes a first-order non-linear partial differential equation. In order to numerically solve it by using standard finite-volume schemes, this may be transformed to

$$R^\Delta = \frac{\partial (c_j \Delta)}{\partial x_j} - \Delta \frac{\partial^2 \Delta}{\partial x_j^2} - 1 = 0 \tag{4.83}$$

with $c_j = \partial \Delta / \partial x_j$ acting as a 'convective velocity' term.

The residual eq. 4.83 should be solved alongside with the state equations, i.e. as an extra contraint of the optimization process. Based on the adjoint methodology, by satisfying the eikonal equation, we will no longer require to calculate the term $\partial\Delta/\partial b_n$.

As a result, since the primal equations are being increased by one, the augmented objective function should be defined again, in order to include the residual of the additional state equation through the volume integral term F_Δ

$$L = F + \int_\Omega u_i R_i^v d\Omega + \int_\Omega q R^p d\Omega + \int_\Omega \widetilde{\nu}_a R^{\widetilde{\nu}} d\Omega + \int_\Omega m_i^a R_i^m d\Omega + \underbrace{\int_\Omega \Delta_\alpha R^\Delta d\Omega}_{F_\Delta} \tag{4.84}$$

where Δ_a denotes the adjoint to the distance field. By differentiating the new augmented function of eq. 4.84 w.r.t. the design variables, one gets

$$\frac{\delta L}{\delta b_n} = \frac{\delta F}{\delta b_n} + \frac{\delta}{\delta b_n}\left(\int_\Omega u_i R_i^v d\Omega + \int_\Omega q R^p d\Omega + \int_\Omega \widetilde{\nu}_a R^{\widetilde{\nu}} d\Omega + \int_\Omega m_i^a R_i^m d\Omega\right) + \frac{\delta F_\Delta}{\delta b_n} \tag{4.85}$$

In eq. 4.85, all of the derivative terms have been already developed on the previous sections, except for the extra derivative term $\delta F_\Delta/\delta b_n$. In this regard, by using Leibniz's theorem on the derivative of the extra field integral we get

$$\frac{\delta F_\Delta}{\delta b_n} = \frac{\delta}{\delta b_n}\int_\Omega \Delta_a R^\Delta d\Omega = \int_\Omega \Delta_a \frac{\partial R^\Delta}{\partial b_n} d\Omega + \int_{S_{W_p}} \Delta_a R^\Delta n_k \frac{\delta x_k}{\delta b_n} dS \tag{4.86}$$

By developing the term $\partial R^\Delta/\partial b_n$, i.e. by differentiating the Hamilton-Jacobi equation and substituting it in eq. 4.86 we get

$$\frac{\delta F_\Delta}{\delta b_n} = \int_S 2\Delta_a \frac{\partial \Delta}{\partial x_j} n_j \frac{\partial \Delta}{\partial b_n} dS + \int_{S_{W_p}} \Delta_a R^\Delta n_k \frac{\delta x_k}{\delta b_n} dS - \int_\Omega 2 \frac{\partial}{\partial x_j}\left(\Delta_a \frac{\partial \Delta}{\partial x_j}\right) \frac{\partial \Delta}{\partial b_n} d\Omega \tag{4.87}$$

Finally, by substituting eq. 4.87 into eq. 4.85 and zeroing the multiplier of $\partial\Delta/\partial b_n$ in the resulting volume integrals, the field adjoint distance equation is derived, namely

$$R^{\Delta_\alpha} = -2\frac{\partial}{\partial x_j}\left(\Delta_\alpha \frac{\partial \Delta}{\partial x_j}\right) + \widetilde{\nu}\widetilde{\nu_a} C_\Delta = 0 \tag{4.88}$$

where the term $\widetilde{\nu}\widetilde{\nu_a} C_\Delta$ is contributed by the differentiation of the Spalart-Allmaras turbulence model. It should be noted that eq. 4.88 is solved at a post-processing step, after solving the coupled system of the adjoint field equations. The boundary conditions for the adjoint Hamilton-Jacobi equation can be found in [41].

Subsequently, the field integral term I_Ω in eq. 4.77 can be replaced as

$$\int_\Omega \widetilde{\nu}\widetilde{\nu_a}\mathcal{C}_\Delta \frac{\partial \Delta}{\partial b_n} d\Omega = \int_{S_{W_p}} \Delta_a R^\Delta n_k \frac{\delta x_k}{\delta b_n} dS - \int_{S_{W_p}} 2\Delta_a \frac{\partial \Delta}{\partial x_j} n_j \frac{\partial \Delta}{\partial x_m} n_m n_k \frac{\delta x_k}{\delta b_n} dS \tag{4.89}$$

4.2.7 Final Sensitivity Derivatives Expression

After taking into consideration all of the above, the final expression for the sensitivity derivatives reads

$$\begin{aligned}
\frac{\delta L}{\delta b_n} = & T_{SD}^{WF} - \int_{S_{W_p}} \mathcal{SD}_1 \frac{\partial \tau_{ij}}{\partial x_m} n_j t_i^I n_m n_k \frac{\delta x_k}{\delta b_n} dS - \int_{S_{W_p}} \mathcal{SD}_1 \tau_{ij} \frac{\delta (n_j t_i^I)}{\delta b_n} \frac{\delta x_k}{\delta b_n} dS \\
& + \int_{S_{W_p}} \mathcal{SD}_{2,i} v_{\langle t \rangle}^I \frac{\delta t_i^I}{\delta b_n} dS - \int_{S_{W_p}} \mathcal{SD}_{2,i} \frac{\partial v_i}{\partial x_m} n_m n_k \frac{\delta x_k}{\delta b_n} dS \\
& - \int_{S_{W_p}} \left[\left(\nu + \frac{\widetilde{\nu}}{\sigma} \right) \frac{\partial \widetilde{\nu_a}}{\partial x_j} n_j + \frac{\partial F_{S_z}}{\partial \widetilde{\nu}} n_z + \acute{F}_S^{\widetilde{\nu}} \right] \frac{\partial \widetilde{\nu}}{\partial x_m} n_m n_k \frac{\delta x_k}{\delta b_n} dS \\
& - \int_{S_{W_p}} (-u_{\langle n \rangle} + \phi_{\langle n \rangle \langle n \rangle}) \left(\tau_{ij} \frac{\delta (n_i n_j)}{\delta b_n} + \frac{\partial \tau_{ij}}{\partial x_m} n_m \frac{\delta x_k}{\delta b_n} n_k n_i n_j \right) dS \\
& - \int_{S_{W_p}} \phi_{\langle t^I \rangle \langle t^I \rangle} \left(\tau_{ij} \frac{\delta (t_i^I t_j^I)}{\delta b_n} + \frac{\partial \tau_{ij}}{\partial x_m} n_m \frac{\delta x_k}{\delta b_n} n_k t_i^I t_j^I \right) dS \\
& - \int_{S_{W_p}} (\phi_{\langle t^{II} \rangle \langle t^I \rangle} + \phi_{\langle t^I \rangle \langle t^{II} \rangle}) \left(\tau_{ij} \frac{\delta (t_i^{II} t_j^I)}{\delta b_n} + \frac{\partial \tau_{ij}}{\partial x_m} n_m \frac{\delta x_k}{\delta b_n} n_k t_i^{II} t_j^I \right) dS \\
& - \int_{S_{W_p}} \phi_{\langle t^{II} \rangle \langle t^{II} \rangle} \left(\tau_{ij} \frac{\delta (t_i^{II} t_j^{II})}{\delta b_n} + \frac{\partial \tau_{ij}}{\partial x_m} n_m \frac{\delta x_k}{\delta b_n} n_k t_i^{II} t_j^{II} \right) dS \\
& + \int_{S_{W_p}} n_i \frac{\partial F_{S_{W_p,i}}}{\partial x_m} n_m \frac{\delta x_k}{\delta b_n} n_k dS + \int_{S_{W_p}} F_{S_{W_p,i}} \frac{\delta n_i}{\delta b_n} dS + \int_{S_{W_p}} F_{S_{W_p,i}} n_i \frac{\delta (dS)}{\delta b_n} \\
& - \int_{S_{W_P}} \frac{\partial m_i^a}{\partial x_j} n_j \frac{\delta x_i}{\delta b_n} dS + \int_{S_{W_p}} \mathcal{A}_\Delta^{WF} \frac{\partial \Delta^P}{\partial b_n} dS + \int_{S_W} \mathcal{A}_\Delta^{WF} \frac{\partial \Delta^P}{\partial b_n} dS \\
& + \int_{S_{W_p}} \Delta_a R^\Delta n_k \frac{\delta x_k}{\delta b_n} dS - \int_{S_{W_p}} 2\Delta_a \frac{\partial \Delta}{\partial x_j} n_j \frac{\partial \Delta}{\partial x_m} n_m n_k \frac{\delta x_k}{\delta b_n} dS
\end{aligned} \tag{4.90}$$

Eq. 4.90 consitutes the sensitivity derivatives expression based on the E-SI adjoint formulation. It comprises surface integral terms over the boundaries of the domain, therefore it can be evaluated with a relatevely small computational cost. Furthermore, it is used to compute the sensitivity maps, i.e. map representations of the derivative of the objective function w.r.t. the normal displacement of the boundary wall faces.

4.3 Shape Optimization

At this stage, the sensitivity derivatives will incorporate with the optimization process. As already mentioned, the sensitivity derivatives can be used to produce the sensitivity maps, i.e. colormaps that represent the derivative of the objective function w.r.t. the surface-normal displacement of the surface grid points. Sensitivity maps give us an insight on how our goemetry should be deformed, in order to minimize or mazimize the objective function. Positive sensitivities indicate an outwards movement of the geometry whilst negative sensitivities an inwards one, based on the convention for the surface normal unit vector, facing from the fluid to the solid boundaries. In conclusion, sensitivity maps can be a powerfull tool for the engineer by providing general guidelines towards a new geometry design, that wishes to minimize the cost function.

On the other end, another effective way to utilize the sensitivity derivatives is to use them in an automatic shape morphing framework. Such a framework would require a shape morphing tool, capable of automatically deforming the geometry in the direction indicated by the sensitivity derivatives. Concurrently, the deformation of the geometry could change the mesh in two ways; either by deforming the mesh along with the geometry or by deforming the geometry alone and remeshing the resulted domain afterwards. The second approach requires an automatic mesh generator, which, in most industrial applications, is not a wise or cost-effective choice. In the case of the computational domain around the car, that concerns this thesis, a mesh deforming tool is being employed.

Specifically, a mesh parameterization and displacement strategy based on volumetric B-splines, which can be seen as a Free Form Deformation (FFD) method, is being used. The method uses a set of control points in 3D space, in the form of a structured control grid. Displacement of a control point results to deformation of the grid nodes that are under the influence of the corresponding control point. Moreover, the cost of each mesh movement is extremely small, the minimum degree of surface continuity can be defined a priori and the setup of each case is not cumbersome. The FFD tool is being coupled with the adjoint solver to form a complete optimization cycle. Both the FFD tool and the adjoint solver, as much as their coupling, have been developed in OpenFOAM© by the PCOpt/NTUA team [42].

4.3.1 Mesh Deformation Tool

The implemented FFD tool, used in this thesis, makes use of volumetric B-splines, i.e. B-splines defined in $3D$ space. In order to discuss the use of volumetric B-Splines in the morphing process, at first the $1D$ equivalent, i.e. a B-spline curve will be presented in brief. A more complete presentation on the mathematical background of B-splines can be found in [42].

B-spline curves

A B-spline curve $x(u)$, is a 2-Dimensional curve defined by $b_i, i \in [0, n]$ control points, given by

$$x(u) = \sum_{i=0}^{n} U_{i,p}(u) b_i \tag{4.91}$$

where $U_{i,p}(u)$ is the i-th basis function with a degree of p. Hereinafter, the summation sign may be dropped, in line with Einstein's convection of repeated indices.

The resulting x curve of eq. **4.91** is a piecewise polynomial function, with each polynomial having a maximum degree of p. The basis function $U_{i,p}(u)$ is defined by a set of knots in ascending order, known as the knot vector, $\xi_i, i \in [0, m], m = n + p + 1$. Knots can have a multiplicity greater than one, i.e. they can present in the knot vector more than once. Therefore, the so-called uniform knot vector

$$\boldsymbol{\xi} = [\underbrace{0, ..., 0}_{p+1}, \frac{1}{N}, ..., \frac{N-1}{N}, \underbrace{1, ..., 1}_{p+1}] \tag{4.92}$$

where $N = n - p + 1$, is used. This knot vector results to clamped curves, i.e. curves that pass through the first and last control points. The number of control points has to exceed the curve degree by at least one, i.e. $n + 1 \geq p + 1$, or $n \geq p$.

Two consecutive knots define a knot span. The zero order basis function is given by

$$U_{i,p}(u) = \begin{cases} 1, & \text{if } \xi_i < u < \xi_{i+1}. \\ 0, & \text{elsewhere.} \end{cases} \tag{4.93}$$

whereas the higher degree basis functions are given by

$$U_{i,p}(u) = \frac{u - \xi_i}{\xi_{i+p} - \xi_i} U_{i,p-1}(u) + \frac{\xi_{i+p+1} - u}{\xi_{i+p+1} - \xi_{i+p}} U_{i+1,p+1}(u) \tag{4.94}$$

where $u \in [0, 1]$. Each control point, or equivalently each basis function, is affecting only points with parametric coordinate residing residing in the $p + 1$ knot spans defined by $[\xi_i, \xi_{i+p+1})$. The very desirable property of the B-spline curves is its local support, i.e. a certain part of the curve can be morphed whilst the rest of the curve can stay intact. Moreover, the continuity of the curve can be determined a priopi; an advantageous property of a mesh movement algorithm.

Volumetric B-splines

In agreement with B-spline curves, volumetric B-splines are B-spline curves assigned in $3D$ space. The definition of a volumetric B-spline can be done through expanding the theory of B-splines in a 3 dimensional coordinate system, presented briefly below.

Let $b_m^{ijk}, m \in [1,3], i \in [0,I], j \in [0,J], k \in [0,K]$ be the Cartesian coordinates of the $ijk-th$ control point of the 3D structured control grid, where I, J and K are the number of control points per control grid direction. The Cartesian coordinates $\mathbf{x} = [x_1, x_2, x_3]^T = [x, y, z]^T$ of a CFD mesh point residing within the boundaries defined by the control grid are related to the parametric ones with the following expression.

$$x_m(u,v,w) = U_{I,pu}(u) V_{J,pv}(v) W_{L,pw}(w) b_m^{ijk} \quad , \quad m = 1,2,3 \tag{4.95}$$

where $\mathbf{u} = [u_1, u_2, u_3]^T = [u, v, w]^T$ are the mesh point parametric coordinates, U, V, W are the B-splines polynomial basis functions defined in each different direction and pu, pv, pw their respective degrees.

A mapping from $\Re^3(x,y,z) \rightarrow \Re^3(u,v,w)$ is required, in order to compute the mesh parametric coordinates. Owing to this, the volumetric B-splines can reproduce any geometric shape to machine accuracy. This is not necessarily the case, e.g. an approximate mapping $\Re^3(x,y,z) \rightarrow \Re^3(u,v,w)$ is performed in NURBS fitting.

Given the control points position, the knot vectors and the basis functions degrees, the parametric coordinates (u,v,w) of a point with Cartesian coordinates $r = [x_r, y_r, z_r]^T$ can be computed by solving the system of equations

$$\mathbf{R}(u,v,w) = \begin{bmatrix} x(u,v,w) - x_r = 0 \\ y(u,v,w) - y_r = 0 \\ z(u,v,w) - z_r = 0 \end{bmatrix} \tag{4.96}$$

where $x_m(u,v,w), \quad m = 1,2,3$ are computed through eq. 4.95, based on the given $\mathbf{b}$ values. The 3×3 system of eq. 4.96 can be solved independently for each parameterized mesh point using for example the Newton-Raphson method, after computing and inverting the Jacobian $\partial x_m / \partial u_j \ , \ m, j \in [1,3]$. The Jacobian matrix is computed analytically through a closed form expression resulting by differentiating eq. 4.95 w.r.t. the components of $\mathbf{u}$. Since the evaluation of the parametric coordinates of each point is independent from the rest of the grid points, this phase may run in parallel.

The aforementioned mapping process has to be done only once at the beginning of the optimization and thereafter eq. 4.95 can be used to compute the CFD mesh coordinates according to the values of the parametric ones at a negligible computational cost. In addition, since x_m depends only on (u,v,w) and $\mathbf{b}$, the deformed meshes are step-independent. This means that, for a given final control points position, the same mesh quality will be obtained independent of the number of steps taken to reach that position [42].

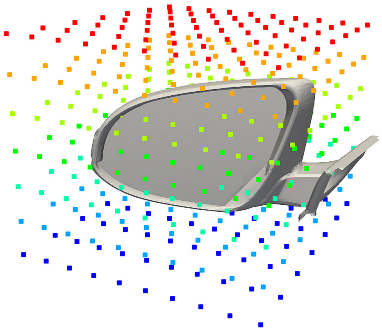

Figure 4.5: *Arbitrary control grid consisting of* $7 \times 7 \times 10$ *control points, around the car's side view mirror. Control points are coloured based their* k *value. Surface and volume mesh points residing within the boundaries of the control grid will be displaced following a possible displacement of the control points.*

The volumetric B-spline control points are arrranged in a control grid, containing the geometry that we want to modify. As a result of the $\Re^3(x,y,z) \rightarrow \Re^3(u,v,w)$ mapping, a possible displacement of the control points results to displacement of the surface and volume mesh points residing within the boundaries of the control grid.

4.3.2 Control Point Update Method

In this section, the method by which the control points are updated from one optimization cycle to the other is presented. The control point coordinates, or equivalenty the design variables, are updated according to the computed sensitivity derivatives.

There are various methods for updating the design variable components. Nevertheless, all methods update the design variables using a scheme of the form [43]

$$b_n^{new} = b_n^{old} + \eta p_n \tag{4.97}$$

where $\mathbf{b}$ are the design variables, p_n the direction which the design variables will follow and η a user-defined step length, which may be computed through.

$$\eta = \frac{\Delta b^{max}}{\Delta b^{act}} \tag{4.98}$$

where Δb^{max} is the maximum allowed displacement of the control points b_n as defined by the user and Δb^{act} is the maximum displacement of the control points as calculated from the optimization for $\eta = 1$.

In this thesis, the Fletcher-Reeves Conjugate Gradient method [32] was used to update the **b** vector of design variables. At the end of each morphing iteration, the quality of the mesh was evaluated according to the standard mesh checking routines of OpenFOAM©. The Conjucate Gradient method's mathematical background will be presented in brief. However, the simplest and most straightforward method, the Steepest Descent, will be firstly mentioned, as it forms the basis for all the other methods.

Steepest Descent

The steepest descent is the simplest and most robust gradient method. Owing to its robustness, the method is usually the first choice for use in optimization algorithms.

The basic idea of steepest descent's method is that a function F, differentiable in a neighborhood of a vector $\mathbf{b}$, decreases fastest if one goes from $\mathbf{b}$ in the direction of the negative gradient $-\nabla F(\mathbf{b})$. In that sense, the gradient $-\nabla F(\mathbf{b})$ consitutes the direction p_n that updates the vector $\mathbf{b}$. Therefore, equation 4.97 may take the form

$$b_n^{new} = b_n^{old} - \eta \frac{\delta F}{\delta b_n} \tag{4.99}$$

Steepest descent makes use of a 1st order gradient scheme and thus, depending on the case, it may fall short on accuracy. Higher order update schemes, such as the 2nd order BFGS method [33] could then be used to imporve the gradient's precision.

Conjugate Gradient

The conjugate gradient is an iterative method, used for the numerical solution of particular systems of linear equations [6]. It is commonly used to solve unconstrained linear optimization problems. The nonlinear Fletcher-Reeves conjugate method [32], which concerns this thesis, generalizes the conjugate gradient method to nonlinear optimization problems, discussed briefly below.

For a quadratic function $F(\mathbf{b}) = ||A\mathbf{b} - C||^2$, the minimum of F occurs where the gradient is equal to zero, i.e.

$$\nabla_{\mathbf{b}} F = 2A^T(A\mathbf{b} - C) = \mathbf{0} \tag{4.100}$$

---

[6] Namely those whose matrix is symmetric and positive-definite.

The gradient $\nabla_{\mathbf{b}} F$ of eq. 4.100 indicates the direction of maximum increase, therefore one can simply start to update $\mathbf{b}$ accoring to the steepest descent, i.e.

$$\Delta\mathbf{b}_0 = -\eta_0 \nabla_{\mathbf{b}} F(\mathbf{b}_0) \tag{4.101}$$

where η_0 is an adjustable step length, determined by a line search in this direction, until it reaches the minimum of F, i.e.

$$\eta_0 := \arg\min_{\eta} F(\mathbf{b}_0 + \eta\Delta\mathbf{b}_0) \tag{4.102}$$

This initial step $\Delta\mathbf{b}_0$ of length η_0 along the steepest descent makes up for the first iteration of the iterative method. The following steps constitute one interation, indicated as i, of moving along a subsequent conjugate direction $\mathbf{p}_i$:

1. Compute the steepest direction $\Delta\mathbf{b}_i = -\nabla_{\mathbf{b}} F(\mathbf{b}_i)$.
2. Compute the Fletcher-Reeves parameter $\beta_i = \Delta\mathbf{b}_i{}^T \Delta\mathbf{b}_n / \Delta\mathbf{b}_{i-1}{}^T \Delta\mathbf{b}_{i-1}$.
3. Update the conjugate direction $\mathbf{p}_i = \Delta\mathbf{b}_i + \beta_i \mathbf{p}_{i-1}$
4. Perform a line search to obtain $\eta_i = \arg\min_{\eta} F(\mathbf{b}_i + \eta\mathbf{p}_i)$
5. Update vector $\mathbf{b}$, in line with eq. 4.97, as $\mathbf{b}_{i+1} = \mathbf{b}_i + \eta_i \mathbf{p}_i$

The algorithm terminates when it locates the minimum, or when some tolerance criterion is reached. Concurrently, a pure quadratic function will reach the minimum quite faster than a non-quadtratic function.

The aforementioned conjugate gradient algorithm is employed in this thesis for the update of the design variables $\mathbf{b}$, in each optimization cycle, with F being the objective function of eq. 4.42. The big drawback of the method is that each line search subiteration, requires an additional functional evaluation of $F(\mathbf{b_i} + \eta_i \mathbf{p_i})$, thus a recomputation of the primal fields. As a result of this, for a total of N conjugate gradient iterations, the primal equations must also be solved for a total of N times. Nevertheless, utilizing this method is more efficient in terms of memory requirements.

4.4 Applications and Results

In this section, the adjoint-based shape optimization workflow is applied to the same production car for the reduction of the noise percieved by the driver, according to the surrogate objective function of eq. 4.42. As already mentioned, the big wind noise contributor is considered to be the vehicle's SVM, responsible of being a source of unsteady pressure fluctuations. From another point of view, in agreement with the objective function's approach, the side view mirror is responsible of being a source of highly turbulent flow, expressed in terms of high ν_t values. The high ν_t values, in turn, can relate to the creation of unsteady pressure fluctuations, based on the work of [4, 38]. Concurrently, the vehicle's windows, being subjected to a turbulent pressure excitation, are considered to be the main mechanism for transmiting sound waves from the exterior to the interior of the vehicle. In view of this, the aim is the reduction of the turbulent viscosity levels inside a volume that is residing next to the vehicle's side windows.

The particular production car comprises two side windows next to the driver, both considered as noise transmission mechanisms, shown in fig. 4.6.

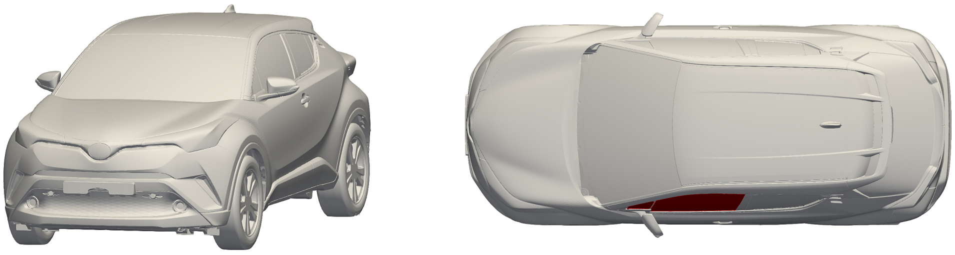

(a) *Vehicle's geometry* **(b)** *Vehicle's top view*

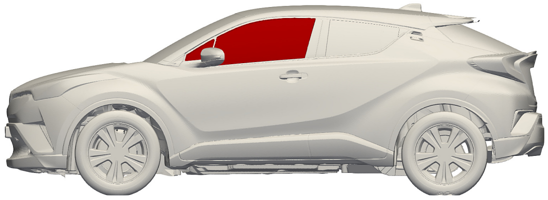

(c) *Vehicle's side view*

Figure 4.6: *The production car's geometry . The driver's side windows, considered as noise transsmiters to the interior of the car, are highlighted in red. The aim of the optimization is the minimisation of the objective function of eq. 4.42, within a thin volume residing on the highlited windows.*

To this end, the volumetric B-Splines of section 4.3.1 were used, in order to morph the shape of the driver's mirror and handle the mesh displacement during the optimization loops, without imposing any constraints.

CFD Mesh

In order to numerically solve the flow equations around the car's geometry, a computational domain is defined, where the primal and adjoint PDEs are integrated. The computational domain is in turn discretized to form a mesh consisting of cell elements. Owing to the limited computational resources and the apparent symmetry of the problem, a half-car model is used for the CFD simulations, instead of the full-car model. Although this approach is expected to introduce numerical errors in the vicinity of the symmetry plane, the benefit in terms of computational cost outweighs.

In this particular case, the computational domain around the half-car is a rectangular box, consisting of an inlet, an outlet, the sides and the top as well as the road (shown in fig. 4.7). The inlet lies $15m$ upstream from the vehicle, while the outlet lies $25m$ downstream, in order to secure uniform inlet and outlet flow conditions. Similarly, the height and width of the computational domain are approximately $11.6m$ and $11m$ respectively, such as the flow on the top and the sides is practically unaffected by the presence of the vehicle's geometry.

Figure 4.7: *Computational domain around the vehicle's half-car model geometry.*

The CFD mesh comprises $5 \cdot 10^6$ surface elements for representing the car's surface and $25 \cdot 10^6$ polyhedral volume elements for discretizing the fluid domain [7]. Furthermore, a hybrid approach has been used for the treatment of the viscous region close to the walls, in order for the boundary layer to be resolved. Specifically, the mesh features 7 layers of prismatic elements near the wall boundaries, where the wall functions combined with the Spalart-Allmaras model are integrated, with an average y^+ value of $y^+ \approx 25$. With the use of refinement boxes, the mesh has been refined in areas considered of high importance, i.e. where the flow is expected to contain more information; namely the area around the body of the vehicle, the rear part were a wake is expected to develop as well as the A-Pillar, SVM and side windows, which concern the present wind noise aerodynamic problem.

---

[7] The surface and volume mesh were provided by TME.

Nevertheless, in order to be able to run the optimization cycles at an affordable CPU cost, the surface mesh resolution remained relatively low in the geometries of interest; namely 13930 cells for the representation of the mirror (fig. 4.8) and 14017 cells for the side windows. All simulations were conducted with a stationary mesh on the wheels while, as shown on 4.8, the geometry of the vehicle's tires was intersected with the road by $10mm$, to account for tire deformation.

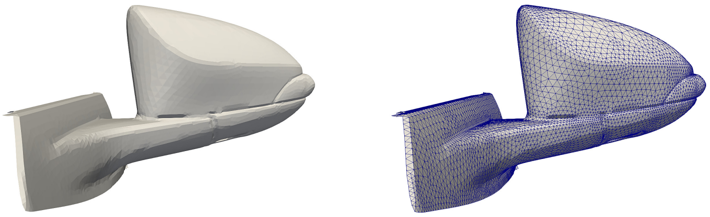

(a) *SVM's geometry* **(b)** *Mesh on SVM*

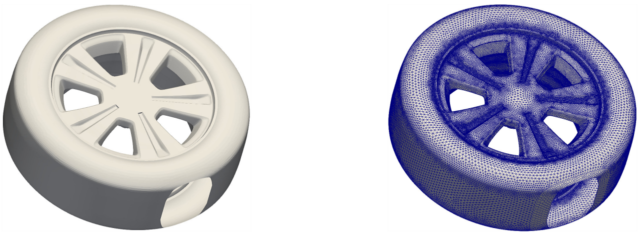

(c) *Wheel's geometry* **(d)** *Mesh on wheel*

Figure 4.8: *Mesh resolution on the side view mirror (SMV) and wheel surface. The surface mesh was generated with an average cell edge length of about* 1 *mm and consists of* 13930 *faces on the SVM and* 132263 *faces on the wheel.*

Concurrently, for the evaluation of the objective function of eq. 4.42, a thin volume $\Omega^{'}$ residing on the vehicle's side windows has been defined (shown in fig. 4.9). The volume $\Omega^{'}$ comprises only prismatic cells, while the wall functions technique is employed to determine the ν_t values along the volume's cell centers. It consists of a total of 71146 hexahedral elements, excluding the surface mesh elements of $S^{'}$.

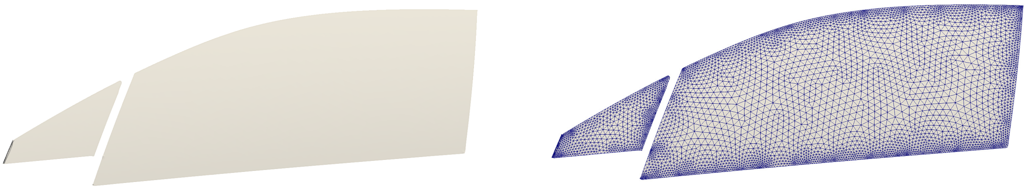

(a) *Windows surface* $S^{'}$ **(b)** *Volume* $\Omega^{'}$

Figure 4.9: *The volume* $\Omega^{'}$ *is residing on the windows surface* $S^{'}$ *with a thickness* t *of approximately* 1 *mm and consists of a total of* 71146 *hexagonal cell elements. The* ν_t^2 *field is integrated inside* $\Omega^{'}$ *in order to obtain the scalar objective funtion*

4.4.1 Flow Simulation

The primal and adjoint simulations were conducted on the aforementioned mesh, in the OpenFOAM© environment. The mean flow equations were solved by using the standard steady-state, pressure-based SIMPLE algorithm, by utilizing a second-order upwind scheme for the convection terms. Moreover, spatial gradients were discretized using the Green–Gauss theorem and a linear interpolation of the neighboring cell values on the mesh faces for the quantities of interest. The primal simulation reached convergence after 5000 iterations, with the use of relaxation factors.

The adjoint equations, in turn, were solved by using the adjoint OpenFOAM© solver developed by PCOpt/NTUA, by using a second order downwind scheme for the convection terms.

For the RANS flow simulation, a uniform inflow velocity of $v_\infty = 27.7 (m/s)$ was imposed on the inlet, equivalent to a cruising speed of 100 *kph*. Furthermore, a zero Dirichlet condition for the velocity was imposed on the car's surface, including the wheels which were modeled as stationary [8].

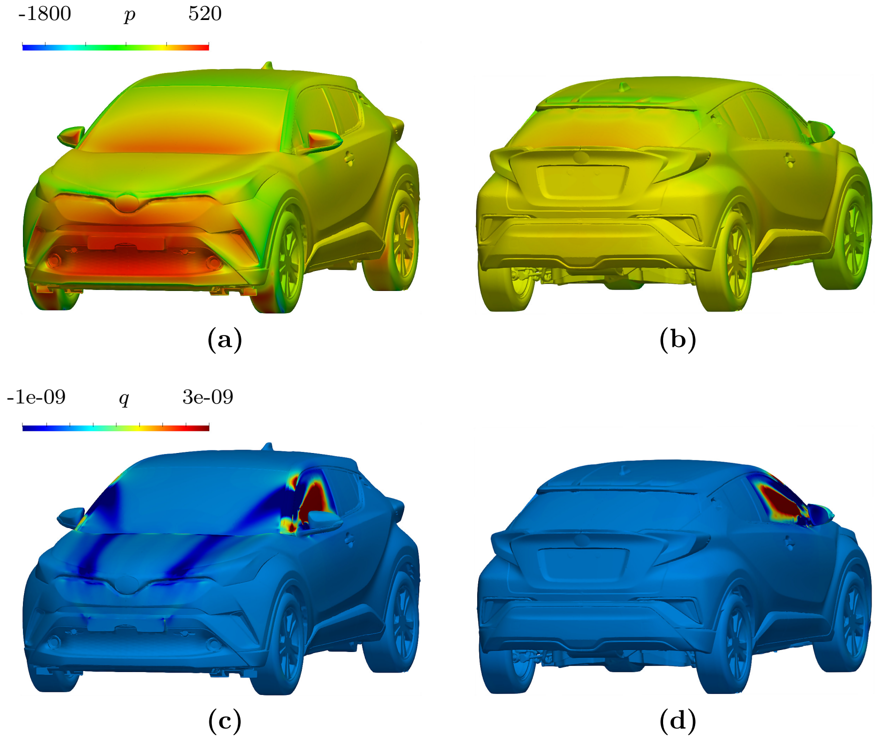

(a) **(b)**

(c) **(d)**

Figure 4.10: *Primal pressure p and adjoint pressure q distributions on the vehicle's surface. The adjoint pressure maximizes on the window and has a smaller magnitude.*

---

[8] Since spinning wheels induce noise on a wind tunnel experiment which cannot be modeled through the means of this work, both the simulation and the experiment were performed with stationary wheels for a better correlation between the two.

The pressure p and adjoint pressure q distributions on the car's surface are illustrated in fig. 4.10, obtained by fully converged solutions. The adjoint pressure locates its maximum on the side windows, while overall has a significantly smaller magnitude than pressure[9].

The primal and adjoint flow fields of pressure, velocity and turbulence model variable are illustrated in fig. 4.11, using a cross-sectional plane that is parallel to the road.

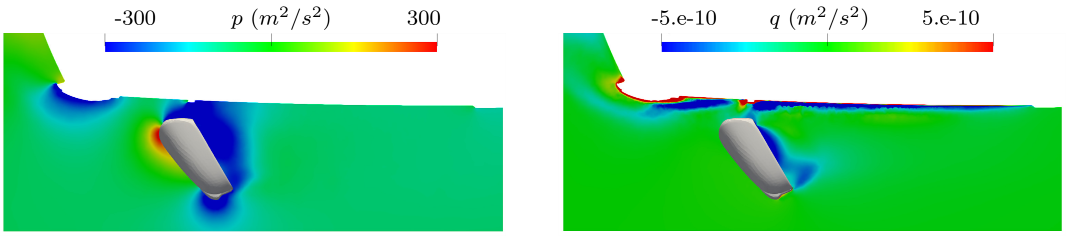

(a) *Pressure p* **(b)** *Adjoint pressure q*

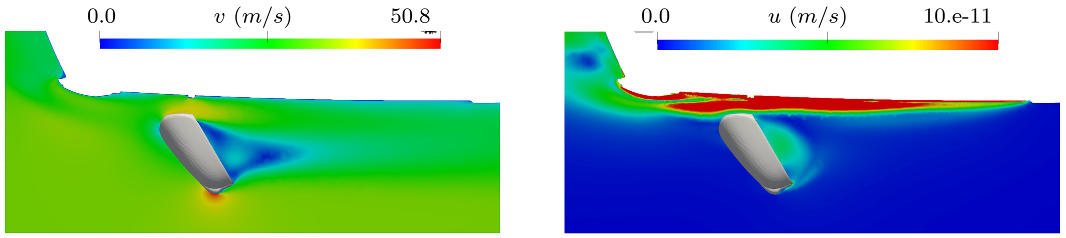

(c) *Velocity v* **(d)** *Adjoint velocity u*

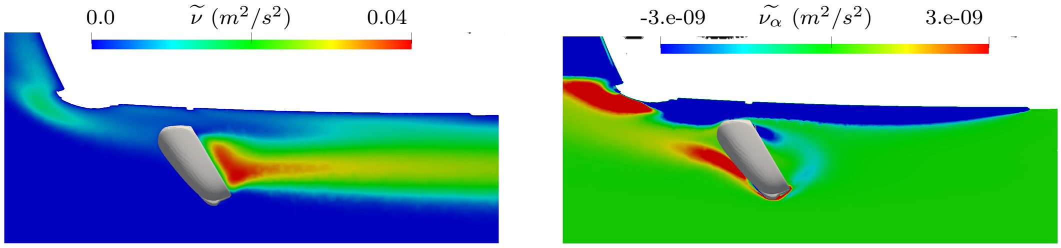

(e) *Spalart variable $\widetilde{\nu}$* **(f)** *Adjoint Spalart variable $\widetilde{\nu_\alpha}$*

Figure 4.11: *Primal and adjoint fields, plotted on a cross-sectional plane parallel to the road. The adjoint fields advance in a reverse-like manner compared to the primal ones and have a significantly smaller magnitude.*

The adjoint flow fields appear to develop in a reverse-like manner compared to the primal ones and have a significantly smaller magnitude.

---

[9] Pressure referes to kinematic pressure rather than static, given dimensionally in (m^2/s^2), since OpenFOAM© solves for p/ρ when the flow is incompressible.

After a fully-converged primal solution, the ν_t field is obtained. Fig. 4.12 illustrates with the use of isosurfaces the ν_t field downstream of the side view mirror. High levels of ν_t are observed along the mirror's wake, where the flow is turbulent. The ν_t^2 field is then calculated and integrated inside volume Ω' for a functional evaluation of the objective function.

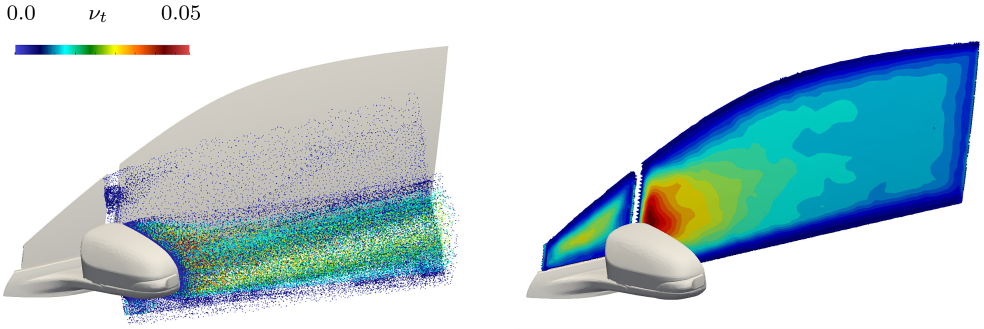

(a) *ν_t field's isosurfaces (m^2/s^2)* **(b)** *ν_t^2 field of volume Ω'*

Figure 4.12: *The ν_t field illustrated using iso-surfaces downstream of the SVM. The ν_t^2 field is in turn calculated and integrated inside Ω' to evaluate the objective function.*

Sensitivity Map on the SVM

After solving the field adjoint equations, the final sensitivity derivatives expression of eq. 4.90 can be evaluated. A map representation of the sensitivity derivatives field gives rise to the sensitivity map of fig. 4.13. The sensitivity map pinpoints the areas on the side view mirror's surface that show the greatest potential for noise reduction. Areas coloured in blue should be pushed inwards while red coloured areas should be pulled outwards.

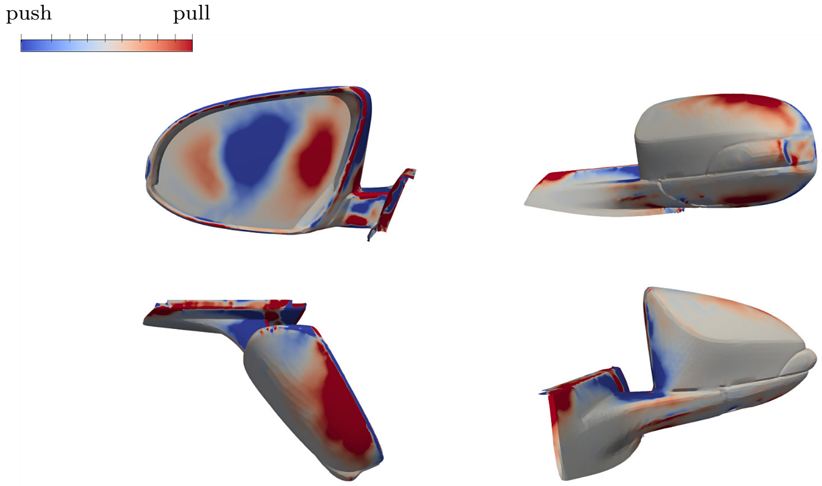

Figure 4.13: *Sensitivity map on the vehicle's side view mirror (SVM). Blue coloured areas should be pushed inwards, while red coloured areas outwards for noise reduction.*

4.4.2 Optimization Results

A volumetric B-Splines control grid consisting of $7 \times 7 \times 10$ control points, shown in fig. 4.14, was used in order to parametrize the driver's mirror geometry and morph it accordingly. The optimization was performed without imposing constraints, apart from allowing a maximum deflection of $2mm$ in each optimization cycle. It should be noted that in general, an unconstrained morphing might lead to impractical optimized shapes, such as a vanishing mirror.

In keeping with the available resources, the optimization algorithm was allowed to advance for 4 cycles, while the 5th cycle resulted to a deformed mesh failing the quality metrics, exhibiting negative cell volumes and high cell skewness. Upon the end of each cycle, the flow equations were solved anew and the objective function was evaluated for each deformed SVM geometry. The convergence of the objective function is presented in fig. 4.14. The wall clock time for computing a single cycle was 17.5 h, in 100 processes of Intel(R) Xeon(R) E5-2630 v4 @2.20 GHz CPUs.

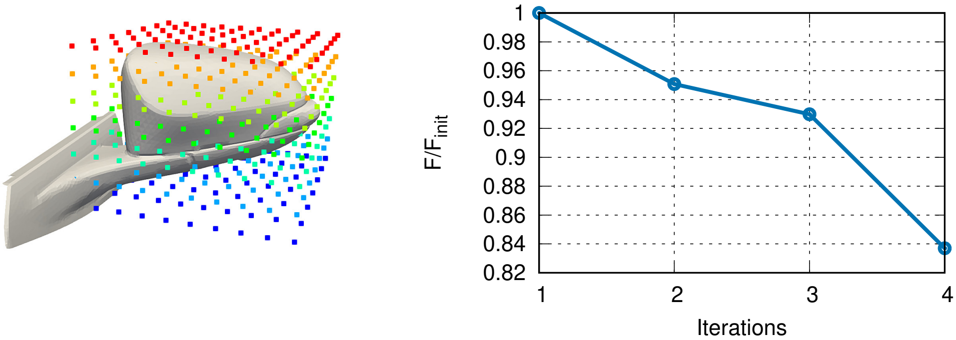

(a) *Control grid on SVM* **(b)** *Noise objective function convergence*

Figure 4.14: *Convergence history of the noise objective function F. All values have been devided by F_{init}, where F_{init} is the objective value computed by the baseline geometry. After a total of 3 optimization cycles, a 16% reduction on F is observed.*

As shown in fig. 4.14, the objective function F has reduced by a factor of 16% after 3 optimization cycles. This amount of reduction can be considered as relatively small, hence, one would normally progress for more than 4 iterations.

Nevertheless, as already mentioned, the optimization involved extreme mesh displacements and the simulation crashed after 4 iterations. In order for the algorithm to be able to proceed any further, a new mesh should be generated from scratch on the optimized geometry. On account of this, within the context of this thesis and the resources available, a reduction of 16% was considered acceptable, since a clear downwards trend on the objective function has been observed.

The optimized side view mirror geometries are shown in fig. 4.15 from an isometric view and in fig. 4.16 from a top-down view. The optimal mirror is thicker and appears as if it has rotated inwards around its rotational axis, in a position that is now facing the side window.

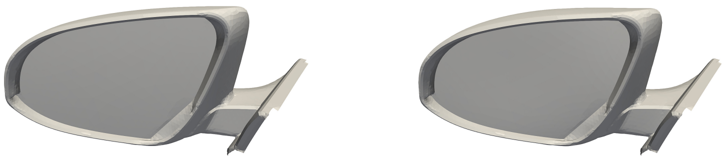

(a) *Baseline* **(b)** *1st optimization cycle*

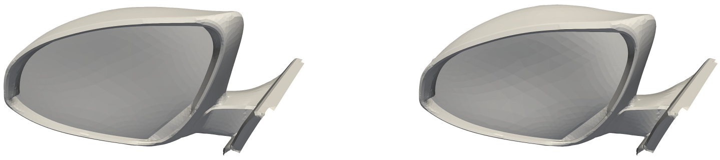

(c) *2nd optimization cycle* **(d)** *3rd optimization cycle*

Figure 4.15: *Baseline and three morphed side view mirror geometries.*

(a) *Baseline* **(b)** *1st cycle*

(c) *2nd cycle* **(d)** *3rd cycle*

Figure 4.16: *Top view of the baseline and of the three morphed side view mirror geometries. The inner edge on the upstream of the optimized mirror appears to be rounded off, possibly minimizing the local detachment of the flow.*

Moreover, the mirror's inner edge on the upstream has been notably rounded off. This modification results to a smoothly curved surface for the upcoming streamlines, possibly minimizing the detachment of the flow in the specific area.

The ν_t^2 field computed for the baseline and the three optimized mirror geometries is presented in fig. 4.17, plotted on a cutting plane of the volume $\Omega^{'}$. Each optimization cycle results to a decrease of the ν_t^2 field, while a significant decrease is observed on the 4th optimization cycle. The objective function value for each optimized geometry is decreased by 5%, 7% and 16% respectively, compared to the F value computed using the baseline.

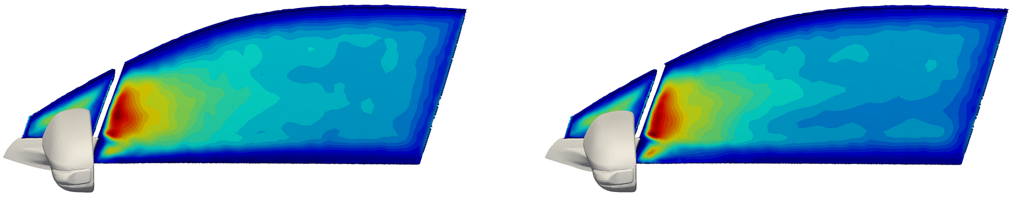

(a) *Baseline* **(b)** *1st optimization cycle*

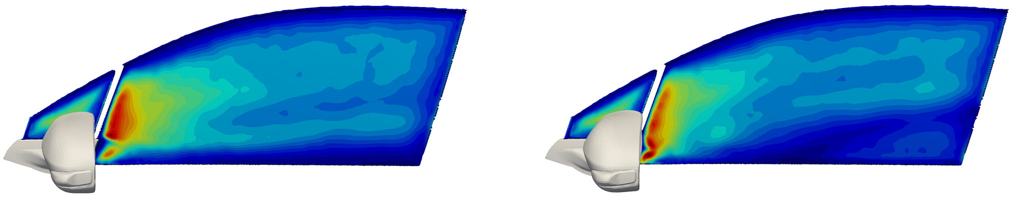

(c) *2nd optimization cycle* **(d)** *3rd optimization cycle*

Figure 4.17: *The ν_t^2 field computed using the baseline and three morphed SVM geometries, plotted on a plane inside the volume $\Omega^{'}$. The optimal SVM computes a ν_t^2 value, at an order of 16% smaller than the baseline geometry.*

The flow characteristics of each deformed geometry can be verified by examining the flow patterns downstream of the SVM. The computed flow fields are illustrated on a cross-sectional plane that extends along the mirror's wake and is parallel to the road. Fig. 4.18 illustrates the velocity magnitude and fig. 4.19 the turbulent viscocity, downstream of the baseline and three optimized mirrors.

The optimal mirror has rotated inwards and, as a result, it is directing its wake directly to the side glass. Furthermore, the recirculation downstream of the mirror has been reduced compared to the baseline, leading to a slight local increase of the velocity magnitude. Simultaneously, the local increase of velocity magnitude results to a decrease on ν_t values in the wake. Thus, it can be observed in fig. 4.19 that the ν_t values have been decreased not only close to the window, where $\Omega^{'}$ is located, but also along the whole length of the mirror's wake.

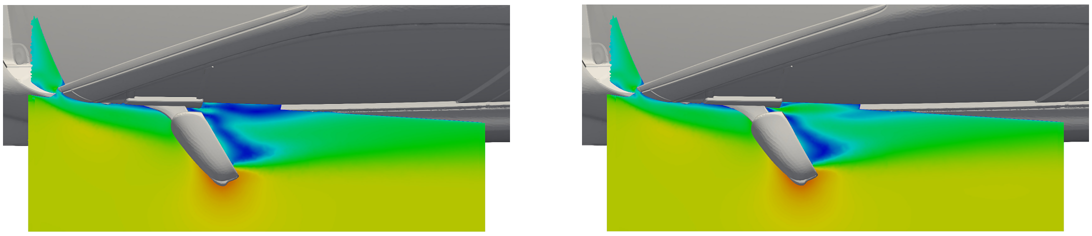

(a) *Baseline* **(b)** *1st optimization cycle*

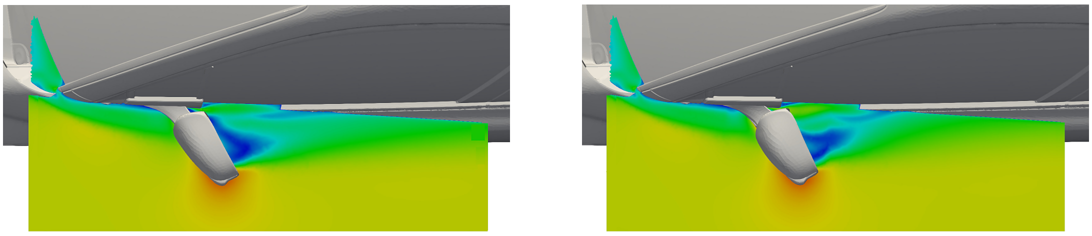

(c) *2nd optimization cycle* **(d)** *3rd optimization cycle*

Figure 4.18: *Velocity magnitude U field computed using the baseline and three morphed SVM geometries, plotted on a cross-sectional plane parallel to the road. The optimized geometry appears to be directing the mirror's wake towards the driver's side window.*

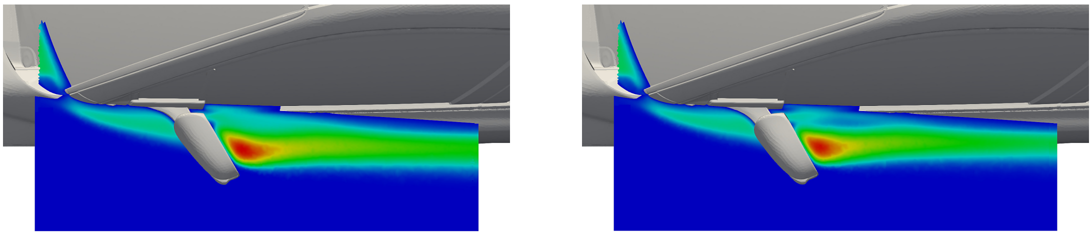

(a) *Baseline* **(b)** *1st optimization cycle*

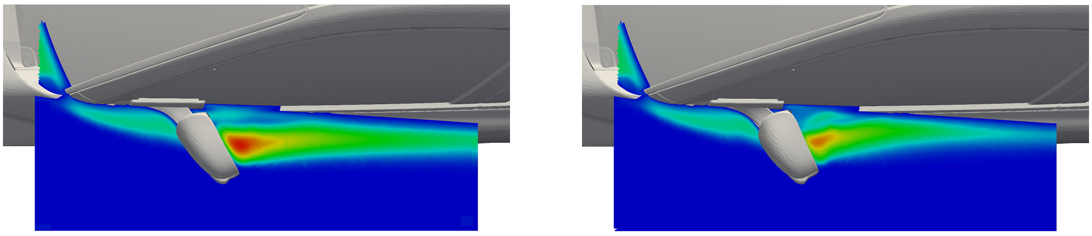

(c) *2nd optimization cycle* **(d)** *3rd optimization cycle*

Figure 4.19: *The ν_t field computed using the baseline and three morphed SVM geometries, plotted on a cross-sectional plane parallel to the road. A reduction on ν_t can be observed not only close to the volume $\Omega^{'}$, but also along the length of the mirror's wake.*

4.4.3 Correlation with Experiment

An attempt has been made for a fast but reliable experimental validation of the aforementioned optimization results. In consideration of this, a mock-up model of the optimized mirror geometry was evaluated in the anechoic wind tunnel. The mock-up model was based on a shape modification of the existing side view mirror, so as to resemble the optimal mirror's geometry.

In order to determine the differences in noise levels between the baseline and the mock-up mirror cases, two sets of experimental measurements were conducted; firstly, a phased array beamforming technique was applied for the localization of the exterior noise sources; secondly, interior noise levels have been measured for both cases, using microphones positioned in the cabin, close to the driver's ear.

The acoustic measurements were performed in the S2A GIE acoustic windtunnel, outside of Paris, France [44]. The experimental setup for the noise source localization that supports the beamforming acoustic testing consists of 88 microphones on the top/horizontal array, arranged in a spiral configuration. The frequency range of the output acoustic intensity map is 630-8000 Hz and the source separation capability is 17 cm at 2 kHz.

The production car as well as the mock-up model of the mirror that was used, seen from a front view, are shown in fig. 4.20.

(a) *Production car in windtunnel* **(b)** *Front view of mock-up model*

Figure 4.20: *A view of the production car in the GIE windtunnel and a front view of the optimized SVM's mock-up model.*

Fig. 4.4.3 presents the noise intensity maps of the baseline case and the mock-up mirror case, obtained by the phased array beamforming technique at the 2 kHz frequency band. First and foremost, it is observed that the main source of exterior wind noise is the vehicle's side view mirrors. Moreover, it is observed in the mock-up model case that the noise intensity has been notably reduced around the driver's SVM, i.e. around the mock-up mirror model.

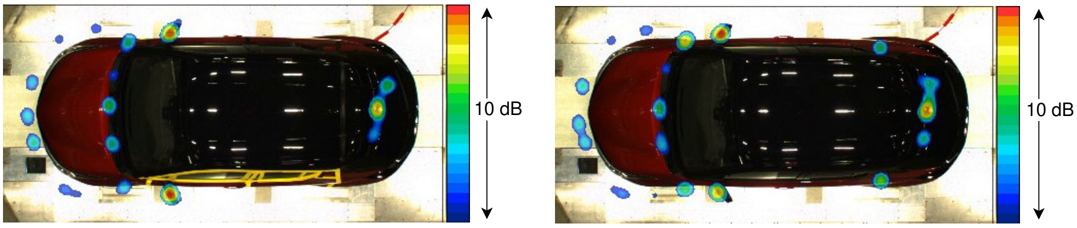

(a) *Baseline SVM* **(b)** *Mock-up SVM*

Figure 4.21: *Noise intensity maps of the baseline case and the mock-up mirror case, produced by the phased array beamforming technique at the 2 kHz frequency band. The driver's side view mirror on the right image has been replaced by the mock-up model. Red coloured areas refer to high levels of exterior noise, measured in dB.*

Specifically, regarding all frequency ranges, a total decrease of $0.7dB$ on exterior noise is achieved with the introduction of the mock-up mirror model. This amount of exterior noise reduction can be considered significant (hence, not accidental) and can therefore validate the suggested shape modification.

Furthermore, a reduction has also been observed on the interior noise levels, measured using microphones positioned inside the cabin. Fig. 4.4.3 presents the interior noise levels measured for the baseline and the mock-up SVM test cases. It is noted that the absolute dB values of interior noise have been normalized.

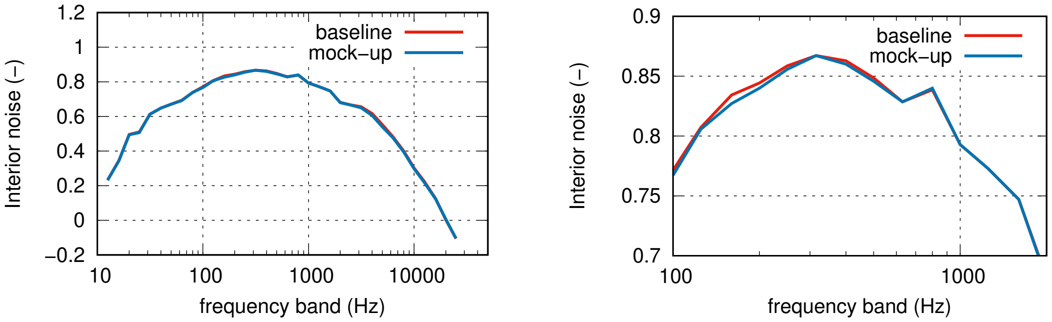

Figure 4.22: *Normalized interior noise levels of baseline and mock-up SVM.*

By averaging over all frequency bands, a mean reduction of $0.14dB$ is achieved on interior noise. This amount of reduction corresponds to a 0.67% articulation index (AI) improvement [10].

---

[10] Articulation index (AI) referres to the amount of speech that is audible to a passenger of the vehicle.

Chapter 5

Summary & Conclusions

In this diploma thesis, a prediction of exterior wind noise induced from car geometries was realised through means of a CFD-based model in the OpenFOAM© environment. Furthermore, a shape optimization based on the continuous adjoint method was performed, in order to reduce wind noise levels. The adjoint method used, developed by PCOpt/NTUA, is formulated based on the Enhanced SI (E-SI) approach. The Spalart-Allmaras turbulence model was fully differentiated in order to take into account the effect of the design variable value changes in the flow turbulence.

In order to predict the aeroacoustic characteristics of vehicles and localize the noise sources, a CFD-based Noise Source Identification (NSI) model, developed and owned by Toyota Motor Corporation (TMC), has been programmed in the OpenFOAM© environment. A key performance indicator, referred to as Acoustic Pressure Density Source ($APDS$), is the output of the model, which determines the fluid regions that contribute to the generation of acoustic pressure fluctuations. The model requires the unsteady flow fields of velocity and vorticity around the vehicle, acquired by a transient CFD simulation. A transfer of the unsteady flow fields of velocity from the time domain to the frequency domain has been performed via a Fast Fourier Transform (FFT). The code used, performs an FFT on unsteady scalar field data and was programmed for the purposes of this thesis in OpenFOAM© v.1906. The NSI method was applied to a production car; the unsteady flow fields were obtained by a DDES simulation, combined with the Spalart-Allmaras turbulence model. The warm-up period of the simulation was detected and truncated using the heuristic MSER-5 algorithm, implemented in C++.

Thereinafter, a shape optimization workflow using the continuous adjoint method was utilized, so as to reduce the wind noise levels percieved by the driver of the vehicle. In order to bypass an expensive unsteady optimization workflow, a surrogate model expressing the generation of wind noise in an incompressible and steady-state manner was used as the objective functional of the optimization process, expressed exclusively in terms of turbulent viscosity. The main wind noise generating component, the vehicle's side view mirror, was parametrized using volumetric B-Splines and morphed accordingly for a minimization of the objective function.

Concluding this thesis, the implementation of TMC's vortex sound based NSI model has successfully determined the flow patterns that contribute to aerodynamic noise (i.e. the A-pillar's wake and side view mirror's wake). The $APDS$ results imply that the main wind noise generating component of the vehicle is the side view mirror (SVM). Furthermore, the $APDS$ index field suggests that the inner edge of the side view mirror should be deformed in order to reduce wind noise. This result comes in agreement with the sensitivity maps produced by the adjoint method, since they both pinpoint the inner edge of the SVM for noise reduction.
Regarding the adjoint optimization, a reduction of 16% has been observed on the objective function after a total of 4 optimization cycles. Moreover, the optimized mirror shape reduces the turbulent viscosity levels both close to the window and along the entire mirror's wake. A fast validation of these results in the anechoic wind tunnel, using a mock-up model of the optimized mirror shape, results to a total decrease of $0.7dB$ on exterior noise, leading to a 0.67% articulation index (AI) improvement.

Proposals for Future Work

1. Validation of the current implementation of the vortex sound NSI model, through experimental means or through comparison with its previous implementation of the method by TMC.
2. A unsteady DDES simulation around the car geometry for a longer physical time, in order to determine the broader unsteadiness and better understand how the unsteady flow fields of interest develop over time.
3. Implementation of the MSER-5 algorithm in OpenFOAM$^{©}$, so as to apply it for entire flow fields instead of specific points in the flow, in order to more accurately detect the warm-up period of an unsteady CFD simulation.
4. Application of the $APDS$ model on the optimized SVM geometry obtained in this thesis, in order to validate that the optimized mirror reduces the levels of the $APDS$ index field.
5. Developement of the continuous adjoint method to the $APDS$ model, as a tool to compute the sensitivity derivatives of the $APDS$ index w.r.t. the vehicle's shape. These sensitivity derivatives can be used in an unsteady optimization workflow, in order to minimize the $APDS$ levels and optimize production cars for low noise emissions.

Εθνικό Μετσόβιο Πολυτεχνείο
Σχολή Μηχανολόγων Μηχανικών
Τομέας Ρευστών
Μονάδα Παράλληλης Υπολογιστικής Ρευστοδυναμικής
& Βελτιστοποίησης

Πρόλεξη του Αεροδυναμικά Επαγόμενου Εξωτερικού Θορύβου από Αυτοκίνητα & Βελτιστοποίηση Μορφής με Χρήση της Συνεχούς Συζυγούς Μεθόδου

Εκτενής Περίληψη Διπλωματικής Εργασίας

Κωνσταντίνος Σάρρας

Επιβλέπων
Κυριάκος Χ. Γιαννάκογλου, Καθηγητής ΕΜΠ

Αθήνα, 2020

Εισαγωγή

Τα τελευταία χρόνια, η αεροακουστική ανάλυση επιβατηγών αυτοκινήτων λαμβάνει σημαντική θέση στον χώρο της αυτοκινητοβιομηχανίας, καθώς ο θόρυβος επηρεάζει έντονα τα επίπεδα συγκέντρωσης, την ασφάλεια αλλά και την άνεση του οδηγού. Σε χαμήλες ταχύτητες, ο θόρυβος στο εσωτερικό της καμπίνας οφείλεται κυρίως σε παράγοντες όπως τον κινητήρα, τα λάστιχα ή το σύστημα μετάδοσης κίνησης. Ωστόσο, σε υψηλές ταχύτητες (άνω των 100 χμ/ώρα), ο αεροδυναμικά επαγόμενος θόρυβος, δηλαδή ο θόρυβος εξαιτίας της αεροδυναμικής μορφής του αμαξιού, κυριαρχεί στο εσωτερικό. Δεδομένου αυτού, η μείωση του αεροδυναμικού θορύβου αποτελεί καθοριστικό παράγοντα στην ανάπτυξη ποιοτικών και ανταγωνιστικών αυτοκινήτων.

Πρωταρχικός στόχος της διπλωματικής εργασίας είναι ο προγραμματισμός και η εφαρμογή μιας αξιόπιστης μεθόδου, που στοχεύει στον εντοπισμό των πηγών αεροδυναμικού θορύβου σε επιβατηγά οχήματα. Η μέθοδος προϋποθέτει τον εκ των προτέρων υπολογισμό των χρονικά μη-μόνιμων πεδίων ροής γύρω από το σώμα του αμαξιού. Δευτερευόντως, τίθεται ως στόχος η μείωση των επιπέδων θορύβου στο εσωτερικό του οχήματος. Κυρίαρχος παράγοντας παραγωγής θορύβου θεωρούνται τα υψηλά επίπεδα τύρβης που αναπτύσσονται κατάντι του καθρέπτη του οδηγού, εκφραζόμενα από υψηλές τιμές της τυρβώδους συνεκτικότητας. Ενόψει αυτού, συνάρτηση κοστός προς ελαχιστοποίηση είναι τα επίπεδα της τυρβώδους συνεκτικότητας με χρήση κατάλληλου χωρικού ολοκληρώματος τους στην περιοχή ενδιαφέροντός τους. Η ελαχιστοποίηση της συνάρτησης κόστους επιτυγχάνεται μέσω βελτιστοποίησης μορφής του καθρέπτη, με χρήση της συνεχούς συζυγούς μεθόδου.

Μοντελοποίηση της ροής

Πρώτο στάδιο της παρούσας δουλείας αποτελεί η ανάλυση της τυρβώδους συνεκτικής ροής γύρω απο τη γεωμετρία του αυτοκινήτου προς μελέτη. Για την μοντελοποίηση της ροής αυτής, ακολουθήθηκαν δύο προσεγγίσεις· Η πρώτη, απλούστερη προσέγγιση είναι αυτή των RANS εξισώσεων. Το RANS μοντέλο (**2.1.1**) επιλύει πρακτικά την μόνιμη συνεκτική ροή, ενώ το μοντέλο τύρβης Spalart-Allmaras [**29**] (**4.1.2**) μοντελοποιεί τον τυρβώδη χαρακτήρα της. Η δεύτερη προσέγγιση αφορά την επίλυση μη-μόνιμης ροής με χρήση του υβριδικού μοντέλου DDES (**2.1.4**), βασιζόμενη στο μοντέλο τύρβης Spalart-Allmaras. Η υβριδοποίηση έγκειται στην επίλυση των RANS εξισώσεων κοντά στον τοίχο και των LES (**2.1.2**) μακρυά, πετυχαίνοντας έτσι γρήγορη και υψηλής ακρίβειας επίλυση του μη-μόνιμου πεδίου.

Και στις δύο προσεγγίσεις επίλυσης ροής, χρησιμοποιείται η τεχνική των συναρτήσεων τοίχου προκειμένου να προσδιοριστούν τα χαρακτηριστικά του οριακού στρώματος κοντά στα τοιχώματα του αυτοκίντου, δεδομένης της χρήσης αραιών (κατάλληλων για μοντέλα τύρβης υψηλών αριθμών Reynolds) πλεγμάτων.

Μοντέλο Πρόλεξης Αεροδυναμικού Θορύβου

Για την επίλυση προβλημάτων αεροδυναμικού θορύβου που σχετίζονται με εφαρμογές αυτοκινήτων, είναι σημαντικό πολλές φορές να προσδιοριστούν οι θέσεις των κύριων πηγών θορύβου γύρω από το όχημα. Ενόψει αυτού, αναπτύχθηκε από την Toyota Motor Corporation (TMC) μοντέλο υπολογιστικής ρευστομηχανικής με σκοπό την αεροακουστική αξιολόγηση ενός οχήματος, καθώς και τον εντοπισμό των πηγών αεροδυναμικού θορύβου γύρω από το όχημα. Συγκεκριμένα, το μοντέλο που κατοχυρώνει ο V.L. Phan μέσω πατέντας No. US 2019/0354647 , χρησιμοποιεί την ακουστική αναλογία του Powell [20] προκειμένου να προσδιορίσει τις πηγές της ακουστικής πίεσης που βιώνουν τα παράθυρα του οχήματος, δεχόμενοι ότι οι διαταραχές αυτές προκαλούν δονήσεις στο τζάμι του παραθύρου και διαδίδουν τον θόρυβο στο εσωτερικό.

Ορίζεται όγκος ρευστού Ω που περικλύει τα εξαρτήματα του αυτοκινήτου που ευθύνονται για τον αεροδυναμικό θόρυβο (πλευρικός καθρέπτης, κολόνα A-Pillar). Παράλληλα, ορίζεται S η επιφάνεια των παραθύρων του οχήματος. Κάθε σημείο του Ω υποδηλώνεται ως $\boldsymbol{z}$ και κάθε σημείο της επιφάνειας S ως $\boldsymbol{x}$.

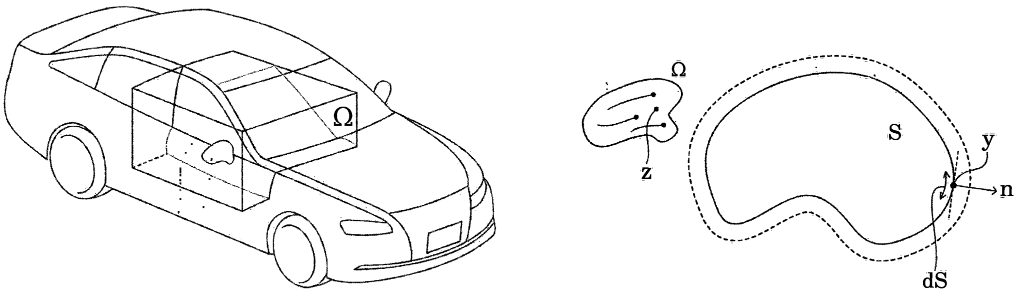

(α′) *Όγκος ρευστού* Ω (β′) *Όγκος* Ω *και επιφάνεια* S

Σχήμα 5.1: *Όγκος ρευστού* Ω *στον οποίο ικανοποιούνται οι εξισώσεις του μοντέλου. Ο όγκος περικλύει τα κύρια εξαρτήματα του αυτοκινήτου που ευθύνονται για τον αεροδυναμικό θόρυβο. Σημεία του όγκου συμβολίζονται με* $\boldsymbol{z}$ *ενώ σημεία της επιφάνειας του αμαξιού με* $\boldsymbol{y}$.

Με χρήση της εξίσωσης 3.20, ο V.L. Phan καταλήγει σε μια σχέση μεταξύ των ακουστικών διαταραχών πίεσης και ροϊκών μεγεθών του ρευστού, εκφραζόμενη στο πεδίο της συχνότητας, που δίνεται από τον δείκτη κατανομής πηγών ακουστικής πίεσης (Acoustic Pressure Density Source (APDS))

$$APDS(\boldsymbol{y},\boldsymbol{z},f_m) \propto \frac{{f_m}^2}{|\boldsymbol{r}|^4} \cdot |\boldsymbol{u_f}| \cdot |\overline{\boldsymbol{u}} \times \boldsymbol{r}| \cdot |\overline{\boldsymbol{\omega}} \times \boldsymbol{r}| \tag{5.1}$$

όπου $|\boldsymbol{u_f}|$ το μέτρο της ταχύτητας στο πεδίο της συχνότητας, $\overline{\boldsymbol{u}}$ η χρονικά μέση ταχύτητα, $\overline{\boldsymbol{\omega}}$ η χρονικά μέση στροβιλότητα, f_m η ζώνη συχνοτήτων που μας αφορά και

$\boldsymbol{r} = \boldsymbol{y} - \boldsymbol{z}$ η απόσταση μεταξύ των σημείων υπολογισμού.

Ολοκλήρωση της εξ. 5.1 πάνω στην επιφάνεια των παραθύρων S δίνει ·ενα χωρικό πεδίο $APDS(\boldsymbol{z}, f_m)$ για κάθε ζώνη συχνοτήτων f_m, ή

$$APDS(\boldsymbol{z}, f_m) = \int_S APDS(\boldsymbol{y}, \boldsymbol{z}, f_m) dS \tag{5.2}$$

Μεγάλες τιμές του $APDS(\boldsymbol{z}, f_m)$ χωρικού πεδίο της εξ. 5.2 εντοπίζονται στα σημεία της ροής που συμβάλλουν στην ακουστική πίεση που βιώνει το τζάμι του παραθύρου. Συνεπώς, το πεδίο $APDS(\boldsymbol{z}, f_m)$ εκφράζει την ένταση των πηγών θορύβου μέσα στην ροή.
Αντίστοιχα , ολοκληρώνοντας την εξ. 5.1 εντός του όγκου Ω δίνει το επιφανειακό πεδίο $APDS(\boldsymbol{y}, f_m)$ πάνω στην επιφάνεια S των παραθύρων, ένα για κάθε ζώνη συχνοτήτων f_m

$$APDS(\boldsymbol{y}, f_m) = \int_\Omega APDS(\boldsymbol{y}, \boldsymbol{z}) d\Omega \tag{5.3}$$

Υψηλές τιμές του πεδίου της εξ. 5.3 εντοπίζονται στα σημεία του τζαμιού του παραθύρου που βιώνουν διαταραχές πίεσης συχνότητας f_m με μεγάλο πλάτος (ή ενέργεια).

Η ροή εργασίας για τον υπολογισμό των $APDS$ πεδίων δίνεται συνοπτικά από τα επόμενα 6 βήματα:

1. Εκτέλεση ΥΡΔ προσομοίωσης μη-μόνιμης ροής για έναν φυσικό χρόνο T δευτερολέπτων, ούτως ώστε να αποκτηθούν τα μη-μόνιμα πεδία ταχύτητας $\widetilde{\boldsymbol{u}}$ και στροβιλότητας $\widetilde{\boldsymbol{\omega}}$. Περικοπή των αρχικών T^* δευτερολέπτων που αντιστοιχούν στην μεταβατική περίοδο της προσομοίωσης.
2. Αποθήκευση των μη-μόνιμων πεδίων ταχύτητας $\widetilde{\boldsymbol{u}}$ εντός του όγκου Ω, για παράθυρο φυσικού χρόνου T_w χρησιμοποιώντας ένα καθορισμένο απο τον χρήστη χρονικό βήμα δειγματοληψίας Δt.
3. Εφαρμογή μετασχηματισμού Fast Fourier Transfrom (FFT) στα πεδία της μη-μόνιμης ταχύτητα $\widetilde{\boldsymbol{u}}$ ώστε να υπολογισθούν τα πεδία ταχύτητας στο πεδίο συχνότητας $\boldsymbol{u_f}$. Μείωση της ανάλυσης του πεδίου συχνότητας από ευρυζωνική σε 1^{ec} ή $1/3^o$ οκτάβες.
4. Εύρεση των χρονικά μέσων πεδίων ταχύτητας $\overline{\boldsymbol{u}}$ και στροβιλότητας $\overline{\boldsymbol{\omega}}$, με υπολογισμό του μέσου όρου των τιμών των πεδίων για χρονικό παράθυρο T_w.
5. Υπολογισμός του δείκτη $APDS(\boldsymbol{y}, \boldsymbol{z}, f_m)$ με χρήση της εξ. 5.1.
6. Ολοκλήρωση του $APDS(\boldsymbol{y}, \boldsymbol{z}, f_m)$ πεδίου πάνω στην επιφάνεια των παραθύρων του οχήματος S, προκειμένου να υπολογιστεί το χωρικό $APDS(\boldsymbol{z}, f_m)$ πεδίο για κάθε ζώνη συχνοτήτων f_m, με βάση την εξ. 5.2.
7. Ολοκλήρωση του $APDS(\boldsymbol{y}, \boldsymbol{z}, f_m)$ πεδίου εντώς του όγκου Ω, προκειμένου να υπολογιστεί το επιφανειακό $APDS(\boldsymbol{y}, f_m)$ πεδίο πάνω στα παράθυρα, για κάθε ζώνη συχνοτήτων f_m, με βάση την εξ. 5.3.

Εφαρμογή σε Αυτοκίνητο Παραγωγής

Η προαναφερθείσα ροή εργασίας για την αεροακουστική αξιολόγηση και τον εντοπισμό των πηγών αεροδυναμικού θορύβου ενός οχήματος, εφαρμόστηκε σε επιβατηγό αυτοκίνητο μαζικής παραγωγής. Η γεωμετρία του αυτοκινήτου δίνεται στο σχήμα **5.2**. Στην εικόνα απεικονίζεται επίσης ο όγκος ρευστού Ω, ο οποίος περικλείει τον καθρέπτη, το A-Pillar και τα παράθυρα του οδηγού.

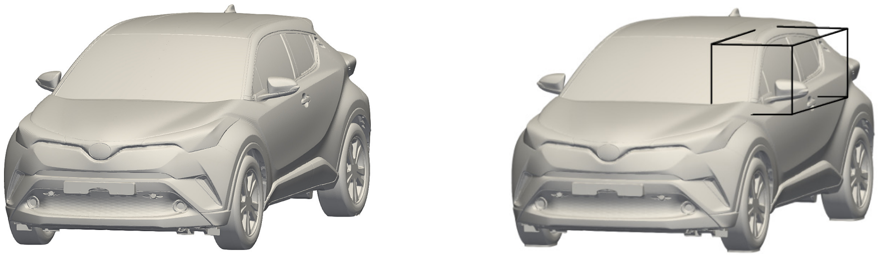

(α΄) *Γεωμετρία αυτοκινήτου*

(β΄) *Όγκος ρευστού* Ω

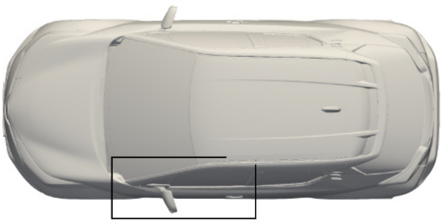

(γ΄) *Άνω όψη του όγκου* Ω

Σχήμα 5.2: *Γεωμετρία του αυτοκινήτου παραγωγής. Ορίζεται όγκος ρευστού* Ω *που περικλύει τον καθρέπτη, το A-Pillar και τα παράθυρα του οδηγού. Σημειώνεται ότι ο όγκος* Ω *αποτελείται εξ΄ ολοκλήρου από σημεία ρευστού και, συνεπώς, αποκλείει οποιαδήποτε επιφάνεια που βρίσκεται εντός των ορίων του.*

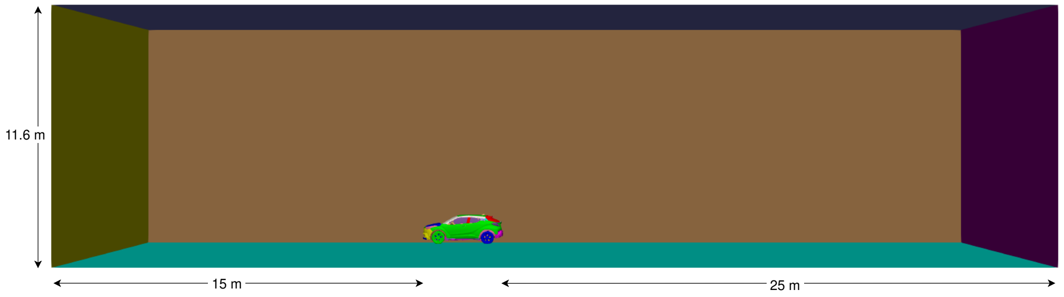

Σχήμα 5.3: *Παραλληλεπίπεδο υπολογιστικό χωρίο γύρω από την γεωμετρία του αυτοκινήτου. Οι επιφάνειες εισόδου και εξόδου της ροής τοποθετούνται* $15m$ *και* $11m$ *μακριά από το αυτοκίνητο, αντίστοιχα, προκειμένου να υπάρχει ομοιόμορφη ροή στην είσοδο και την έξοδο.*

Το υπολογιστικό χωρίο του σχήματος 5.3 διακριτοποιήθηκε σε υπολογιστικό πλέγμα αποτελούμενο από πολυγωνικά κελιά. Το πλέγμα αποτελείται από $2.8 \cdot 10^6$ επιφανειακά κελιά για την αναπαράσταση της γεωμετρίας του αμαξιού και $4 \cdot 10^7$ πολυεδρικά ογκικά κελιά για την αναπαράσταση του χωρίου του ρευστου.

Οι εξισώσεις μη-μόνιμης ροής του μοντέλου DDES επιλύθηκαν στο προαναφερθέν υπολογιστικό πλέγμα. Στο σχήμα 5.4 δίνονται τα πεδία του μέτρου της ταχύτητας στο πεδίο συχνότητας $|\boldsymbol{u_f}|$, υπολογισμένα για τέσσερις μπάντες συχνοτήτων.

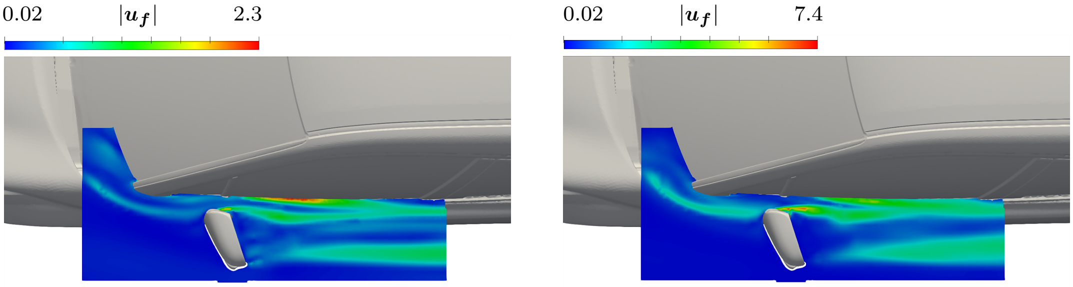

(α′) $f_m = 25\ Hz$ (β′) $f_m = 125\ Hz$

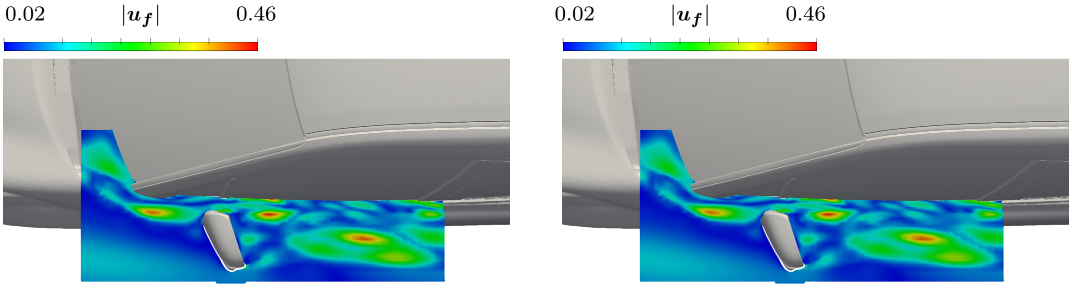

(γ′) $f_m = 1000\ Hz$ (δ′) $f_m = 2000\ Hz$

Σχήμα 5.4: *Πεδία του μέτρου της ταχύτητας στο πεδίο συχνότητας $|\boldsymbol{u_f}|$, προκύπτοντα από μετασχηματισμό FFT των μη-μόνιμων πεδίων ταχύτητας $\tilde{u}$, απεικονιζόμενα σε επίπεδο παράλληλο στον δρόμο.*

(α′) *Χρονικά μέσο πεδίο ταχύτητας $\overline{v}$* (β′) *Χρονικά μέσο πεδίο στροβιλότητας $\overline{\omega}$*

Σχήμα 5.5: *Χρονικά μέσα πεδία ταχύτητας $\overline{u}$ και στροβιλότητας $\overline{\omega}$.*

Αποτελέσματα χωρικού και επιφανειακού APDS πεδίου

Το σχήμα 5.6 παρουσιάζει τις ισο-επιφάνειες του χωρικού πεδίου $APDS(z)$, για την 1/3 οκτάβα συχνοτήτων κεντρικής συχνότητας $f_m = 2kHz$. Γίνεται φανερό ότι τα μοτίβα της ροής που συμβάλλουν στην δημιουργία ακουστικής πίεσης είναι αφ' ενός ο ομόρρους του A-Pillar , ενώ κυρίως δε είναι ο ομόρρους κατάντι του καθρέφτη του οδηγού.

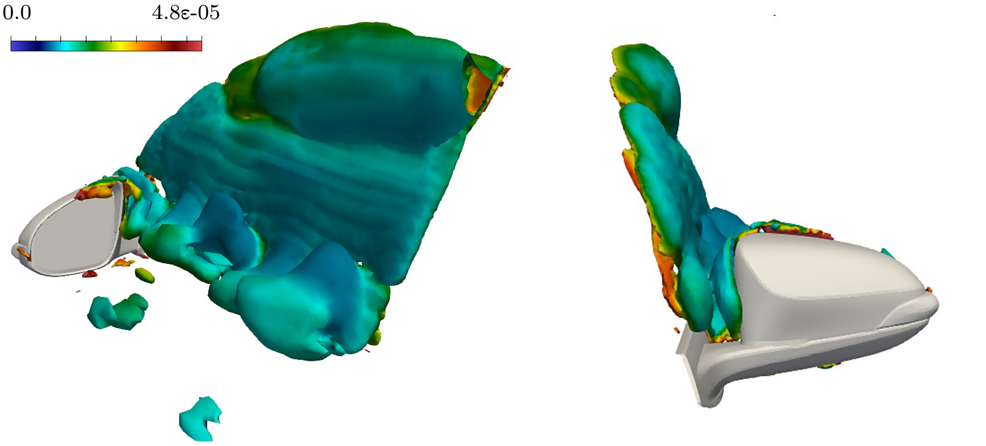

Σχήμα 5.6: *Το χωρικό πεδίο πηγών θορύβου $APDS(z)$ του όγκου Ω, υπολογισμένο για την 1/3 οκτάβα συχνοτήτων κεντρικής συχνότητας $f_m = 2kHz$.*

Στο σχήμα 5.7 παρουσιάζεται το επιφανειακό πεδίο $APDS(y)$ πάνω στο τζάμι των παραθύρων της θέσης του οδηγού. Υψηλες τιμές του πεδίου εντοπίζονται εκεί όπου οι διαταραχές πίεσης συχνότητας f_m εμφανίζουν μεγάλο πλάτος.

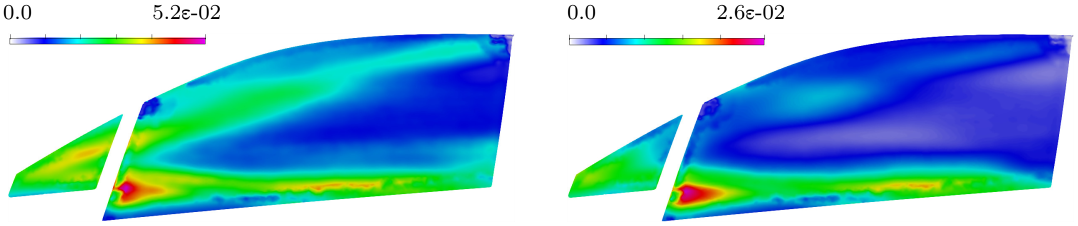

(α΄) $f_m = 25\ Hz$ (β΄) $f_m = 40\ Hz$

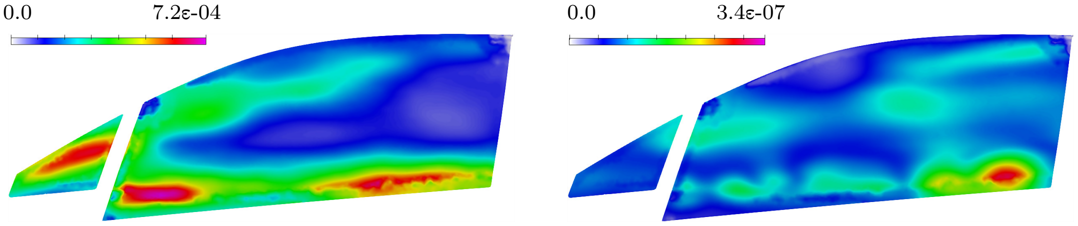

(γ΄) $f_m = 125\ Hz$ (δ΄) $f_m = 2000\ Hz$

Σχήμα 5.7: *Πεδίο επιφανειακών διαταραχών πίεσης $APDS(y)$ πάνω στο τζάμι των παραθύρων της θέσης του οδηγού, για διαφορετικές ζώνες συχνοτήτων.*

Διατύπωση του Συζυγούς Προβλήματος

Αφετηρία για τη διαμόρφωση του συζυγούς προβλήματος είναι η μαθηματική διατύπωση του πρωτεύοντος προβλήματος, το οποίο περιγράφεται από τις RANS εξισώσεις για ασυμπίεστη και χρονικά μόνιμη ροή συνδυασμένες με το μοντέλο τύρβης Spalart-Allmaras, [29]. Οι εξισώσεις αυτές, χρησιμοποιώντας τη σύμβαση του Einstein για τους επαναλαμβανόμενους δείκτες, γράφονται ως εξής

$$R^p = -\frac{\partial v_j}{\partial x_j} = 0 \tag{5.4α$'$}$$

$$R_i^v = v_j \frac{\partial v_i}{\partial x_j} - \frac{\partial}{\partial x_j}\left[(\nu+\nu_t)\left(\frac{\partial v_i}{\partial x_j}+\frac{\partial v_j}{\partial x_i}\right)\right] + \frac{\partial p}{\partial x_i} = 0\,, \qquad i=1,2,3 \tag{5.4β$'$}$$

$$R^{\widetilde{\nu}} = v_j \frac{\partial \widetilde{\nu}}{\partial x_j} - \frac{\partial}{\partial x_j}\left[\left(\nu+\frac{\widetilde{\nu}}{\sigma}\right)\frac{\partial \widetilde{\nu}}{\partial x_j}\right] - \frac{c_{b2}}{\sigma}\left(\frac{\partial \widetilde{\nu}}{\partial x_j}\right)^2 - \widetilde{\nu}\, P\left(\widetilde{\nu}\right) + \widetilde{\nu}\, D\left(\widetilde{\nu}\right) = 0 \tag{5.4γ$'$}$$

Εν συνεχεία, ορίζεται η συνάρτηση κόστους F προς ελαχιστοποίηση. Βασιζόμενοι σε βιομηχανική εμπειρία, μια συνάρτηση κόστους που σχετίζεται με την παραγωγή αεροδυναμικού θορύβου, εξαρτάται αποκλειστικά από την τυρβώδη συνεκτικότητα ν_t και δίνεται από τη σχέση [4]

$$F_\nu = \int_{\Omega'} \nu_t^2 d\Omega \tag{5.5}$$

όπου ν_t είναι η τυρβώδης συνεκτικότητα και Ω' είναι όγκος που γειτνιάζει στο παράθυρο του οδηγού του αυτοκινήτου με προκαθορισμένο πάχος.

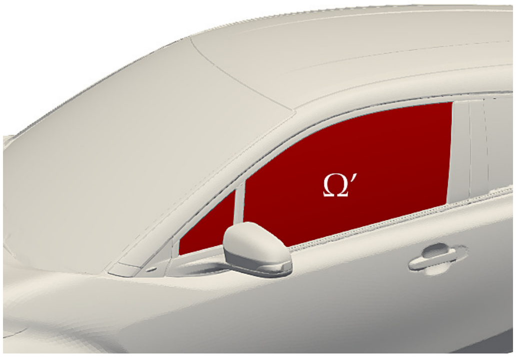

Σχήμα 5.8: *Πεπερασμένος όγκος Ω' για τον ορισμό της συνάρτησης κόστους 5.5. Ο όγκος Ω' γειτνιάζει στο παράθυρο του οδηγού του αυτοκινήτου και έχει προκαθορισμένο πάχος.*

Βασική αρχή της συνεχούς συζυγής μεθόδου είναι ο ορισμός της Λαγκραντζιανής ή επαυξημένης συνάρτησης κόστους L. Η επαυξημένη συνάρτηση ορίζεται προκειμένου να εξασφαλιστεί η ανεξαρτησία του κόστους υπολογισμού των παραγώγων ευαισθησίας από το πλήθος N των μεταβλητών σχεδιασμού. Στην E-SI συζυγή προσέγγιση που χρησιμοποιείται εδώ, η επαυξημένη συνάρτηση κόστους ορίζεται ως

$$L = F_\nu + \int_\Omega u_i R_i^v d\Omega + \int_\Omega q R^p d\Omega + \int_\Omega \widetilde{\nu_a} R^{\widetilde{\nu}} d\Omega + \int_\Omega m_i^a R_i^m d\Omega \tag{5.6}$$

όπου Ω είναι το υπολογιστικό χωρίο, u_i η συζυγής ταχύτητα, q η συζυγής πίεση και $\widetilde{\nu_a}$ η συζυγής μεταβλητή του μοντέλου τύρβης και m_i^a η συζυγής της μεταβλητής m_i, δηλαδή των μετατοπίσεων των κόμβων του πλέγματος.

Διαφόριση της εξίσωσης **5.6** ως προς τις μεταβλητές σχεδιασμού b_n δίνει

$$\begin{aligned}\frac{\delta L}{\delta b_n} =& \frac{\delta F_\nu}{\delta b_n} + \int_\Omega u_i \frac{\partial R_i^v}{\partial b_n} d\Omega + \int_\Omega q \frac{\partial R^p}{\partial b_n} d\Omega + \int_\Omega \widetilde{\nu_a} \frac{\partial R^{\widetilde{\nu}}}{\partial b_n} d\Omega \\ &+ \int_{S_{W_P}} m_i^a n_j \frac{\partial}{\partial x_j} \left(\frac{\delta x_i}{\delta b_n} \right) dS - \int_{S_{W_P}} \frac{\partial m_i^a}{\partial x_j} n_j \frac{\delta x_i}{\delta b_n} dS + \int_\Omega \frac{\partial^2 m_i^a}{\partial x_j^2} \frac{\delta x_i}{\delta b_n} \delta\Omega \\ &+ \int_{S_{W_P}} \left(u_i R_i^v + q R^p + \widetilde{\nu_a} R^{\widetilde{\nu}} + m_i^a R_i^m \right) n_k \frac{\delta x_k}{\delta b_n} dS \end{aligned} \tag{5.7}$$

όπου για τον όρο της παραγώγου της συνάρτησης κόστους $\delta F_\nu / \delta b_n$ ισχύει

$$\begin{aligned}\frac{\delta F_\nu}{\delta b_n} &= \frac{\delta}{\delta b_n} \int_{\Omega'} \nu_t^2 d\Omega = \int_{\Omega'} \frac{\partial \nu_t^2}{\partial b_n} d\Omega + \int_{S'} \nu_t^2 n_k \frac{\delta x_k}{\delta b_n} dS \\ &= \int_{\Omega'} \underbrace{2\nu_t \frac{\partial \nu_t}{\partial \widetilde{\nu}}}_{\acute{F}_\Omega^{\widetilde{\nu}}} \frac{\partial \widetilde{\nu}}{\partial b_n} d\Omega + \int_{S'} \nu_t^2 n_k \frac{\delta x_k}{\delta b_n} dS \end{aligned} \tag{5.8}$$

όπου $S^{'}$ η επιφάνεια των παραθύρων του αυτοκινήτου και $\acute{F}_\Omega^{\widetilde{\nu}}$ ένας επιπλέον όρος πηγής που πρέπει να ικανοποιεί η εξίσωση του συζυγούς μοντέλου τύρβης στο $\Omega^{'}$. Σημειώνεται ότι αφού $L = F_\nu$, τότε $\delta L / \delta b_n = \delta F_\nu \ \delta b_n$.

Λαμβάνοντας υπόψη την εξ. **5.8** και, εν συνεχεία, θέτοντας τους πολλαπλασιαστές των παραγώγων των ροϊκών ποσοτήτων ως προς τις μεταβλητές σχεδιασμού εντός των χωρικών ολοκληρωμάτων ίσους με το μηδέν, προκύπτουν οι συζυγείς πεδιακές εξισώσεις

$$R^q = -\frac{\partial u_j}{\partial x_j} + \acute{F}_\Omega^p = 0 \tag{5.9}$$

$$\begin{aligned} R_i^u =& u_j \frac{\partial v_j}{\partial x_i} - \frac{\partial (v_j u_i)}{\partial x_j} - \frac{\partial}{\partial x_j} \left[(\nu + \nu_t) \left(\frac{\partial u_i}{\partial x_j} + \frac{\partial u_j}{\partial x_i} \right) \right] + \frac{\partial q}{\partial x_i} + \acute{F}_{\Omega,i}^v \\ &+ \widetilde{\nu_a} \frac{\partial \widetilde{\nu}}{\partial x_i} - \frac{\partial}{\partial x_l} \left(\widetilde{\nu_a} \widetilde{\nu} \frac{\mathcal{C}_Y}{Y} e_{mjk} \frac{\partial v_k}{\partial x_j} e_{mli} \right) = 0 \ , \ i = 1, 2, 3 \end{aligned} \tag{5.10}$$

$$
\begin{aligned}
R^{\widetilde{\nu_a}} = & -\frac{\partial(v_j\widetilde{\nu_a})}{\partial x_j} - \frac{\partial}{\partial x_j}\left[\left(\nu+\frac{\widetilde{\nu}}{\sigma}\right)\frac{\partial\widetilde{\nu_a}}{\partial x_j}\right] + \frac{1}{\sigma}\frac{\partial\widetilde{\nu_a}}{\partial x_j}\frac{\partial\widetilde{\nu}}{\partial x_j} + 2\frac{c_{b2}}{\sigma}\frac{\partial}{\partial x_j}\left(\widetilde{\nu_a}\frac{\partial\widetilde{\nu}}{\partial x_j}\right) \\
& + \widetilde{\nu_a}\widetilde{\nu}\mathcal{C}_{\widetilde{\nu}} + \frac{\partial\nu_t}{\partial\widetilde{\nu}}\frac{\partial u_i}{\partial x_j}\left(\frac{\partial v_i}{\partial x_j}+\frac{\partial v_j}{\partial x_i}\right) + (-P+D)\,\widetilde{\nu_a} + \acute{F}_{\Omega}^{\widetilde{\nu}} = 0
\end{aligned} \tag{5.11}
$$

$$
R_k^{m^a} = \frac{\partial^2 m_k^a}{\partial x_j^2} + \frac{\partial}{\partial x_j}\left\{u_i v_j\frac{\partial v_i}{\partial x_k} + u_j\frac{\partial p}{\partial x_k} + \tau_{ij}^a\frac{\partial u_i}{\partial x_k} - u_i\frac{\partial\tau_{ij}}{\partial x_k} - q\frac{\partial v_j}{\partial x_k}\right\} = 0 \tag{5.12}
$$

Οι οριακές συνθήκες των συζυγών εξισώσεων δίνονται αναλυτικά στο αγγλικό κείμενο (**4.2.5**), ενώ εδώ παραλείπονται για λόγους συντομίας. Μετά την εξαγωγή των συζυγών εξισώσεων και των συζυγών οριακών συνθηκών, η τελική έκφραση των παραγώγων ευαισθησίας δίνει

$$
\begin{aligned}
\frac{\delta F_{aug}}{\delta b_n} = & T_{SD}^{WF} - \int_{S_{W_p}} \mathcal{SD}_1\frac{\partial\tau_{ij}}{\partial x_m}n_j t_i^I n_m n_k\frac{\delta x_k}{\delta b_n}dS - \int_{S_{W_p}}\mathcal{SD}_1\tau_{ij}\frac{\delta(n_j t_i^I)}{\delta b_n}\frac{\delta x_k}{\delta b_n}dS \\
& + \int_{S_{W_p}}\mathcal{SD}_{2,i}v_{\langle t\rangle}^I\frac{\delta t_i^I}{\delta b_n}dS - \int_{S_{W_p}}\mathcal{SD}_{2,i}\frac{\partial v_i}{\partial x_m}n_m n_k\frac{\delta x_k}{\delta b_n}dS \\
& - \int_{S_{W_p}}\left[\left(\nu+\frac{\widetilde{\nu}}{\sigma}\right)\frac{\partial\widetilde{\nu_a}}{\partial x_j}n_j + \frac{\partial F_{S_z}}{\partial\widetilde{\nu}}n_z + \acute{F}_S^{\widetilde{\nu}}\right]\frac{\partial\widetilde{\nu}}{\partial x_m}n_m n_k\frac{\delta x_k}{\delta b_n}dS \\
& - \int_{S_{W_p}}(-u_{\langle n\rangle} + \phi_{\langle n\rangle\langle n\rangle})\left(\tau_{ij}\frac{\delta(n_i n_j)}{\delta b_n} + \frac{\partial\tau_{ij}}{\partial x_m}n_m\frac{\delta x_k}{\delta b_n}n_k n_i n_j\right)dS \\
& - \int_{S_{W_p}}\phi_{\langle t^I\rangle\langle t^I\rangle}\left(\tau_{ij}\frac{\delta(t_i^I t_j^I)}{\delta b_n} + \frac{\partial\tau_{ij}}{\partial x_m}n_m\frac{\delta x_k}{\delta b_n}n_k t_i^I t_j^I\right)dS \\
& - \int_{S_{W_p}}(\phi_{\langle t^{II}\rangle\langle t^I\rangle} + \phi_{\langle t^I\rangle\langle t^{II}\rangle})\left(\tau_{ij}\frac{\delta(t_i^{II} t_j^I)}{\delta b_n} + \frac{\partial\tau_{ij}}{\partial x_m}n_m\frac{\delta x_k}{\delta b_n}n_k t_i^{II} t_j^I\right)dS \\
& - \int_{S_{W_p}}\phi_{\langle t^{II}\rangle\langle t^{II}\rangle}\left(\tau_{ij}\frac{\delta(t_i^{II} t_j^{II})}{\delta b_n} + \frac{\partial\tau_{ij}}{\partial x_m}n_m\frac{\delta x_k}{\delta b_n}n_k t_i^{II} t_j^{II}\right)dS \\
& + \int_{S_{W_p}}n_i\frac{\partial F_{S_{W_p,i}}}{\partial x_m}n_m\frac{\delta x_k}{\delta b_n}n_k dS + \int_{S_{W_p}}F_{S_{W_p,i}}\frac{\delta n_i}{\delta b_n}dS + \int_{S_{W_p}}F_{S_{W_p,i}}n_i\frac{\delta(dS)}{\delta b_n} \\
& - \int_{S_{W_P}}\frac{\partial m_i^a}{\partial x_j}n_j\frac{\delta x_i}{\delta b_n}dS + \int_{S_{W_p}}\mathcal{A}_{\Delta}^{WF}\frac{\partial\Delta^P}{\partial b_n}dS + \int_{S_W}\mathcal{A}_{\Delta}^{WF}\frac{\partial\Delta^P}{\partial b_n}dS \\
& + \int_{S_{W_p}}\Delta_a R^{\Delta}n_k\frac{\delta x_k}{\delta b_n}dS - \int_{S_{W_p}}2\Delta_a\frac{\partial\Delta}{\partial x_j}n_j\frac{\partial\Delta}{\partial x_m}n_m n_k\frac{\delta x_k}{\delta b_n}dS
\end{aligned} \tag{5.13}
$$

όπου

$$
\mathcal{SD}_1 = -u_{\langle t\rangle}^I + \phi_{\langle t^I\rangle\langle n\rangle} + \phi_{\langle n\rangle\langle t^I\rangle} \tag{5.14}
$$

$$
\mathcal{SD}_{2,i} = (\nu+\nu_t)\left(\frac{\partial u_i}{\partial x_j}+\frac{\partial u_j}{\partial x_i}\right)n_j - qn_i + \frac{\partial F_{S_{W_p,k}}}{\partial v_i}n_k + \acute{F}_{S_{W_p,i}}^v \tag{5.15}
$$

$$
\phi_{ij} = \frac{\partial F_{S_{W_p,k}}}{\partial\tau_{ij}}n_k \tag{5.16}
$$

όπου οι όροι T^{WF}_{SD}, $\int_{S_{W_P}} \mathcal{A}^{WF}_{\Delta} \frac{\partial \Delta^P}{\partial b_n} dS$ ανδ $\int_{S_W} \mathcal{A}^{WF}_{\Delta} \frac{\partial \Delta^P}{\partial b_n} dS$ συνοψίζουν τη συνεισφορά της διαφόρισης των συναρτήσεων τοίχου στις παραγώγους ευαισθησίας [40].

Μέσω της εξ. **5.13** των παραγώγων ευαισθησίας, μπορεί να προσδιορισθεί η κλίση της συνάρτησης κόστους ως προς την κάθετη μετατόπιση των επιφανειακών κόμβων του πλέγματος. Γραφική απεικόνιση των παραπάνω παραγώγων επάνω στην επιφάνεια του οχήματος συνθέτει τον χάρτη ευαισθησίας του προβλήματος

Βελτιστοποίηση Μορφής Πλευρικού καθρέπτη

Κατόπιν του υπολογισμού των συζυγών πεδίων ροής και των παραγώγων ευαισθησίας, ακολούθησε η αφ΄ ενός παραμετροποίηση και αφ΄ ετέρου βελτιστοποίηση της μορφής του καθρέπτη του οδηγού, με σκοπό την ελαχιστοποίηση της συνάρτησης κόστους. Η μορφοποίηση του σχήματος του καθρέπτη, και ταυτόχρονα του πλέγματος, πραγματοποιήθηκε με χρήση ογκικών B-Splines . Συγκεκριμένα, ορίζεται κουτί ελέγχου του σχήματος **5.9**, που απαρτίζεται από 7 × 7 × 10 σημεία ελέγχου και περικλύει την γεωμετρία του καθρέπτη.

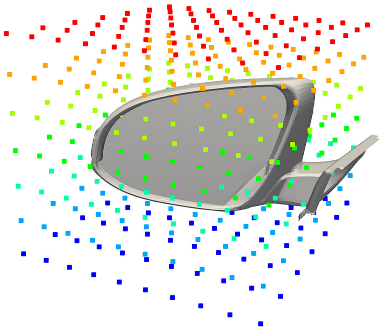

Σχήμα 5.9: *Κουτί ελέγχου ογκικών B-Splines , αποτελούμενο από* $7 \times 7 \times 10$ *σημεία ελέγχου που παραμετροποιεί την γεωμετρία του καθρέπτη του αμαξιού.*

Οποιαδήποτε μετακίνηση των σημείων ελέγχου οδηγεί σε ανάλογη παραμόρφωση των επιφανειακών και ογκικών κελιών του υπολογιστικού πλέγματος.

Οι συντεταγμένες των σημείων ελέγχου των ογκικών B-Splines αποτελούν τις μεταβλητές σχεδιασμού b_n της βελτιστοποίησης. Αναναίωση των μεταβλητών σχεδιασμού από κύκλο σε κύκλο βελτιστοποίησης οδηγεί σε καινούργιες γεωμετρίες καθρέπτη που ολοένα ελαχιστοποιούν την τιμή της συνάρτησης κόστους F_ν. Η μέθοδος ανανέωσης των μεταβλητών σχεδιασμού b_n βασίζεται στην πληροφορία της παραγώγου ευαισθησίας $\delta F_\nu / \delta b_n$ ούτως ώστε να προσδιορίζεται η κατεύθυνση κίνησης των συνιστωσών των b_n η οποία θα επιφέρει μείωση της συνάρτησης κόστους. Συγκεκριμένα, η μέθοδος των συζυγών κλίσεων εφαρμόζεται για την αναναίωση του b_n, η οποία δίνεται αναλυτικά στο αγγλικό κείμενο (**4.3.2**), αλλά παραλείπεται εδώ χάριν συντομίας.

Εφαρμογή σε Αυτοκίνητο Παραγωγής

Η προαναφερθείσα διαδικασία βελτιστοποίησης εφαρμόζεται στο επιβατηγό αυτοκίνητο μαζικής παραγωγής που αφορά την παρούσα εργασία, με στόχο τη μείωση των επιπέδων θορύβου που αντιλαμβάνεται ο οδηγός του αμαξιού. Η γεωμετρία του αυτοκινήτου παραγωγής δίνεται στο σχήμα **5.10**. Τα παράθυρα στην θέση του οδηγού S' πάνω στα οποία ορίζεται ο όγκος Ω' επισημαίνονται με κόκκινο χρώμα.

Προκειμένου να λυθούν υπολογιστικά οι πρωτεύουσες και συζυγείς εξισώσεις ροής γύρω από την γεωμερία του αυτοκινήτου, ορίστηκε παραλληληλεπίπεδο υπολογιστικό χωρίο, που δίνεται στην εικόνα **4.7** του αγγλικού κειμένου. Δεδομένης της προφανούς συμμετρίας του προβλήματος και των περιορισμένων υπολογιστικών πόρων, χρησιμοποιήθηκε το μοντέλο του μισού αμαξιού. Οι επιφάνειες εισόδου και εξόδου της ροής τοποθετούνται $15m$ και $11m$ μακριά από το αυτοκίνητο, αντίστοιχα, προκειμένου να υπάρχει ομοιόμορφη ροή στην είσοδο και την έξοδο του χωρίου υπολογισμού.

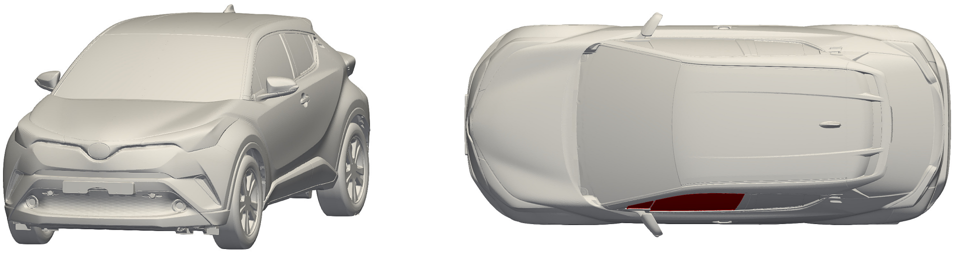

(α΄) *Γεωμετρία αυτοκινήτου* (β΄) *Άνω όψη αυτοκινήτου*

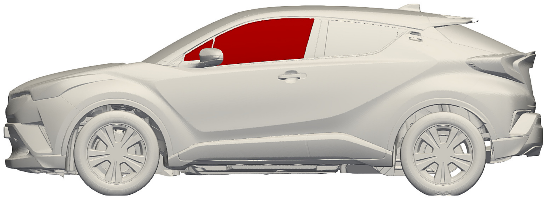

(γ΄) *Πλάγια όψη αυτοκινήτου*

Σχήμα 5.10: *Γεωμετρία του επιβατηγού αυτοκινήτου παραγωγής. Τα παράθυρα στην θέση του οδηγού S' πάνω στα οποία ορίζεται ο όγκος Ω' επισημαίνονται με κόκκινο χρώμα.*

Το υπολογιστικό χωρίο διακριτοποιήθηκε σε υπολογιστικό πλέγμα αποτελούμενο από πολυγωνικά κελιά. Το πλέγμα αποτελείται από $5 \cdot 10^6$ επιφανειακά κελιά για την αναπαράσταση της γεωμετρίας του μοντέλου του μισού αυτοκινήτου και από $25 \cdot 10^6$ πολυεδρικά ογκικά κελία για την αναπαράσταση του χωριού του ρευστου. Παράλληλα, το πλέγμα διαθέτει 7 στρώματα από πρισματικά κελία κοντά στα στερεά τοιχώματα του αυτοκινήτου, με το πρώτο κελί να βρίσκεται σε αδιάστατη απόσταση y^+ κατά μέσο όρο $y^+ \approx 25$.

Οι πρωτεύουσες και οι συζυγείς εξισώσεις ροής επιλύθηκαν στο προαναφερθέν υπολογιστικό πλέγμα. Στην είσοδο του χωρίου επιβλήθηκε ταχύτητα ομοιόμορφης ροής εισόδου $v_\infty = 27.7(m/s)$ που αντιστοιχεί ισοδύναμα σε ταχύτητα πλέυσης των 100 (χμ/ώρα). Παράλληλα, οι ρόδες του οχήματος μοντελοποιήθηκαν ως ακίνητες.

Τα πρωτεύοντα και συζυγή πεδία ροής της πίεσης, ταχύτητας και της μεταβλητής του μοντέλου τύρβης παρουσιάζονται στο σχήμα 5.11, απεικονισμένα σε επίπεδο τομής που είναι παράλληλο στον δρόμο. Τα συζυγή πεδία δείχνουν να αναπτύσσονται κατά αντίστροφο τρόπο σε σχέση με τα πρωτεύοντα πεδία ροής, ενώ εμφανίζουν σημαντικά χαμηλότερο μέτρο.
Παράλληλα, οι κατανομές της πίεσης p και της συζυγούς πίεσης q επάνω στην επιφάνεια του αυτοκινήτου δίνονται στο σχήμα 5.12. Η συζυγής πίεση μεγιστοποιείται στην επιφάνεια των παραθύρων του αμαξιού, ενώ συνολικά παρουσιάζει σημαντικά χαμηλότερες τιμές.

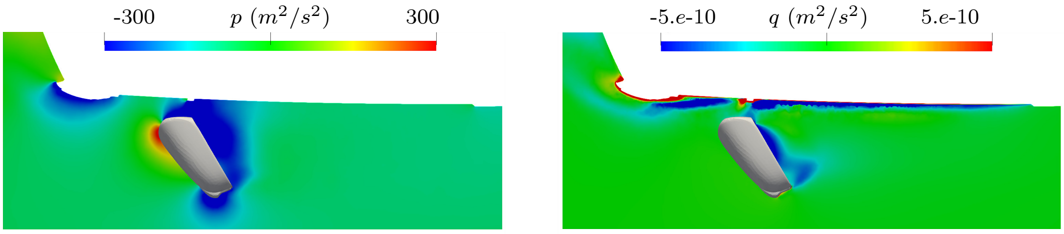

(α') *Πίεση* p **(β')** *Συζυγής πίεση* q

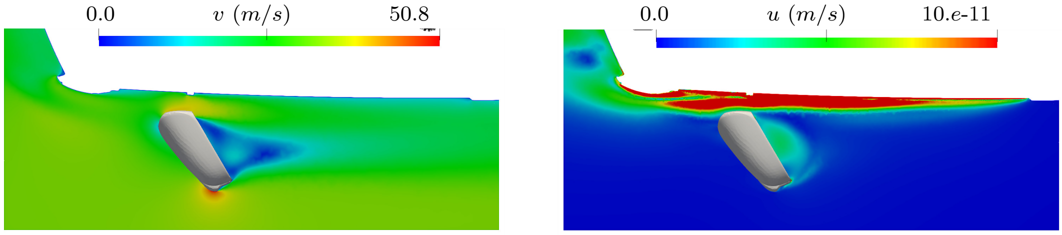

(γ') *Ταχύτητα* v **(δ')** *Συζυγής ταχύτητα* u

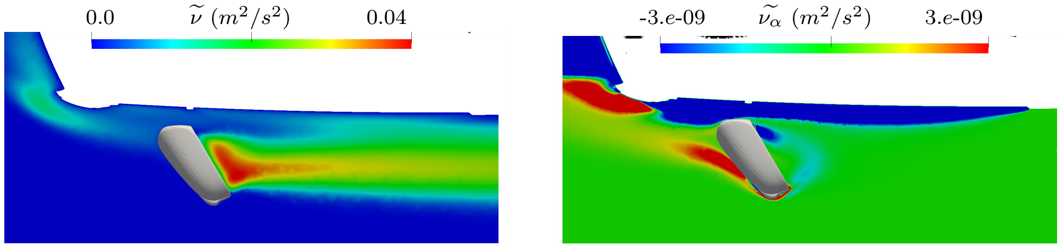

(ε') *Spalart μεταβλητή* $\widetilde{\nu}$ **(ϛ')** *Συζηγής Spalart μεταβλητή* $\widetilde{\nu_\alpha}$

Σχήμα 5.11: *Πρωτεύοντα και συζηγή πεδία ροής απεικονιζόμενα ανάντι και κατάντι του καθρέπτη με χρήση επιπέδου παράλληλου στον δρόμο. Τα συζυγή πεδία αναπτύσσονται κατά αντίστροφο τρόπο σε σχέση με τα πρωτεύοντα και εμφανίζουν σημαντικά χαμηλότερο μέτρο.*

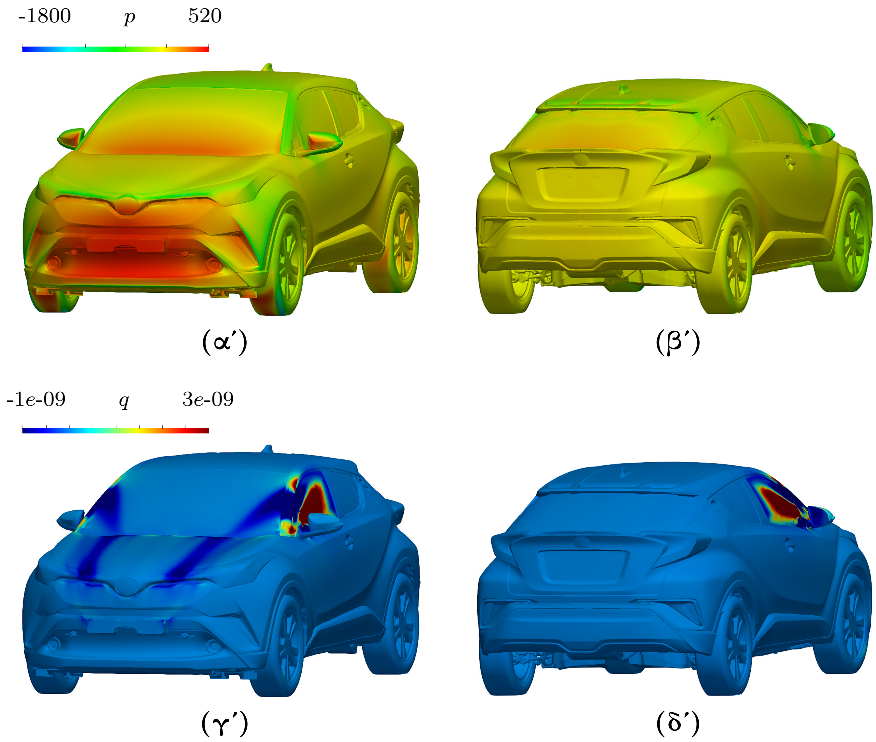

Σχήμα 5.12: *Κατανομή της πίεσης* p *και της συζυγούς πίεσης* q *πάνω στην επιφάνεια του αυτοκινήτου. Η συζυγής πίεση μεγιστοποιείται σην επιφάνεια των παραθύρων του αυτοκινήτου, ενώ συνολικά παρουσιάζει σημαντικά χαμηλότερες τιμές από την πίεση.*

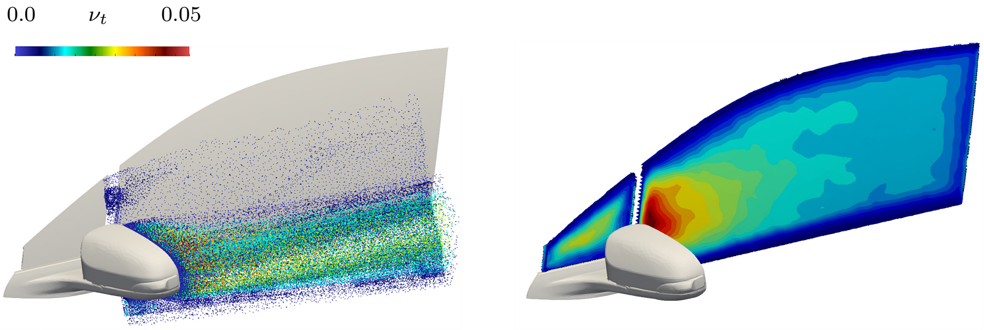

(α′) *Ισο-επιφάνειες του* ν_t *πεδίου*

(β′) *Το* ν_t^2 *πεδίο του όγκου* $\Omega^{'}$

Σχήμα 5.13: *Το* ν_t *πεδίο απεικονιζόμενο κατάντι του καθρέπτη του αυτοκινήτου με χρήση ισο-επιφανειών. Το* ν_t^2 *πεδίο, εν συνεχέια, υπολογίζεται και ολοκληρώνεται εντός του όγκου* $\Omega^{'}$*, προκειμένου να αξιολογηθεί η τιμή της συνάρτησης κόστους.*

Αποτελέσματα Βελτιστοποίησης μορφής

Κατόπιν της παραμετροποίσης του καθρέπτη και της επίλυσης της συζψγούς ροής, έγινε δυνατή η βελτιστοποίηση μορφής του καθρέπτη. Η βελτιστοποίηση πραγματοποιήθηκε χωρίς να επιβληθούν περιορισμοί, παρά του ότι ορίστηκε μέγιστη παραμόρφωση καθρέπτη $2mm$ από κύκλο σε κύκλο βελτιστοποίησης.

Σε συμφωνία με τους διαθέσιμους υπολογιστικούς πόρους, ο αλγόριθμος βελτιστοποίησης προχώρησε για 4 συνολικά κύκλους, ενώ ο 5ος κύκλος οδήγησε σε ένα σημαντικά παραμορφωμένο πλέγμα που αποτυγχάνει τις μετρικές. Στο τέλος κάθε κύκλου, οι εξισώσεις ροής λύθηκαν εκ νέου και η συνάρτηση κόστους αξιολογήθηκε για κάθε νέα παραμορφωμένη γεωμετρία. Η σύγκλιση της συνάρτησης κόστους παρουσιάζεται στο σχήμα **5.14**. Μετά από συνολικά 4 κύκλους βελτιστοποίησης, παρατηρείται μια είωση της τάξης του 16% στην F.

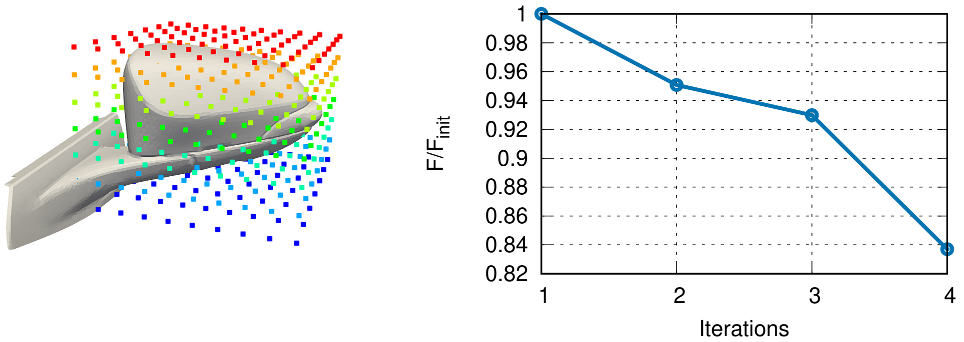

(α΄) *Κουτί ελέγχου γύρω από τον καθρέπτη*

(β΄) *Σύγκλιση της συνάρτησης κόστους θορύβου*

Σχήμα 5.14: *Ιστορία σύγκλισης της αντικειμενικής συνάρτησης του θορύβου F. Όλες οι τιμές έχουν διαιρεθεί με F_{init}, όπου F_{init} είναι η τιμή της συνάρτησης κόστους που υπολογίζει η πρωταρχική γεωμετρία καθρέπτη.*

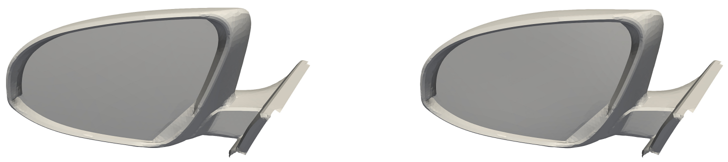

(α΄) *Αρχική γεωμετρία*

(β΄) *2ος κύκλος βελτιστοποίησης*

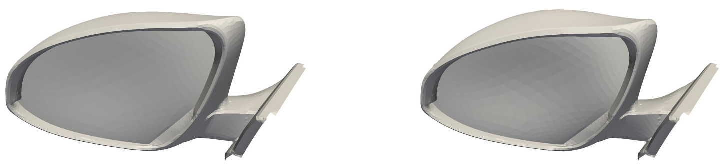

(γ΄) *3ος κύκλος βελτιστοποίησης*

(δ΄) *4ος κύκλος βελτιστοποίησης*

Σχήμα 5.15: *Αρχική γεωμετρία του πλευρικού καθρέπτη και τρεις προκύπτουσες από τη βελτιστοποίηση παραμορφωμένες γεωμετρίες.*

(α′) *Αρχική γεωμετρία*

(β′) *2ος κύκλος βελτιστοποίησης*

(γ′) *3ος κύκλος βελτιστοποίησης*

(δ′) *4ος κύκλος βελτιστοποίησης*

Σχήμα 5.16: *Άνω όψη της αρχικής γεωμετρίας και των τριών παραμορφωμένων γεωμετριών του καθρέπτη. Η εσωτερική ακμή της βελτιστοποιημένης γεωμετρίας ανάντι της ροής είναι αισθητά στρογγυλοποιημένη σε σχέση με την αρχική γεωμετρία, αλλαγή που πιθανώς μειώνει την τοπική αποκόλληση της ροής.*

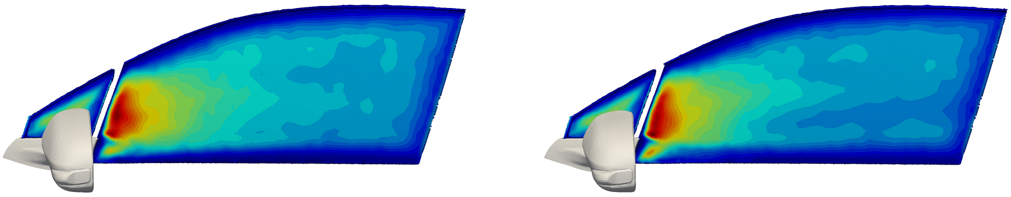

(α′) *Αρχική γεωμετρία*

(β′) *2ος κύκλος βελτιστοποίησης*

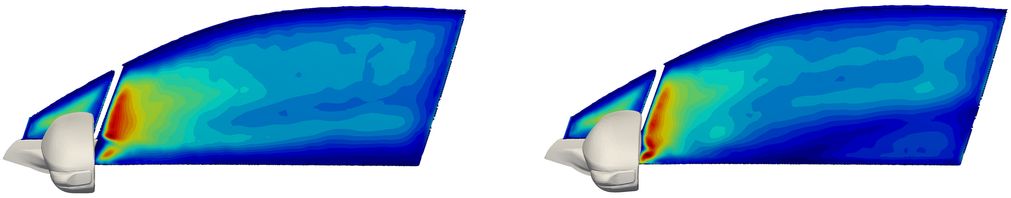

(γ′) *3ος κύκλος βελτιστοποίησης*

(δ′) *4ος κύκλος βελτιστοποίησης*

Σχήμα 5.17: *Το ν_t^2 πεδίο υπολογισμένο χρησιμοποιώντας την αρχική και τις τρεις βελτιστοποιημένες γεωμετρίες καθρέφτη, απεικονισμένο πάνω σε επίπεδο του όγκου $\Omega^{'}$.Η βέλτιστη γεωμετρία καθρέπτη υπολογίζει τιμή ν_t^2 της τάξης του 16% μικρότερη από την αρχική γεωμετρία.*

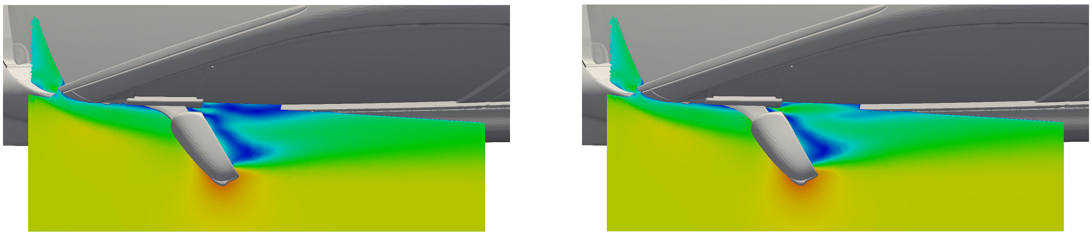

(α′) *Αρχική γεωμετρία* (β′) *2ος κύκλος βελτιστοποίησης*

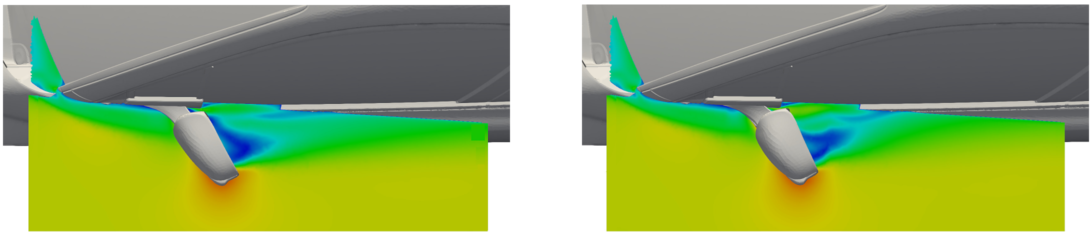

(γ′) *3ος κύκλος βελτιστοποίησης* (δ′) *4ος κύκλος βελτιστοποίησης*

Σχήμα 5.18: *Μέτρο της ταχύτητας U υπολογισμένο για την αρχική γεωμετρία και για τις τρεις παραμορφωμένες γεωμετρίες καθρέπτη, απεικονιζόμενο σε επίπεδο παράλληλο στον δρόμο. Η βέλτιστη γεωμετρία δείχνει να κατευθύνει τον ομόρρου του καθρέπτη προς το παράθυρο του οδηγού.*

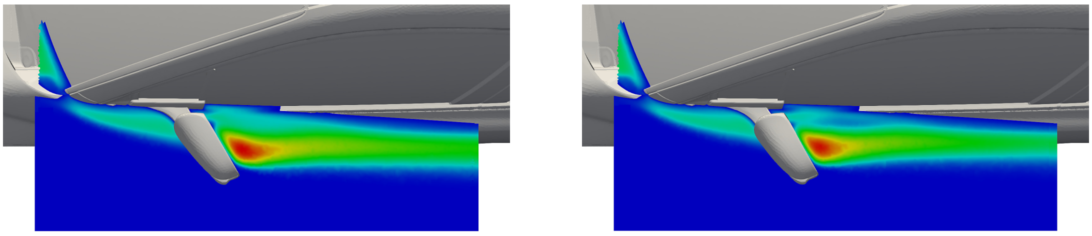

(α′) *Αρχική γεωμετρία* (β′) *2ος κύκλος βελτιστοποίησης*

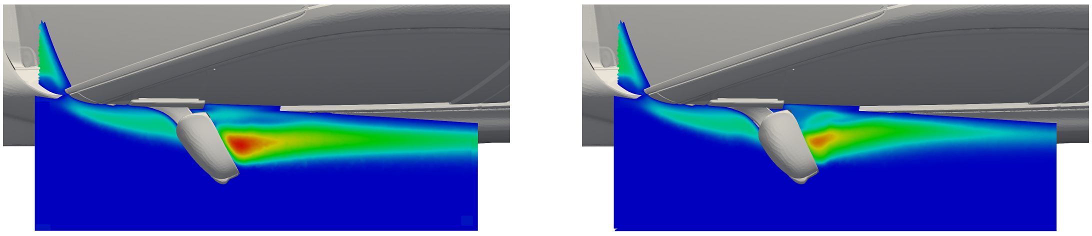

(γ′) *3ος κύκλος βελτιστοποίησης* (δ′) *4ος κύκλος βελτιστοποίησης*

Σχήμα 5.19: *Το ν_t πεδίο υπολογιζόμενο για την αρχική γεωμετρία και για τις τρεις παραμορφωμένες γεωμετρίες καθρέπτη, απεικονιζόμενο σε επίπεδο παράλληλο στον δρόμο. Μείωση στα επίπεδα ν_t παρατηρούνται όχι μόνο κοντά στο παράθυρο του οδηγού, όπου ο όγκος Ω' της συνάρτησης κόστους ορίζεται, αλλά επίσης και κατά μήκος όλου του ομόρρου του καθρέπτη.*

Bibliography

[1] Oettle, N. and Sims-Williams, D.: *Automotive aeroacoustics: An overview.* Proceedings of the Institution of Mechanical Engineers, Part D: Journal of Automobile Engineering, 231:095440701769514, April 2017. 10.1177/0954407017695147.

[2] Helfer, M.: *General aspects of vehicle aeroacoustics.* June 2005.

[3] Oettle, N., Sims-Williams, D., Dominy, R., Darlington, C., Freeman, C., and Tindall, P.: *The effects of unsteady on-road flow conditions on cabin noise.* In *SAE Technical Paper*. SAE International, April 2010. `https://doi.org/10.4271/2010-01-0289`.

[4] Papoutsis-Kiachagias, E.M., Magoulas, N., Mueller, J., Othmer, C., and Giannakoglou, K.C.: *Noise reduction in car aerodynamics using a surrogate objective function and the continuous adjoint method with wall functions*, volume 122. Computers and Fluids, 2015.

[5] Τσαγγάρης, Σ.: *Μηχανική των Ρευστών.* Συμεών, Αθήνα, 2005.

[6] Γιαννάκογλου, Κ. Χ.: *Μέθοδοι Βελτιστοποίησης στην Αεροδυναμική.* Πανεπιστημιακές Εκδόσεις Ε.Μ.Π., Αθήνα, 2006.

[7] Giannakoglou, K.C., Papadimitriou, D.I., Papoutsis-Kiachagias, E.M., and Othmer, C.: *Adjoint methods in cfd-based optimization - gradient computation & beyond.* ECCOMAS 2012–European Congress on Computational Methods in Applied Sciences and Engineering, 2012.

[8] Yang, Z.: *Large-eddy simulation: Past, present and the future.* Chinese Journal of Aeronautics, 91, December 2014. 10.1016/j.cja.2014.12.007.

[9] J. Fröhlich, W. Rodi: *Introduction to Large Eddy Simulation of Turbulent Flows.* Insitute for Hydromechanics, University of Karlsruhe.

[10] P. Spalart, Philippe, Jou, W., Strelets, M., and Allmaras, S.: *Comments on the feasibility of les for wings, and on a hybrid rans/les approach.* January 1997.

[11] Fröhlich, J. and von Terzi, D.: *Hybrid LES/RANS methods for the simulation of turbulent flows.* Progress in Aerospace Sciences, 44(5):349–377, July 2008. 10.1016/j.paerosci.2008.05.001.

[12] Spalart, P. R., Deck, S., Shur, M. L., Squires, Kyle, Strelets, M. Kh, and Travin, A.: *A new version of detached-eddy simulation, resistant to ambiguous grid densities*. Theoretical and Computational Fluid Dynamics, 20(3):181–195, July 2006, ISSN 0935-4964. 10.1007/s00162-006-0015-0.

[13] Spalart, P.: *Detached-eddy simulation*. Annual Review of Fluid Mechanics, 41:181–202, January 2009. 10.1146/annurev.fluid.010908.165130.

[14] Lighthill, M. J.: *On sound generated aerodynamically. i. general theory*. Proceedings of the Royal Society of London Series A, 211(1107):564–587, 1952. 10.1098/rspa.1952.0060.

[15] Curle, N.: *The influence of solid boundaries upon aerodynamic sound*. Proceedings of the Royal Society of London. Series A, Mathematical and Physical Sciences, 231(1187):505–514, 1955, ISSN 00804630. `http://www.jstor.org/stable/99804`.

[16] Papoutsis-Kiachagias, E.M., Asouti, V.G., Giannakoglou, K.C., Gkagkas, K., Shimokawa, S., and Itakura, E.: *Multi-point aerodynamic shape optimization of cars based on continuous adjoint*. Structural and Multidisciplinary Optimization, 59(2):675–694, 2019.

[17] Tucker, P.: *Computational Aeroacoustics*, pages 271–324. January 2014.

[18] Lighthill, M. J.: *On sound generated aerodynamically. ii. turbulence as a source of sound*. Proceedings of the Royal Society of London. Series A, Mathematical and Physical Sciences, 222(1148):1–32, 1954, ISSN 00804630. `http://www.jstor.org/stable/99373`.

[19] Papoutsis-Kiachagias, E.M.: *Adjoint methods for turbulent flows, applied to shape and topology optimization and robust design*. PhD thesis, Lab. of Thermal Turbomachines, N.T.U.A., Athens, 2013.

[20] Powell, A.: *Vortex Sound*. Report (University of California, Los Angeles. Department of Engineering). Department of Engineering, University of California, 1961. `https://books.google.gr/books?id=paZRXwAACAAJ`.

[21] Howe, M. S.: *Contributions to the theory of aerodynamic sound, with application to excess jet noise and the theory of the flute*. Journal of Fluid Mechanics, 71(4):625–673, 1975. 10.1017/S0022112075002777.

[22] Disselhorst, J. H. M. and Wijngaarden, L. Van: *Flow in the exit of open pipes during acoustic resonance*. Journal of Fluid Mechanics, 99(2):293–319, 1980. 10.1017/S0022112080000626.

[23] *Acoustically induced periodic vortex shedding at sharp edged open channel ends: Simple vortex models*. Journal of Sound and Vibration, 161(2):281 – 299, 1993, ISSN 0022-460X. `http://www.sciencedirect.com/science/article/pii/S0022460X83710722`, https://doi.org/10.1006/jsvi.1993.1072.

[24] Phan, V.L., Tanaka, H., Nagatani, T., Wakamatsu, M., and Yasuki, T.: *A cfd analysis method for prediction of vehicle exterior wind noise*. SAE Int. J.

Passeng. Cars - Mech. Syst., 10:286–298, March 2017. https://doi.org/10.4271/2017-01-1539, 10.4271/2017-01-1539.

[25] Chernenko, S.: *Librow - fast fourier transform (fft).* http://www.librow.com/articles/article-10.

[26] White, P., Cobb, M., and Spratt, S.: *A comparison of five steady-state truncation heuristics for simulation.* January 2001. 10.1145/510378.510486.

[27] Hoad, K. and Robinson, S.: *Implementing mser-5 in commercial simulation software and its wider implications.* Proceedings - Winter Simulation Conference, pages 495–503, December 2011. 10.1109/WSC.2011.6147779.

[28] Wang, Y., Gu, Z., Li, W., and Lin, X.: *Evaluation of aerodynamic noise generation by a generic side mirror.* 37, January 2010.

[29] Spalart, P. and Allmaras, S.: *A one-equation turbulence model for aerodynamic flows.* AIAA Paper 1992-439, 30th Aerospace Sciences Meeting and Exhibit, Reno, Nevada, USA, January 6–9 1992.

[30] Moukalled, F., Darwish, M., and Mangani, L.: *The Finite Volume Method in Computational Fluid Dynamics. An Advanced Introduction with OpenFOAMand MATLAB.* Springer, 2016.

[31] Spalding, D. B.: *A single formula for the law of the wall.* Journal of Applied Mechanics, 28:455–457, 1961.

[32] Fletcher, R. and Reeves, C. M.: *Function minimization by conjugate gradients.* The Computer Journal, 7(2):149–154, January 1964, ISSN 0010-4620. https://doi.org/10.1093/comjnl/7.2.149, 10.1093/comjnl/7.2.149.

[33] Nocedal, Jorge and Wright, Stephen J.: *Numerical Optimization.* Springer, New York, NY, USA, 1999.

[34] Khalfan, H. Fayez, Byrd, R. H., and Schnabel, R. B.: *A theoretical and experimental study of the symmetric rank-one update.* SIAM Journal on Optimization, 3(1):1–24, 1993. https://doi.org/10.1137/0803001, 10.1137/0803001.

[35] Papadimitriou, D. and Giannakoglou, K.C.: *The continuous direct-adjoint approach for second order sensitivities in viscous aerodynamic inverse design problems.* Computers Fluids - COMPUT FLUIDS, 38:1539–1548, September 2009. 10.1016/j.compfluid.2008.12.007.

[36] Kavvadias, I.S., Papoutsis-Kiachagias, E.M., and Giannakoglou, K.C.: *On the proper treatment of grid sensitivities in continuous adjoint methods for shape optimization*, volume 301. Journal of Computational Physics, 2015.

[37] Giannakoglou, K.C., Papoutsis-Kiachagias, E.M., Kavvadias, I.S., and Gkaragkounis, K.Th.: *Continuous Adjoint in Shape & Topology Optimization - Recent Developments & Applications.* Conference: Seminar on Adjoint CFD Methods in Industry and Research, At Wiesbaden, Germany, 2016.

[38] Proudman, I.: *The generation of noise by isotropic turbulence.* Proc A Soc A, 59(2):675–694, 2019.

[39] Zymaris, A.S., Papadimitriou, D.I., Giannakoglou, K.C., and Othmer, C.: *Continuous adjoint approach to the spalart-allmaras turbulence model for incompressible flows.* Computers & Fluids, 38(8):1528–1538, 2009.

[40] Zymaris, A.S., Papadimitriou, D.I., Giannakoglou, K.C., and Othmer, C.: *Adjoint wall-functions: A new concept for use in aerodynamic shape optimization.* Journal of Computational Physics, 229(13):5228–5245, 2010.

[41] Papoutsis-Kiachagias, E.M. and Giannakoglou, K.C.: *Continuous adjoint methods for turbulent flows, applied to shape and topology optimization: Industrial applications.* Springer, 2014.

[42] Papoutsis–Kiachagias, E.M. and Giannakoglou, K.C.: *A parameterization and mesh movement strategy based on volumetric B-splines. Applications to shape optimization.* NTUA/PCOpt/2015/01 REPORT, 2015.

[43] Nocedal, J. and Wright, S.J.: *Numerical Optimization.* Springer, 1999.

[44] S2A, Wind Tunnels: *Souffleries aeroacoustiques automobiles.* `https://www.soufflerie2a.com/en/`.